DECAY OF HOT AND ROTATING NUCLEI FORMED IN HEAVY ION REACTIONS AT LOW ENERGIES

A THESIS

Submitted to the

FACULTY OF SCIENCE

THAPAR UNIVERSITY, PATIALA

for the degree of

DOCTOR OF PHILOSOPHY

by

MANPREET KAUR

SCHOOL OF PHYSICS AND MATERIALS SCIENCE

THAPAR UNIVERSITY

PATIALA-147004, PUNJAB

INDIA

Dedicated to

My Beloved Husband

who has been my strongest support and always been there for me

Thapar University, Patiala

CANDIDATE'S DECLARATION

I hereby certify that the thesis entitled "**DECAY OF HOT AND ROTATING NUCLEI FORMED IN HEAVY ION REACTIONS AT LOW ENERGIES**" in partial fulfilment of the requirements for the award of Degree of Doctor of Philosophy in the School of Physics and Materials Science, Thapar University, Patiala, is a record of my own work carried under the supervision of Dr. Manoj K. Sharma. The matter presented in this thesis has not been submitted by me in part or full for the award of any other degree in any other university or institute.

This is to certify that the above statement made by the candidate is correct to the best of our knowledge.

Dr. Manoj K. Sharma

(Supervisor)

Head of the Department

Dean R&SP

External Examiner

Date: 24.01.2014

Acknowledgements

Without question these acknowledgements must begin with a sincere and humble thank to the almighty for giving me the courage and strength for completing this task successfully.

My vocabulary run short to express my sincere and deepest gratitude to my supervisor, Dr. Manoj K. Sharma, Associate Professor, School of Physics and Materials Science, Thapar University, Patiala for his illuminating guidance, positive attitude, unfailing patience and being supportive throughout. I owe a debt of gratitude for his affectionate behavior and moral support throughout the period of my research. I greatly appreciate his knowledge and his willingness to always assist me in my research work. Working under his guidance I have earned a great deal of scientific knowledge which has shaped my research skills and encouraged me to pursue in research field. This document would not exist without his guidance and patience. Thankyou very much sir. A special thanks to madam sharma for her affection.

I gratefully recognise the collaborative effort of Dr. Raj K. Gupta, Professor of Physics (Retd.), Physics Department, Panjab University, Chandigarh for his suggestions and positive criticisms in my research work. It is fortunate enough to work with him. I thank him for the valuable and innovative suggestions that enabled me to carry out this work.

I express sincere thanks to Dr. Kulvir Singh, Head, School of Physics and Materials Science, Thapar University, Patiala, for providing me the necessary facilities in the department and for his affectionate behavior throughout my research period. I also wishes to express my gratitude to all the faculty and staff of the School for their help and kind support. I am thankful to Prof. K. K. Raina, Director, for his encouragement and constant moral support to accomplish this task. My advisory doctoral committee members Dr. Suneel Kumar, Dr. A. K. Lal and Dr. Alka Upadhyay deserve many thanks for their useful suggestions during the progress report presentations. Thanks also goes to Dr. P.

iv

K. Bajpai, Dean of Research and Sponsored Projects for providing the possible research facilities. Special thanks to Prof. O. P. Pandey for the encouragement and moral support at bad times.

I would like to thank Dr. Birbikram Singh, Dr. Shefali Kanwar, Dr. Raj Kumar and Dr. Gudveen Sawhney for their gentle guidance and suggestions which have helped me during my Ph.D. tenure. I am also thankful to Dr. Varinderjit Kaur and Dr. Rajni for their encouragement and support.

This thesis would not have been possible without the assistance of a number of individuals. I would like to thank Miss Deepika Jain, Miss Gurvinder Kaur, Miss Kirandeep Sandhu for the co-operation, encouragement and all time help. I am grateful to Karan, Mandeep, Rajni, Navjot and Aman for the help, support and jovial company. I am happy to acknowledge my friend Miss Rupinder Makkar who supported and inspired me during the awful phases of my life and shared happiness during the good times. I am thankful to many others who are not mentioned here but contributed to the completion of this thesis.

I concedes my heartiest admiration and gratitude for my parents (S. Gurmukh Singh and Mrs. Narinder Kaur) for the moral support and countless blessings. I am thankful to my sister Miss Navneet Kaur and brother Mr. Baljot Singh for their best wishes, support and love. Gratitude and regard is also recorded for the support offered by my in laws (S. Baldev Singh and Mrs. Kulwant Kaur).

Lastly the most important, my strongest support, I feel immense obligation, admiration and gratitude for my husband, S. Parminder Singh who always stood by me during the critical phases of life and encouraged me to reach this destination of knowledge. You have been the most indispensable source of strength for me. Thank you for everything. Special note of thanks to my cute son Bhavnoor Singh whose interests were ignored during the course of this work.

The financial assistance in the form of fellowship from University Grants Commission (UGC), New Delhi, under the "UGC Research Fellowships in Sciences for Meritorious Students" is gratefully acknowledged.

Patiala

August, 2013.

(Manpreet Kaur)

vi

List of Publications

I. International Journals:

1. Systematic study of the decay of ^{118,122}Ba* formed in ^{78,82}Kr-induced reactions at E_{lab} = 5.5 MeV/nucleon,

   Manpreet Kaur, Raj Kumar and Manoj K. Sharma, Phys. Rev. C **85**, 014609 (2012).

2. Decay mechanism of the ^{204}Po* nucleus formed in ^{16}O and ^{28}Si induced reactions,

   Manpreet Kaur and Manoj K. Sharma, Phys. Rev. C **85**, 054605 (2012).

3. Effects of deformations and orientations in the fission of actinide nuclear system ^{254}Fm* formed in ^{11}B +^{243}Am reaction,

   Manpreet Kaur, Manoj K. Sharma and Raj K. Gupta, Phys. Rev. C **86**, 064610 (2012).

4. Possible decay mechanisms of ^{220}Ra formed in carbon induced reaction,

   Manpreet Kaur and Manoj K. Sharma, AIP Conf. Proc. **1524**, 151 (2013).

5. Analysis of fragment distribution and associated effects in ^{12,13}C induced reactions,

   Manpreet Kaur and Manoj K. Sharma, Eur. Phys. J. A (under review).

6. Dynamics of ^{58}Ni+^{54}Fe→^{112}Xe* reaction across the Coulomb barrier,

   Manpreet Kaur and Manoj K. Sharma, Phys. Rev. C (under review).

II. In Conferences, Symposiums and Workshops:

1. Decay of ^{204}Po nucleus formed in ^{16}O and ^{28}Si induced reaction, **Manpreet Kaur** and Manoj K Sharma, DAE Symposium on Nuclear Physics, BITS (PILANI), Vol. **55**, 384 (2010).

2. Fusion-fission and related aspects of ^{204}Po formed in heavy ion reactions, **Manpreet Kaur** and Manoj K Sharma, DAE Symposium on Nuclear Physics, Andhra University, (Vishakhapatnam), Vol. **56**, 476 (2011).

3. Decay of ^{118,122}Ba formed in ^{78,82}Kr + ^{40}Ca reactions at beam energy 5.5 MeV/A, **Manpreet Kaur**, Raj Kumar and Manoj K. Sharma, DAE symposium on Nuclear Physics, Andhra University, (Vishakhapatnam), Vol. **56**, 514 (2011).

4. Deformation effects in the decay of actinide nuclear system ^{254}Fm* formed in ^{11}B induced channel, **Manpreet Kaur** and Manoj K. Sharma, NSD conference in Opatija, July 9-13, 2012.

5. Decay of ^{254}Fm* nucleus formed in ^{11}B + ^{243}Am reaction, **Manpreet Kaur** and Manoj K Sharma, DAE symposium on Nuclear Physics, Delhi University, Delhi, Vol. **57**, 426 (2012).

6. Contribution of incomplete fusion cross sections in ^{13}C + ^{207}Pb reaction, **Manpreet Kaur** and Manoj K Sharma, Punjab Science Congress, Baba Farid University of Health Sciences, Faridkot, February 7-9, (2013).

Contents

List of Figures

List of Tables

Abstract

The aim of the present work is to carry out an extensive theoretical investigation of the decay behavior of a variety of nuclear systems formed in heavy ion reactions. This investigation has been performed within the framework of dynamical cluster decay model (DCM), which is a non-statistical model used to account for the decay of hot (E≠0) and rotating (ℓ≠0) nuclei formed in low energy heavy ion reactions. The deformation, orientation, temperature and angular momentum effects of decaying fragments are explicitly included in this model. The thesis is organized into eight chapters and a brief outline of the work is given below.

Chapter 1 gives the general introduction related to present work, which includes the broad outline of theoretical developments related to the dynamics of hot and rotating compound nuclei formed in heavy ion reactions. A brief discussion is made in reference to competing non-compound nucleus contribution. Beside this, the role of angular momentum, anisotropies, deformations and orientations etc. is discussed in brief.

Chapter 2 gives the details of the methodology used, the dynamical cluster decay model (DCM) for the decay of hot and rotating nuclei. DCM is formulated from preformed cluster decay model (PCM) (for ground state decays) by considering the temperature effects in its various interaction terms. It is based on quantum mechanical fragmentation

theory (QMFT). In this formalism, the Schrodinger equation is solved which includes fragmentation potential as an input. The fragmentation potential is calculated as sum of binding energies, Coulomb interaction potential, proximity potential and angular momentum dependent potential. It may be noted that all the above terms are temperature dependent. Besides this, the deformations and orientations are incorporated well within DCM. Here the emission of light particles (LPs), intermediate mass fragments (IMFs) and fission fragments upto symmetric division of the compound nucleus, are treated on equal footings as the dynamical collective mass motions of preformed clusters or fragments through the barrier, in contrast to statistical models which follow different formalisms for different processes.

In **Chapter 3**, the decay of actinide nuclear system ^{254}Fm* formed in ^{11}B+^{243}Am reaction is studied using the dynamical cluster decay model (DCM), with choices of spherical, quadrupole deformation β_2 alone and higher multipole deformations β_2-β_4. For β_2 deformations, the optimum orientations θ_i^{opt} are used whereas for higher multipole deformations the compact orientations θ_i^c of decaying fragments are taken into account. Besides β_2-static, the effects of dynamical-β_2 deformations is also explored. The calculated cross-sections find excellent agreement with the available experimental data with spherical as well as deformed choices of fragmentations, enabling us to account for the role of important nuclear deformation effects in the ^{11}B induced nuclear reaction. Spontaneous decay of ^{254}Fm with cold elongated configuration and optimum orientation is also worked out. The mass distributions of excited fermium isotopes in the neighborhood of ^{254}Fm* is also explored. In addition, the role of temperature, angular momentum and fission fragment anisotropies is investigated in the context of chosen reaction.

In **Chapter 4**, the decay of ^{220}Ra* nucleus formed in two different entrance channels ^{12}C+^{208}Pb and ^{13}C+^{207}Pb is investigated over a wide range of incident energies using the dynamical cluster decay model (DCM). The excitation functions are calculated by considering quadrupole (β_2) deformations with optimum orientations (θ_i^{opt}) of decaying fragments. The DCM based cross sections for evaporation residue (ER), fission, αxn and neutron decay processes find nice agreement with the reported experimental data over wide range of incident energies. The cross sections corresponding to different decay mechanism are worked out within DCM by fitting neck length parameter ($\triangle$R). The entrance channel and angular momentum effects are investigated in reference to the above mentioned reaction channels. In addition to this, the fragment mass distribution is worked out by colliding ^{13}C weakly bound stable projectile with a variety of target nuclei resulting in ^{13}C+^{159}Tb, ^{13}C+^{181}Ta and ^{13}C+^{207}Pb reactions. At comparable projectile energies, the increase in target mass is shown to favor asymmetric fragmentation in the fissioning region. Beside this, the incomplete fusion (ICF) contribution is worked out for ^{12}C and ^{13}C channels by applying necessary energy corrections in the framework of DCM.

In **Chapter 5**, the role of deformations, orientations, angular momentum dependence along with possible presence of non compound nucleus (nCN) component is investigated in the decay of pre-actinide nucleus ^{204}Po* formed in ^{16}O and ^{28}Si induced reactions over a wide range of projectile energies having comparable $E_{c.m.}/V_c$ values for two channels. An experiment was performed to extract fusion-fission and evaporation residue cross-sections for ^{16}O + ^{188}O$\rightarrow$^{204}Po* and ^{28}Si +^{176}Yb$\rightarrow$^{204}Po* reactions over a wide range of energies (E_{lab} = 84-155 MeV). Within the Dynamical cluster decay model (DCM), the evaporation residue and the fission cross-sections are calculated in reference to the available data at various incident energies by simultaneously fitting the only parameter, neck-length (ΔR)

for evaporation residue and fission. The choice of different neck-length parameter(ΔR) values for ER and fission indicate that the two decay processes do not occur simultaneously i.e they occur in different time scales and evolve subject to the nature of dynamics of compound nucleus formed. The calculated evaporation residue cross-sections and fission cross-sections show excellent agreement with the reported data at all incident center of mass energies, except at one highest energy for the channel ^{28}Si +^{176}Yb$\rightarrow$^{204}Po* for fission. The disagreement between DCM calculations and reported data at highest incident center of mass energy for the ^{28}Si +^{176}Yb entrance channel may be associated with the presence of small amount of nCN effects which is in line with the predictions of the Preequilibrium model. Also the inbuilt property of barrier lowering effect of DCM seems to be operating in context of these reactions. The fission fragment anisotropies are also calculated using DCM based parameters for the non sticking moment of inertia, and it find reasonable comparison with experimental data. Finally, the isotopic effect is worked out by studying the decay of ^{202}Po* and ^{204}Po* nuclei formed in ^{16}O induced reactions at comparable $E_{c.m.}/V_c$ value.

In **Chapter 6**, the dynamical cluster decay model (DCM) is applied in reference to data on ^{78,82}Kr+^{40}Ca reactions at bombarding energy of 5.5 MeV/nucleon. For the nuclear systems ^{118,122}Ba*, the experimental data for complete charge spectrum is also available along with evaporation residue (ER) and fission cross-sections. Within the DCM approach, the total fission and evaporation residue cross-sections are fitted nicely for spherical choice of nuclei by simultaneously fitting of the neck length parameter. Effect of different level density parameter is also studied. Results of DCM calculations are compared with BUSCO, GEMINI and DNS based calculations. All the models use the maximum angular momentum ℓ_{max} as the fitting parameter, which in this work is fixed

via neck-length parameter($\triangle$R) for the penetrability P$\rightarrow$1. Also the role of non zero pairing strength (δ>0) is seen, using δ(T) in V_{LDM} as a fitting parameter, say to Li data. The effect of different proximity potentials is also studied. Finally some non-compound nucleus contribution is shown to be operating in context of reactions under study. The N/Z dependence of decay fragments is also studied for Ba isotopes with A = 114-126.

In **Chapter 7**, the decay of ^{112}Xe* compound system formed in massive heavy ion reaction ^{58}Ni+^{54}Fe is studied using DCM at both below and above barrier energies with the deformations and orientation degrees of freedom of the nuclei included in it. DCM calculations give nice description of the experimental fusion excitation function, σ_{ER} as a function of center of mass energy, within one parameter fitting, the neck length parameter (ΔR) whose value remains within the range of proximity interaction. The barrier height corresponding to the neck length parameter gives barrier modification in a straight forward way, which helps to address the fusion- evaporation cross sections particularly in below barrier region. The role of deformations, orientations, angular momentum and diffuseness parameter is investigated to look for the structure effect of decaying fragments. Finally the N/Z dependence of fragmentation structure of different compound systems formed via ^{58}Ni beam is explored.

Finally, in **chapter 8**, conclusions and an outlook of the work is presented.

Chapter 1

Introduction

The universe has always been a mystery ever since the big bang. The big bang theory describes the universe to be formed from tremendous explosion. An insatiable curiosity to know more has lead to scientific and technological advancements to explore the possible existence of universe. In order to understand the extreme of the universe we need to examine the subatomic world. Classically, the atomic structure comprises of fundamental elementary particles such as protons, neutrons and electrons. The protons and neutrons are packed tightly within the atomic nucleus which is about 10^{-12} cm in diameter and the electrons spin around the nucleus within discrete electronic shells. The electron shells, surrounding the nucleus in an atom are important however the existence of an atom is decided by the stability of the nucleus.

The nucleus contain a number of individual protons and neutrons that orbit relative to one another and interact with each other via various interactions e.g. attractive (nuclear force) and repulsive (Coulomb force). Understanding the nucleus and its properties is a pursuit of scientists for a long time. The field of physics that studies the building blocks of atomic nuclei, interactions between them and energies that make up the very heart of matter is termed as nuclear physics. Today nuclear physics is a diverse field, encompassing

research that spans dimensions from most microscopic (considering individual particles (neutrons and protons) in the nucleus to cosmic (large scales of astrophysical objects in the cosmos). The motivation to study nuclear physics comes from its potential to provide quality information which is not limited to nature and dynamics of the nuclear systems but also to its wider application in other branches of physics as well. The astrophysics is connected to nuclear physics in a way as most of the things in the universe are created through nuclear synthesis. Physicians use techniques learned from nuclear physics to perform diagnosis and therapy in areas deep inside the body (in medical imaging device). Beside this nuclear phenomenon find various other applications in diversified fields such as energy production, engineering, radio carbon dating etc. We can say nuclear physics is a branch of science which encompass a broad spectrum and enables us for the better understanding of the nature. The history of nuclear physics as a discipline may be traced to the discovery of radioactivity in 1896 by Henri Becquerel. The impact of nuclear physics extends well beyond propagating our scientific knowledge of the nucleus and nuclear properties. Investigation of nuclear properties and structure of the nuclei is an active, interesting and productive area of research. Nuclear physics in general have three aspects; studying the fundamental particles and their interactions, interpreting the properties and manifest technologically to benefit society.

The experimental and theoretical studies in nuclear physics have played a significant role in the development and understanding of present century physics. The atomic nucleus was studied extensively starting with Rutherford making the first nuclear reaction and proposing nucleus as the small central part of an atom. With advancement in this direction the nuclear constituents known as protons and neutrons were found which interact via strong and electro magnetic interactions while obeying the Pauli's exclusion principle. Nuclei exhibit incredible structural diversity, even on the scale of addition or removal of

nucleon. More firm theory could be developed on the framework of quantum mechanics. Quantum mechanics is an important mathematical formulation that enables to investigate the wave dynamics of material particles. Current research in nuclear physics is associated with the study of nuclei under extreme conditions e.g. high excitation energy, angular momentum, temperature etc.. Besides, the production of super heavy elements is also a topic of immense interest [1–3]. The number of stable proton-neutron configurations that are naturally abundant is around 300 and various other configurations are created in the laboratory. Experimentalists can produce such nuclei by using modern day nuclear physics facilities and its an endeavor to extend the periodic table. An advancement that has greatly helped to understand the nuclear dynamics is associated with advanced experimental facilities and availability of various theoretical models. Besides experimental investigations, the calculations based on theoretical models are very important tools to describe and understand the nuclear dynamics, and this work is intended to explore further knowledge about theoretical understanding of nuclear dynamics

Any measurement in nuclear physics is facilitated by a nuclear reaction. Therefore, nuclear reactions are an indispensable tool of nuclear physics to untangle the nuclear structure information while trying to extract information on various nuclear phenomena. It is ofcourse necessary to have a probe which is sensitive on the nuclear physics scale i.e of the order of 10^{-15}m. Earlier in the 20^{th} century, nuclear reactions were performed with beam of light particles (e.g. proton, deutron, α particles) at low energies. After the advent of large accelerators, heavy ion beams were created, which could reach large energies and consequently it became possible to extract structure information by identifying the reaction products. The study of nuclear reaction dynamics is important because it provides information not only about the nuclear structure but also regarding nuclear forces and many other phenomena related to nucleus.

With the high energy accelerating machines such as cyclotron, pelletron etc., the range of the projectile beams of nuclei have been obtained to energies varying from few MeV/nucleon to many GeV/nucleon. Depending upon the beam energy, the nuclear reactions are catorized into three groups. If the beam energy E $\leq$15 MeV/nucleon, it is termed as low energy nuclear reaction, intermediate energy if 15<E<500 MeV/nucleon and if E$\geq$500 MeV/nucleon, it is called as high energy nuclear reactions. The present work is confined to low energy nuclear reactions.

1.1 Low energy nuclear reactions

A large fraction of our knowledge on the properties of nuclei is derived from nuclear reactions. The collision of two nuclei lead to a nuclear reaction and the final products can be different from the initial ones. The study of nuclear reactions is important because of its impact on related fields of investigations. Measurement and calculation of nuclear reaction cross sections are of great importance for overall understanding of reaction mechanism. The nuclear reaction requires an energetic nuclear probe (projectile beam) coming from an accelerator or radioactive substance to incident on the target. Depending upon the reaction conditions, different types of reactions can occur. Broadly, a nuclear reaction is divided into two categories;(1) Compound nucleus reaction and (2) Non compound nucleus reaction.

1.1.1 Compound nucleus reaction

A reaction in which the projectile completely fuses with the target to form a composite system where nucleons equilibrate in all degrees of freedom is termed as compound nucleus reaction. For a compound nucleus reaction to occur, the energy of the interacting

nuclei must be high enough to overcome the Coulomb barrier because of the electromagnetic repulsion between the protons. Besides long range Coulomb interaction, the strong nuclear interaction also plays an important role in the formation of a compound nucleus. Unlike Coulomb interaction, the nuclear interaction is not well established and a variety of explanations are available to understand its behavior. In present work the role of well known proximity interaction is emphasized in context of nuclear dynamics. Blocki et. al. [4] introduced a simple formula known as the pocket formula of proximity potential for nucleon-nucleon interaction energy as a function of distance between the surface of the colliding nuclei. Various other proximity potentials are given in [5, 6]. Along with Coulomb and nuclear proximity interaction, effect of angular momentum dependent interaction is also investigated. The details of these interactions are discussed in chapter 2.

Compound nucleus reactions are more important at low energies and are a fruitful source of information of various nuclear properties. One of the most efficient ways to produce compound-nucleus reactions is through heavy ion collisions. Heavy ion (A$\geq$4) collisions is an important tool that enable us to understand the nuclear matter. The compound nucleus formed in these heavy ion reactions is hot (excited, E$\neq$0) and in rapid collective rotation ($\ell\neq0$). The energy and angular momentum of the incident particle beam is shared rapidly among the nucleons and is distributed over numerous degrees of freedom of the compound nucleus until sufficient energy is concentrated on a nucleon or a group of nucleons which the compound nucleus can emit to decay to form the stable daughter fragment. The compound nuclear process takes considerable amount of time (10^{-14}-10^{-16} sec.) and therefore compound nucleus forgets the memory of the mode of its formation. Therefore in general the decay of compound nucleus is independent of its formation, except for some exotic target projectile combinations where entrance channel

effect come into picture.

For a long time, the decay patterns of these hot and rotating nuclei formed in heavy ion reactions are investigated to understand the properties and behavior of nuclear systems. The decay mechanism of compound nucleus is generally treated using statistical processes, where eventually one or a group of nucleons occupy enough energy to escape the compound nucleus barrier. Depending upon the mass of the compound nucleus formed, there is competition between the particle emission/evaporation residue (ER) and nuclear fission. For light mass compound systems with $A_{CN}\approx$40-80, the light particles LPs also known as evaporation residues (ER) (A_2=1-4) are the dominating decay channel accompanied by intermediate mass fragments (IMFs) having quite small contribution. The IMFs are the fragments lying in the range $5\leq A_2\leq 20$. However for heavy mass nuclear systems, fission is the most probable decay mode due to its instability against centrifugal repulsion. Nuclear fission is a process which involves large scale rearrangement of constituents of the nucleus (nucleons) and finally splits into two fragments of comparable mass. Many advances in the understanding of the fusion and fission processes have been achieved due to extensive studies on various aspects of equilibration in the reactions. Beside this, heavy mass fragments (HMFs), the fragments in between IMFs and fission are also observed/predicted in some heavy ion reactions. The comparative analysis of ER, IMF, HMF, fission fragments, make the low energy reaction dynamics more interesting.

Heavy ion fusion-fission reaction paths are largely governed by the potential energy, impact parameter and the bombarding energy near and above the Coulomb barrier. Theoretically, various models have been developed to describe the above mentioned particle emission or decay processes. The emission of the light particles LPs, called evaporation residue, can be understood as the statistically equilibrated compound nucleus emission in Hauser Feshbech (HF) analysis [7, 8] and to understand the production of intermediate

mass fragments (IMF) and heavy mass fragments (HMF), the HF analysis is extended to include the heavier fragments in the BUSCO code [9] or in the Extended Hauser-Feshbach scission-point model [8]. Various other statistical fission model descriptions [10] have also been used that are based on either the scission-point [7] or saddle-point configuration, in the GEMINI code or the saddle-point transition-state model (TSM) [10–13]. Different processes i.e ER, IMF, HMF and fission fragments are considered separately in statistical models. It implies that statistical models follow different formalisms for different decay processes. Alternatively, another theoretical approach known as Dynamical cluster decay model (DCM) [14]- [19] has been developed by Gupta and collaborators to study the decay of hot and rotating compound nucleus using the collective clusterization approach for the emission of ER, IMF, HMF as well as fission. Interesting aspect about DCM is that, contrary to statistical approach it treats different decay possibilities on equal footing. Beside this, one can also account for much needed nuclear structure properties via the preformation factor in this collective clusterization method.

1.1.2 Non Compound nucleus reaction

In addition to compound nucleus process, depending upon the entrance channel mass asymmetry and incident energy, non compound nucleus processes like quasi fission (qf), deep inelastic collision (DIC) etc. start competing. The process where the interaction of projectile with the target do not lead to fully equilibrated nuclear system instead the system so formed may reseparate prematurely not forming a true compound nucleus, represents the non compound nucleus reactions. Similar to compound nucleus processes, the non compound nucleus (nCN) processes also contributes to provide interesting nuclear structure information and the reaction dynamics. The non compound nucleus reaction is a non equilibrium process involving quasi fission which is a fission like process that

precedes the formation of mononuclear system. Comprehensive studies [20–23] revealed limitations in the complete fusion process where reseparation of two fission like fragments from a dinuclear system occurs which however outwardly resembles compound nucleus fission process and is interpreted as quasi fission. The properties of the entrance channel appear to play a major role in the reaction dynamics of quasi fission.

Deep inelastic collision (DIC) is another non compound nucleus process which involves significant dissipation of kinetic energy and angular momentum [24, 25]. In this collision, the projectile and target stick together for a sufficiently longer time but shorter than compound nucleus life time where the exchange of nucleons take place and the product masses are similar to the projectile and target mass. DIC involve the sharing of nucleons between the target and projectile whereas incomplete fusion (ICF) reactions involve the transfer of nucleons from a lighter to heavier reaction partner.

1.1.3 Incomplete fusion (ICF)

In ICF, the projectile is assumed to breakup into its constituent clusters within the nuclear field of the target nucleus, where the partial fusion of one of the cluster occurs with the target to form new nuclear system having relatively less mass, charge and excitation energy. Due to the partial fusion of projectile, fractional momentum transfer takes place in the ICF. This observation of partial fusion of projectile in heavy ion reaction started when Britt and Quinton [26] observed fast α-particles in massive transfer reactions . Since then the ICF dynamics has been investigated actively using heavy ion-beam facilities and also theoretically using various models [27,28]. The Complete fusion (CF) and incomplete fusion (ICF) reaction modes can be extricated on the basis of the input angular momentum as per the prescription in [29,30]. It is worth mentioning here that the angular momentum extracted experimentally is based on the non sticking limit (I_{NS}) of moment of inertia.

However within the proximity interactions (nuclear surface $\leq$2 fm apart), the sticking limit of moment of inertia (I_S) seems more appropriate, which results into large limiting value of angular momentum [31].

The interaction between the projectile and target also depends upon their shape i.e whether they are spherical or deformed.

1.2 Deformation and orientation effects

Collisions between deformed and oriented nuclei have been of huge interest during last few decades. For a long time, it has been known that the deformation degrees of freedom play a significant role in the better description of the nuclear reaction dynamics. Since most of the nuclei are deformed so the deformation degrees of freedom plays an important role in the formation and decay process of a nuclear system. The quest regarding shape of nucleus fascinated the nuclear physics community for many years. In earlier days, nucleus was considered to have spherical shape with symmetric charge distribution but soon it was realized that this definition works only for some percentage of nuclei whereas the remaining ones show non spherical distribution. The quadrupole moment is a measure of the departure from spherical symmetry, such nuclei are said to have quadrupole (β_2) deformation. This is the lowest order of deformation in nuclei. It can be prolate ellipsoidal or oblate ellipsoidal depending upon the positive and negative β_2 deformation parameter. Quadrupole moment in general is given by $2/5Z(b^2\text{-}a^2)$ where Z is the atomic number and b and a are the semi major and semi minor axis of the nuclei.

The shape of an atomic nucleus actually reflects the shell structure of nucleons (protons and neutrons) present. For a spherical nucleus, the shells are completely filled and we talk of a magic nucleus however most of the nuclei are deformed when they occupy the space

inbetween two magic shells. The nucleus can also coexist in different shapes (elongated or flattened) at the same time. Quadrupole deformation is the simplest form of deformation however higher multipole deformation such as octupole and hexadecapole deformations are also important and play a significant role to understand the nuclear dynamics. Fig.

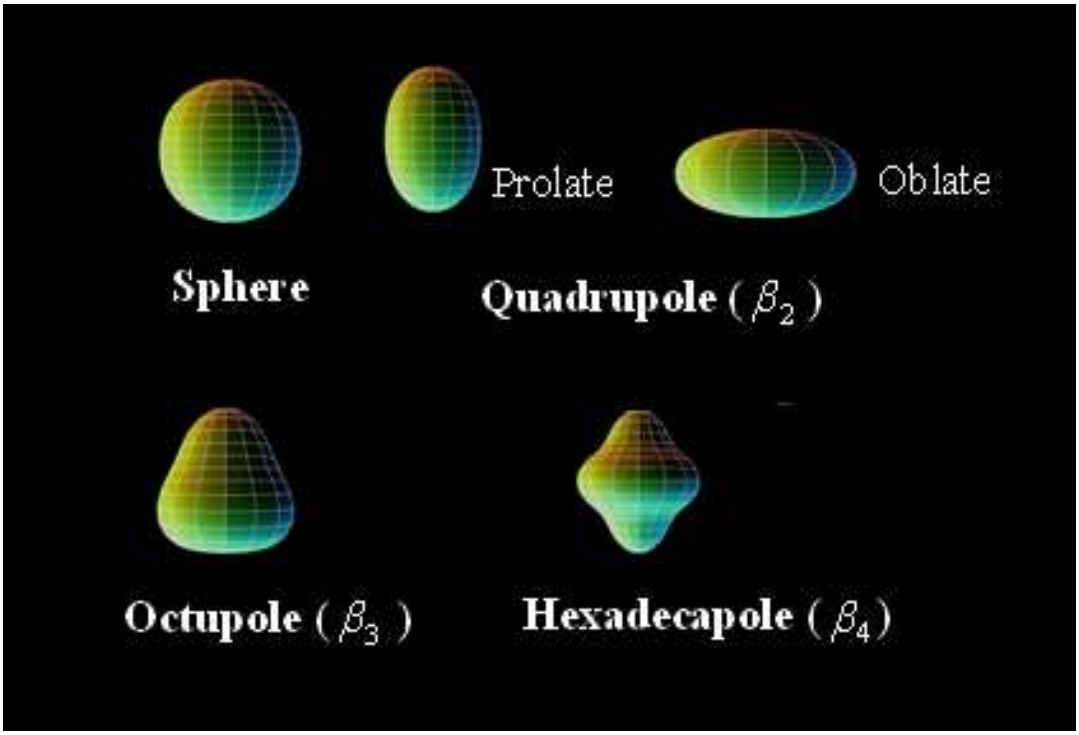

Figure 1.1 Schematic diagram for various orders of deformations of nuclei.

1.1 gives the various orders of deformations of a nuclear system. Octupole deformation gives the nucleus pear like shape and describes the reflection asymmetry in the nuclear shape. The nuclear reactions involving deformed nuclei are widely applied in various laboratories around the world for the synthesis of many heavy and superheavy elements. Besides the deformation effects, the orientation degree of freedom hold an important place in the reaction dynamics. Deformed nuclei can be oriented in same plane (coplanar) or in different plane (non-coplanar), however the present study is confined to coplanar orientation only.

Considering only the co-planar collisions of the deformed nuclei, compact shapes (small interaction radius) are favorable in comparison to elongated shapes (large interaction radius). A study by Gupta and collaborators [32–34], based on quantum mechanical fragmentation theory (QMFT) [35,36] shows that the interaction radius as well as the barrier is significantly affected with the inclusion of deformation and orientation effects. It has been found that the inclusion of deformation and orientation degrees of freedom of the colliding nuclei lead to the reduction of the barrier height. In [15], it was worked out

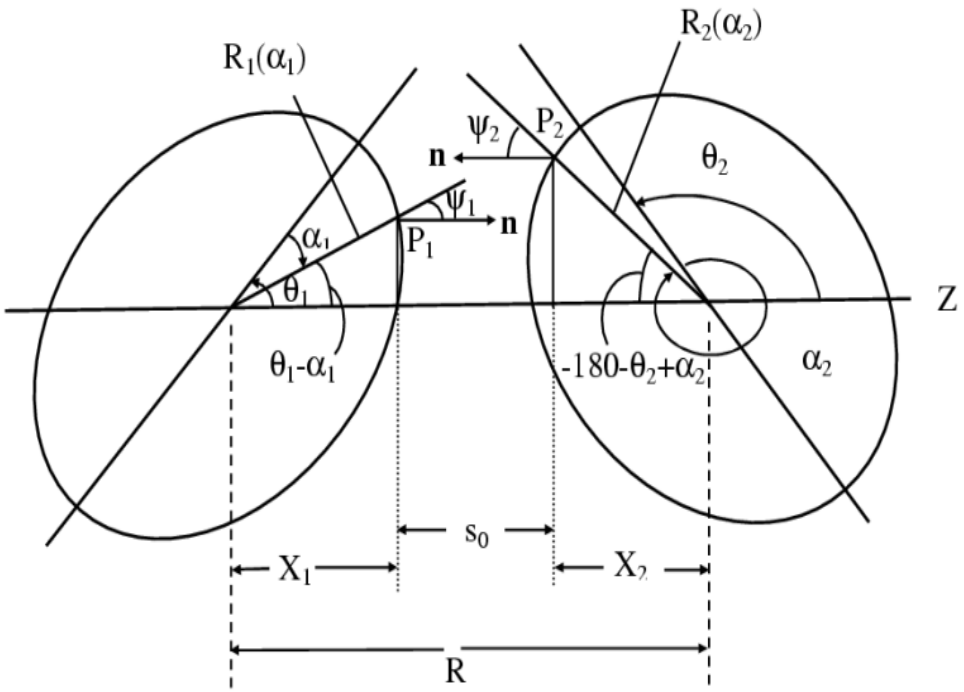

Figure 1.2 Schematic configurations of two (equal/ unequal) axially symmetric deformed, oriented nuclei, lying in the same plane and for various θ_1 and θ_2 values in the range 0^o to 180^o. The θ's are measured in anti-clockwise from the colliding axis and the angle α's in clockwise from the symmetry axis [42].

that the optimum orientations depend upon the signs of quadrupole deformations alone for both hot and cold fusion reactions being independent of the signs of hexadecapole deformation. Whereas the "compact" orientations refer to fusion configurations [17] cor-

responding to smallest interaction radius and are used for higher multipole deformations, particularly for positive hexadecapole deformations.

It is important to note that the distance between mass centers of the reaction partners rely on the orientation of the deformed nuclei [37–40]. Various studies show that the collision with tip to tip of deformed projectile-target nuclei lead to quasi-fission and the their side collisions results in fusion-fission [37, 41].

Fig. 1.2 shows a schematic configuration of two (equal/unequal) axially symmetric deformed, oriented nuclei, coplanar (lying in the same plane(ϕ=0)) for various values of θ_1 and θ_2 in the range 0° to 180°. For the nuclear collisions involving spherical plus deformed nuclei, only one orientation angle θ is enough, referring to the rotationally symmetric deformed nucleus. More details of Fig. 1.2 are discussed in chapter 2.

The configurations based on deformed and oriented nuclei are very decisive for determining the reaction cross sections. The explicit study of role of deformation and orientation certainly provide quality information regarding the dynamics of a nuclear system. The above discussion conclude that the inclusion of deformation and orientation effects are highly desirable for the proper understanding of nuclear reaction dynamics and related aspects.

One of the important quantities of interest in the reaction dynamics is the reaction cross section. It is a measure of the probability for a particular reaction to occur. The comparison between the experimentally measured and theoretically calculated cross sections for a variety of reactions enables us to validate nuclear reaction mechanisms. In this thesis, theoretical investigations of excitation functions or cross-sections for compound nucleus decay are made and the same are compared with available experimental data. The ER, IMF, HMF and fission cross sections are calculated for a variety of nuclear systems over a wide range of nuclear mass, lying between A=100-255. Specifically the

decay of $^{254}Fm^*$, $^{220}Ra^*$, $^{204}Po^*$, $^{118,122}Ba^*$ and $^{112}Xe^*$ nuclear systems are investigated over a range of energies comprising of both below as well as above barrier energies. Such a theoretical study of heavy to medium mass nuclear systems provide an important information regarding the reaction mechanisms and associated nuclear structure effects. The mass distribution of the fragments, fission fragment anisotropies, effect of static and dynamic deformation, spontaneous decay, role of entrance channel, angular momentum, effect of various versions of proximity potential, barrier modification, diffuseness, shell effects etc. have been extensively investigated. In addition to this, the incomplete fusion cross sections are also addressed within DCM approach.

1.3 Organization of thesis

The thesis is organized as follows:

Chapter 2 gives details of the methodology, the Dynamical Cluster-decay Model (DCM) [14]- [19] for the decay of hot and rotating compound nuclear systems formed in heavy ion reactions. DCM, based on the Quantum Mechanical Fragmentation Theory (QMFT) [35, 36] for binary fragmentation, uses a collective mass transfer process. The process of binary decay is treated in terms of two contributing factors, the preformation probability P_0 of the decaying fragments and their penetrability P across the nuclear interaction barrier. Here the P_0 is calculated for all the possible fragments within the mother nucleus. Besides the temperature and angular momentum effects in the decay of hot (excited) compound nuclei, DCM takes care of the deformation and orientation effects of the nuclei involved. It is relevant to mention here that DCM is a reformulation of preformed cluster decay model (PCM) [43–45] of ground state decay, by considering the

temperature-dependence in binding energies, proximity potential, Coulomb interaction potential and angular momentum dependent potential.

In **Chapter 3**, DCM has been applied to study the decay of actinide nuclear system ^{254}Fm* formed in ^{11}B+^{243}Am reaction [46] in reference to data of [47]. The calculated cross sections find nice agreement with the experimental cross section within one parameter fitting in terms of neck length parameter (ΔR) of the model. The higher multipole deformations with proper choice of orientations of nuclei are found to play an important role in the decay of ^{254}Fm* nuclear system. Quadrupole deformations with optimum orientations (θ_i^{opt}) whereas higher multipole deformations with compact orientations (θ_i^{c}) are considered to study the decay of ^{254}Fm*. Besides static quadrupole deformation, the effect of dynamic deformation is nicely explored. Fragment mass distribution of various isotopes in the vicinity of ^{254}Fm* also give symmetric decay. Further for the first time the spontaneous decay of neutron rich nucleus ^{254}Fm is compared with the heavy ion induced decay, which gives asymmetric decay in contrast to being symmetric for the heavy ion induced decay. The fission fragment anisotropies are also nicely explored and are calculated within DCM for the non sticking limit for the moment of inertia.

In **Chapter 4**, various competing decay mechanism have been investigated in the decay of ^{220}Ra* compound system, over a range of energies, using DCM. The compound system ^{220}Ra* is formed in ^{12,13}C + ^{208,207}Pb reaction channels [48] involving weakly bound stable projectile. Entrance channel effects in reference to the above mentioned reaction channels have been explored. The decay mechanism of ^{220}Ra* formed in ^{13}C + ^{207}Pb reaction is briefly discussed in [49]. The fragmentation path for different decay mechanism show similar behavior and follow asymmetric mass distribution. The calculated [50] complete fusion (CF) and incomplete fusion (ICF) excitation functions for ^{220}Ra* compound system show nice agreement with the available experimental data [48]. The cross

sections are calculated by fitting the neck length parameter which gives the time scale of the various processes. The neck length parameter is higher for ER and for n-decay as compared to that for fission process. Fragmentation behavior is explored by colliding weakly bound projectile ^{13}C on different targets, which shows that the mass distribution changes from symmetric to asymmetric with the increase in the mass of the target.

Chapter 5 deal with the decay of preactinide nuclear system ^{204}Po*, formed in the ^{16}O + ^{188}Os and ^{28}Si + ^{176}Yb reaction channels over a wide range of energies using DCM. Interestingly, the entrance channel mass asymmetry of the chosen reactions when compared with Businaro Gallone mass asymmetry anticipate some nCN component in the reaction ^{28}Si + ^{176}Yb. The calculated ER as well as fission cross sections [51] by simultaneously fitting the necklength parameter for the two (ER and fission) decay processes, find good comparison with the available data [52] at all energies for both the reactions except for fission at one highest energy for the channel ^{28}Si + ^{176}Yb. This mismatch at one highest energy is associated with some contribution from non compound nucleus (nCN) process which is in line with the pre equilibrium model predictions. The entrance channel effects are absent as the decay of ^{204}Po* remains symmetric independent of the entrance channel. The deformations of decaying fragments are shown to play significant role in the dynamics of chosen reaction.

In **Chapter 6**, the decay of medium mass nuclei ^{118,122}Ba* is studied in reference to the data of [53]. The nuclear systems ^{118,122}Ba* formed in ^{78,82}Kr + ^{40}Ca reaction channels are studied using DCM [18]. Besides ER and fission cross sections, a complete charge spectrum is also available. The experimental ER and fission cross sections are achieved nicely within DCM approach. For the complete charge spectrum, except for some narrow region, DCM gives nice description of the observed data. The effect of different level density parameters is studied which seems to affect the cross sections negligibly, various

versions of proximity potential have also been attempted to account for the unfitted valley however finally nCN contribution is shown to be operating. The role of non-zero pairing strength (δ>0) is also seen. Results of DCM are also compared with various theoretical models, and DCM is shown to exhibit an overall better description. The N/Z dependence of decaying fragments for Ba isotopes depicts more α-structure for neutron deficient isotope and starts vanishing with increase in the number of neutrons in the parent nucleus.

Chapter 7 deals with the study of decay of $^{112}Xe^{*}$ compound system formed in the massive heavy ion reaction ^{58}Ni + ^{54}Fe over a wide range of energies spread across the Coulomb barrier. The DCM calculated [54] cross sections considering spherical as well as quadrupole deformed fragmentation path, find nice comparison with the experimental data [55] at all energies. The possible occurance of fusion hindrance at sub barrier region is addressed in terms of its inbuilt property of barrier lowering or barrier modification. The effect of various diffuseness coefficients have been investigated which shows large penetrability for lower diffuseness parameter, though the potential energy surfaces remain same and hence preformation probability does not depend much on this parameter. The effect of orientations in context of the chosen reaction is explored. The structure effects are analyzed considering nearly closed shell projectile ^{58}Ni, which shows prominent α-structure for neutron deficient compound system.

Finally **Chapter 8** presents the summary and significance of this work. The scope for possible extension of present work is also discussed.

Bibliography

[1] Yu. Ts. Oganessian, V. K. Utyonkov, Yu. V. Lobanov, F. Sh. Abdullin, A. N. Polyakov, I. V. Shirokovsky, Yu. S. Tsyganov, G. G. Gulbekian, S. L. Bogomolov, B. N. Gikal, A. N. Mezentsev, S. Iliev, V. G. Subbotin, A. M. Sukhov, A. A. Voinov, G. V. Buklanov, K. Subotic, V. I. Zagrebaev, M. G. Itkis, J. B. Patin, K. J. Moody, J. F. Wild, M. A. Stoyer, D. A. Shaughnessy, J. M. Kenneally, P. A. Wilk, R. W. Lougheed, R. I. Il'kaev and S. P. Vesnovskii, Phys. Rev. C **70**, 064609 (2004).

[2] Yu. Ts. Oganessian et. al, Phys. Rev. L **108**, 022502 (2012).

[3] S. Hofmann, S. Heinz et. al, Eur. Phys. J. A **48**, 62 (2012).

[4] J. Blocki, J. Randrup, W.J. Swiatecki, and C.F. Tsang, Ann. Phys. (N.Y.) **105**, 427 (1977).

[5] J. Randrup and J. S. Vaagen, Phys. Lett. B **77**, 170 (1978).

[6] J. R. Birkelund and J. R. Huizenga, Phys. Rev. C **17**, 126 (1978).

[7] R. J. Charity, M. A. McMahan, G. J.Wozniak, R. J. McDonald, L. G. Moretto, D. G. Sarantites, L. G. Sobotka, G. Guarino, A. Pantaleo, L. Fiore, A. Gobbi, and K.D. Hildenbrand, Nucl. Phys. A **483**, 371 (1988).

[8] T. Matsuse, C. Beck, R. Nouicer, and D. Mahboub, Phys. Rev. C **55**, 1380 (1997).

[9] J. Gomez del Campo, R. L. Auble, J. R. Beene, M. L. Halbert, H. J. Kim, A. DOnofrio, and J. L. Charvet, Phys. Rev. C **43**, 2689 (1991); Phys. Rev. Lett. **61**, 290 (1988).

[10] S. J. Sanders, A. Szanto de Toledo, and C. Beck Phys. Rep. **311**, 487 (1999).

[11] L. G. Moretto, Nucl. Phys. A **247**, 211 (1975).

[12] S. J. Sanders, D. G. Kovar, B. B. Back, C. Beck, D. J. Henderson, R. V. F. Janssens, T. F. Wang, and B. D. Wilkins, Phys. Rev. C **40**, 2091 (1989).

[13] S. J. Sanders, Phys. Rev. C **44**, 2676 (1991).

[14] M. Balasubramaniam, R. Kumar, R. K. Gupta, C. Beck and W. Scheid, J. Phys. G: Nucl. Part. Phys. **29**, 2703 (2003); R. K. Gupta, R. Kumar, N. K. Dhiman, M. Balasubramaniam, W. Scheid, and C. Beck, Phys. Rev. C **68**, 014610 (2003).

[15] R. K. Gupta, M. Balasubramaniam, R. Kumar, N. Singh, M. Manhas, and W. Greiner, J. Phys. G: Nucl. Part. Phys. C **31**, 631 (2005).

[16] B. B. Singh, M. K. Sharma and R. K. Gupta, Phys. Rev. C **77**, 054613 (2008).

[17] R. K. Gupta, M. Manhas, and W. Greiner, Phys. Rev. C **73**, 054307 (2006).

[18] M. Kaur, R. Kumar and M. K. Sharma, Phys. Rev. C **85**, 014609 (2012). K. Sandhu, M. K. Sharma and R. K. Gupta, Phys. Rev. C **85**, 024604 (2012). G. Kaur and M. K. Sharma, Phys. Rev. C **87**, 044601 (2013).

[19] M. K. Sharma, S. Kanwar, G. Sawhney, R. K. Gupta, and W. Greiner, J. Phys. G: Nucl. Part. Phys. **38**, 055104 (2011); D. Jain, R. Kumar, M. K. Sharma, and R. K. Gupta, Phys. Rev. C **85**, 024615 (2012).

[20] K. Nishio, H. Ikezoe, S. Mitsuoka, I. Nishinaka, Y. Nagame, Y. Watanabe, T. Ohtsuki, K. Hirose and S. Hofmann, Phys. Rev. C **77**, 064607 (2008).

[21] I. M. Itkis, E. M. Kozulin, M. G. Itkis, G. N. Knyazheva, A. A. Bogachev, E. V. Chernysheva, L. Krupa, Yu. Ts. Oganessian and V. I. Zagrebaev, A. Ya. Rusanov, F. Goennenwein, O. Dorvaux, L. Stuttge, F. Hanappe, E. Vardaci, E. de Goes Brennand, Phys. Rev. C **83**, 064613 (2011).

[22] D. J. Hinde, M. Dasgupta, J. R. Leigh, J. C. Mein, C. R. Morton, J. O. Neton and H. Timmers, Phys. Rev. C **53**, 1290 (1996).

[23] B. B. Back, Journal of Physics:Conference Series **282**, 012003 (2011).

[24] W. U. Schroder and J. R. Huizenga, in Damped Nuclear Reactions, Treatise on Heavy-ion Science, edited by D. A. Bromley (Plenum Press, New York, 1984), Vol. **2**, p. 115.

[25] J. G. Keller, B. B. Back, B. G. Glagola, D. Henderson, S. B. Kaufman, S. J. Sanders, R. H. Siemssen, F. Videbaek, B. D. Wilkins, and A. Worsham, Phys. Rev. C **36**, 1364 (1987).

[26] H. C. Britt and A. R. Quinton, Phys. Rev. **124**, 877 (1961).

[27] T. Udagawa, T. Tamura, Phys. Rev. Lett. **45**, 1311 (1980).

[28] J.P. Bondorf, J.N. De, G. Fai, A.O.T. Karvinen, B. Jakobsson, J. Randrup, Nucl. Phys. A **333**, 285 (1980).

[29] P.E. Hodgson, E. Gadioli, E. Gadioli Erba, Introductory Nuclear Physics, Clarendon Press, Oxford, Chapter 23, (1997).

[30] Pushpendra P. Singh, Abhishek Yadav, Devendra P. Singh, Unnati Gupta, Manoj K. Sharma, R. Kumar, D. Singh, R. P. Singh, S. Muralithar, M. A. Ansari, B. P. Singh, R. Prasad, and R. K. Bhowmik, Phys. Rev. C **80**, 064603 (2009).

[31] M. K. Sharma, G. Sawhney, R. K Gupta, and W. Greiner, J. Phys. G: Nucl. Part. Phys. **38**, 105101 (2011); M. K. Sharma, G. Sawhney, S. Kanwar, and R. K Gupta, Mod. Phys. Lett. A **25**, 2022 (2010).

[32] A.J. Baltz and B.F. Bayman, Phys. Rev. C **26**, 1969 (1982).

[33] M. Seiwert, W. Greiner, V. Oberacker and M.J. Rhoades-Brown, Phys. Rev. C **29**, 477 (1984).

[34] N. Malhotra and R.K. Gupta, Phys. Rev. C **31**, 1179 (1985).

[35] J. Maruhn and W. Greiner, Phys. Rev. Lett. **32**, 548 (1974). J. Maruhn and W. Greiner, Z. Phys. **251**, 431 (1972).

[36] R. K. Gupta, W. Scheid and W. Greiner, Phys. Rev. Lett. **35**, 353 (1975).

[37] D.J Hinde, M. Dasgupta, J.R. Leigh, J.P Lestone, J.C. Mein, C.R. Morton, J.O. Newton, and H. Timmers, Phys. Rev. Lett. **74**, 1295 (1995).

[38] M. Manhas and R.K. Gupta, Phys. Rev. C **72**, 024606 (2005).

[39] A. Iwamoto, P. Moller, J.R. Nix, and H. Sogawa, Nucl. Phys. A **596**, 329 (1996).

[40] R. K. Gupta, M. Manhas, G. Munzenberg, and W.Greiner, Phys. Rev. C **72**, 014607 (2005).

[41] K. Nishio, H. Ikezoe, S. Mitsuoka and K. Satou, and S.C. Jeong, Phys. Rev. C **63**, 044610 (2001).

[42] R. K. Gupta, N. Singh, and M. Manhas, Phys. Rev. C **70**, 034608 (2004).

[43] S. S. Malik and R. K. Gupta, Phys. Rev. C **39**, 1992 (1989).

[44] S. Kumar and R. K. Gupta, Phys. Rev. C **55**, 218 (1997).

[45] G. Sawhney, M. K. Sharma, and R. K. Gupta, Phys. Rev. C **83**, 064610 (2011).

[46] M. Kaur, M. K. Sharma, and R. K. Gupta, Phys. Rev. C **86**, 064610 (2012).

[47] R. Tripathi, K. Sudarshan, S. Sodaye, S. K. Sharma and A.V. R. Reddy, Phys. Rev. C **75**, 024609 (2007).

[48] K. Kalita, J. Phys. G: Nucl. Part. Phys. **38**, 095104 (2011).

[49] M. Kaur and M. K. Sharma, AIP Conf. Proc. **1524**, 151 (2013).

[50] M. Kaur and M. K. Sharma, Eur. Phys. J. A (under review).

[51] M. Kaur and M. K. Sharma, Phys. Rev. C **85**, 054605 (2012).

[52] R. Tripathi, K. Sudarshan, S. K. Sharma, K. Ramachandran, A. V. R. Reddy, P. K. Pujari, and A. Goswami, Phys. Rev. C **79**, 064607 (2009).

[53] G. Ademard, J. P. Wieleczko, J. Gomez del Campo, M. La Commara, E. Bonnet, M. Vigilante, A. Chbihi, J. D. Frankland, E. Rosato, G. Spadaccini, Sh. A. Kalandarov, C. Beck, S. Barlini, B. Borderie, R. Bougault, R. Dayras, G. De Angelis, J. De Sanctis, V. L. Kravchuk, P. Lautesse, N. Le Neindre, J. Moisan, A. D'Onofrio, M. Parlog, D. Pierroutsakou, M. F. Rivet, M. Romoli, R. Roy, G. G. Adamian, and N. V. Antonenko, Phys. Rev. C **83**, 054619 (2011).

[54] M. Kaur and M. K. Sharma, Phys. Rev. C (under review).

[55] A. M. Stefanini, G. Montagnoli, L. Corradi, S. Courtin, E. Fioretto, A. Goasduff, F. Haas, P. Mason, R. Silvestri, Pushpendra P. Singh, F. Scarlassara and S. Szilner, Phys. Rev. C **81**, 037601 (2010). A. M. Stefanini et. al *ibid.* **82**, 014614 (2010).

Chapter 2

Methodology

2.1 Introduction

Many theoretical models have been developed to understand the formation and decay of nuclear systems. In the present work, the reaction dynamics of hot and rotating nuclear systems over a wide mass range is investigated using the dynamical cluster decay model (DCM) [1]- [13], which is a reformulation of preformed cluster decay model (PCM) [14]- [19] for the ground state decay. DCM is a two step formalism: The first step is the formation of the cluster in the parent nucleus, followed by the second step in which the preformed cluster penetrates the barrier. The preformation probability is different for different fragments in the decay process. This fragmentation process is used to explain the evaporation residue (ER), intermediate mass fragments (IMF), fission fragments (FF) emission from the excited compound nucleus, where these processes are treated as the collective mass motion of preformed cluster through the barrier. It is relevant to mention here that the deformations and orientations of the nuclei involved are explicitly included along with temperature and angular momentum effects in this model (DCM). The advantage of using the DCM is that it gives the relative probability of all channels, through which

an excited compound nucleus can decay. Therefore this approach provides a significant information about the nuclear structure properties at compound nucleus state.

The DCM has been used extensively to study the decay paths of a large number of nuclear systems in light, medium, heavy and super-heavy mass regions, during last few years over a wide range of incident center-of-mass (c.m.) energies. DCM is based on well known Quantum Mechanical Fragmentation Theory, (QMFT) [20]- [27] (Sec. 2.2) which, is based on collective co-ordinate approach. QMFT is a unified description of two body channel heavy ion collision and is the only theory, given prior to experiments, that brings out clearly the applicability of the quantum concept of probability and role of shell effects for fusion reactions as well as for fission processes. QMFT (based on two center shell model), is used as an average two body potential in Strutinsky macro-microscopic method [28]. This theory is based on the fact that the fragments are pre-born prior to the decay of the compound nucleus. The quantum mechanical preformation probability P_0 of the decaying fragments or clusters formed in the mother nucleus can be calculated by solving a stationary Schrödinger equation in mass fragmentation coordinate. The preformation probability contains the structure information of CN system and its decaying fragments. Once the clusters/fragments are preformed, their penetration probability P across the interaction barrier can be calculated by using the WKB approximation.

The discussion on preformation probability P_0 and penetration probability P is presented in Sec. 2.2.8 and 2.2.9. The concept of "barrier lowering" and fission fragment anisotropy are discussed in Sec. 2.3.1 and 2.3.2, respectively.

2.2 Quantum Mechanical Fragmentation Theory

In QMFT [20]- [27], the substantive quantities for the description of the nuclear dynamics are the potential energy surfaces and the mass parameters defining the kinetic energy of the system. The static properties of nuclear system are determined by the potential energy alone. The QMFT is worked out in terms of the following collective variables:

(i) relative separation coordinate R between the two nuclei or, in general, two fragments (or, equivalently, the length parameter $\lambda = L/2R_0$, with L as the length of the nucleus and R_0 as the radius of an equivalent spherical nucleus).

(ii) The deformation co-ordinates $\beta_{\lambda i}$ (λ=2,3,4... and i=1,2) of the colliding nuclei.

(iii) The orientation degrees of freedom $\theta_i (i = 1, 2)$ of the deformed nuclei.

(iv) Azimuthal angle ϕ between the principal planes of the two colliding nuclei.

(v) Neck parameter ε, defined by the ratio $\varepsilon = E_0/E'$ for the interaction region ($R < R_1 + R_2$, R_i (i=1, 2) is the radius of the two nuclei). Here E_0 is the actual height of the barrier and E' is the fixed barrier of the two center oscillator. $\epsilon = 0$ represents a broad neck formation, whereas $\epsilon = 1$ gives that the neck is fully squeezed in, corresponding to the asymptotic region ($R > R_1 + R_2$).

(vi) Mass and charge fragmentation co-ordinates [20, 21, 26].

The mass and charge fragmentation for separated nuclei/fragments for the two body channels are defined by the mass and charge-asymmetry coordinates as

$$\eta = \frac{A_1 - A_2}{A}; \qquad \eta_Z = \frac{Z_1 - Z_2}{Z} \tag{2.1}$$

Similarly, the neutron asymmetry coordinate [21]

$$\eta_N = \frac{N_1 - N_2}{N}, \tag{2.2}$$

can also be used, but it is sufficient to treat only two of them as dynamical co-ordinates since they are related as

$$\eta = \frac{Z}{A}\eta_Z + \frac{N}{A}\eta_N \tag{2.3}$$

Here $A = A_1 + A_2$, $Z = Z_1 + Z_2$ and $N = N_1 + N_2$. A_i, Z_i and N_i $(i = 1, 2)$ are respectively the mass number, the charge number and the neutron number of two fragments. A, Z and N are respectively the mass number, charge number and neutron number of the compound system. The limiting values of η are $0 \leq |\eta| \leq 1$ and thus allows a unified description of a few-nucleon, multi-nucleon (a cluster) transfer, a large-mass transfer, the complete fusion $(|\eta| = 1)$ of nuclei and the symmetric $(\eta = 0)$, asymmetric and super-asymmetric fission of a compound nucleus. The η_Z coordinate gives the associated charge distribution effects. In terms of these collective coordinates and their velocities, the collective Hamiltonian can be written as

$$H = K(\mathbf{R}, \beta, \varepsilon, \eta, \eta_Z; \dot{\mathbf{R}}, \dot{\beta}, \dot{\varepsilon}, \dot{\eta}, \dot{\eta}_Z) + V(\mathbf{R}, \beta, \varepsilon, \eta, \eta_Z). \tag{2.4}$$

Here K refers to the kinetic energy and V to collective potential energy and β stand for $\beta_{\lambda 1}$ and $\beta_{\lambda 2}$; λ=2,3,4... . For the compound nucleus formation, the neck parameter is assumed to be zero i.e $\epsilon = 0$. This is so because, once the neck formation starts between the two colliding nuclei, then fission phenomenon can never be stopped, i.e. excited compound nucleus will proceed towards the disintegration process.

For the potential $V(\eta, \eta_Z, R)$, minimized in the η_Z co-ordinate, Schrödinger wave equation in terms of mass parameters η and relative separation R co-ordinates can be written as:

$$H(\eta, R)\psi(\eta, R) = E(\eta, R)\psi(\eta, R) \tag{2.5}$$

with the Hamiltonian,

$$H(\eta, R) = K(\eta) + K(R) + K(\eta, R) + V(\eta) + V(R) + V(\eta, R) \tag{2.6}$$

The mass parameters B_{ij}, defining the kinetic energy term K in the above Eqs. (2.4) and (2.6) are either the consistently calculated cranking masses using the Asymmetric Two-Center Shell Model ($ATCSM$) or the classical hydrodynamical masses, which are shown to have good agreement with microscopic cranking calculations. The coupling term of the kinetic energy $K(\eta, R)$, proportional to $\frac{\partial^2}{\partial\eta\partial R}$, is neglected here, since the coupled cranking masses are very small [20, 21], ($\mathrm{B}_{R\eta} \ll (B_{RR}B_{\eta\eta})^{1/2}$ and $\mathrm{B}_{R\eta_Z} \ll (B_{RR}B_{\eta_Z\eta_Z})^{1/2}$). Same is true for the coupling term of potential energy $V(\eta, R)$.

Therefore, in a decoupled approximation [27], the Schrödinger equation (2.5) can be solved for which the Hamiltonian takes the form:

$$H = -\frac{\hbar^2}{2\sqrt{B_{\eta\eta}}}\frac{\partial}{\partial\eta}\frac{1}{\sqrt{B_{\eta\eta}}}\frac{\partial}{\partial\eta} - \frac{\hbar^2}{2\sqrt{B_{RR}}}\frac{\partial}{\partial R}\frac{1}{\sqrt{B_{RR}}}\frac{\partial}{\partial R} + V(\eta) + V(R). \tag{2.7}$$

For decoupled Hamiltonian (2.7), Schrödinger wave equation (2.5) can be separated for the two co-ordinates η and R as follows,

$$\left[-\frac{\hbar^2}{2\sqrt{B_{\eta\eta}}}\frac{\partial}{\partial\eta}\frac{1}{\sqrt{B_{\eta\eta}}}\frac{\partial}{\partial\eta} + V(\eta)\right]\psi^{\nu}(\eta) = E^{\nu}_{\eta}\psi^{\nu}(\eta) \tag{2.8}$$

and

$$\left[-\frac{\hbar^2}{2\sqrt{B_{RR}}}\frac{\partial}{\partial R}\frac{1}{\sqrt{B_{RR}}}\frac{\partial}{\partial R} + V(R)\right]\psi^{\nu}(R) = E^{\nu}_{R}\psi^{\nu}(R) \tag{2.9}$$

with

$$\psi(\eta, R) = \psi(\eta)\psi(R) \tag{2.10}$$

and

$$E = E_\eta + E_R \tag{2.11}$$

The states $\psi^\nu(\eta)$ are the vibrational states in the potential $V(\eta)$ and are labelled by the quantum numbers $\nu = 0, 1, 2, ...$

In the following subsections, we first discuss the various terms of Schrödinger wave equations (2.8) and (2.9) and then give the solution of Eq. (2.8) for the determination of preformation probability $P_0 \propto |\psi^0(\eta)|^2$.

2.2.1 The Scattering Potential $V(R)$

For a fixed η i.e for a given target projectile (A_1, A_2) combination, the scattering potential $V(R)$ in Eq. (2.9) is defined as the sum of Coulomb, proximity and angular momentum-dependent potentials, where temperature, deformation and orientation effects are duly included i.e.

$$\begin{aligned} V(R, \ell, T) &= V_c(R, Z_i, \beta_{\lambda i}, \theta_i, \phi, T) + V_p(R, A_i, \beta_{\lambda i}, \theta_i, \phi, T) \\ &+ V_\ell(R, A_i, \beta_{\lambda i}, \theta_i, \phi, T) \end{aligned} \tag{2.12}$$

For co-planar nuclei (Fig. 1.2) ϕ=0^0, and for spherical-plus-deformed nuclear collisions, only one orientation angle θ is enough, referring to the rotationally-symmetric deformed nucleus. Further details of deformation and orientation effects are discussed in section 2.2.5.

2.2.2 The Fragmentation potential $V(\eta)$

The temperature dependent collective potential energy or the fragmentation potential $V(\eta, R, T)$, appearing in Eq. (2.8), is calculated as,

$$\begin{aligned} V(\eta, R, \ell, T) &= -\sum_{i=1}^{2} B_i(A_i, Z_i, \beta_{\lambda i}, T) + V_c(R, Z_i, \beta_{\lambda i}, \theta_i, \phi, T) \\ &+ V_p(R, A_i, \beta_{\lambda i}, \theta_i, \phi, T) + V_\ell(R, A_i, \beta_{\lambda i}, \theta_i, \phi, T) \end{aligned} \tag{2.13}$$

The fragmentation potential $V(\eta)$, is calculated at a fixed distance $R = R_1 + R_2 + \Delta R$ for consideration of deformed and oriented reaction product, with

$$R_i(\alpha_i, T) = R_{0i}(T)[1 + \sum_{\lambda} \beta_{\lambda i} Y_\lambda^{(0)}(\alpha_i)], \tag{2.14}$$

and

$$R_{0i}(T) = [1.28A_i^{1/3} - 0.76 + 0.8A_i^{-1/3}] \times (1 + 0.0007T^2). \tag{2.15}$$

Here λ=2,3,4... . and α_i represent the angle that the radius vector R_i of the colliding nuclei makes with the symmetry axis (see Fig. 1.2), measured clockwise. The charges Z_i in Eq. (2.13) are fixed by minimizing the potential V(η), in the η_Z coordinate at each η-value.

The temperature T of the nucleus (in MeV) is related to the excitation energy E^*_{CN} of the compound nucleus, through a semi-empirical statistical relation as:

$$E^*_{CN} = E_{c.m.} + Q_{in} = aT^2 - T \qquad (MeV). \tag{2.16}$$

where a = A/9 to A/11 depending on the mass of the compound nucleus. Q_{in} is the entrance channel Q-value given by $Q_{in} = B_1 + B_2 - B_{CN}$ where B's are the binding

energies.

2.2.3 Temperature dependence of Binding energies

B_i (i=1,2) appearing in Eq. (2.13), are the binding energies of the two nuclei, available from the experimental data of Audi-Wapstra [29]. Wherever the experimental B's are not available, the theoretical binding energies of Möller *et al.* [30] are used. Note that within the Strutinsky renormalization procedure [28], the binding energies contain both the macroscopic (liquid drop part) and the microscopic (shell correction) part, which allows us to define the binding energy B of a nucleus at temperature T as the sum of liquid drop energy $V_{LDM}(T)$ and shell correction $\delta U(T)$ i.e

$$B(T) = V_{LDM}(T) + \delta U exp\left(- \frac{T^2}{{T_0}^2} \right). \tag{2.17}$$

The T dependent liquid drop part of the binding energy $V_{LDM}(T)$ is taken from Davidson *et al.* [31], based on the semi-empirical mass formula of Seeger [32], as

$$\begin{aligned} V_{LDM}(A,Z,T) &= \alpha(T)A + \beta(T)A^{\frac{2}{3}} + \left(\gamma(T) - \frac{\eta(T)}{A^{\frac{1}{3}}}\right)\left(\frac{I^2 + 2 \mid I \mid}{A}\right) \\ &\quad + \frac{Z^2}{R_0(T)A^{\frac{1}{3}}}\left(1 - \frac{0.7636}{Z^{\frac{2}{3}}} - \frac{2.29}{[R_0(T)A^{\frac{1}{3}}]^2}\right) + \delta(T)\frac{f(Z,A)}{A^{\frac{3}{4}}}, \end{aligned} \tag{2.18}$$

where

$$I = a_a(Z - N), \quad a_a = 1.0,$$

and, respectively, for even-even, even-odd, and odd-odd nuclei,

$$f(Z,A) = (-1, 0, 1).$$

For $T = 0$, Seeger [32] obtained the constants, by fitting all even-even nuclei and 488 odd-A nuclei available at that time, as

$$\alpha(0) = -16.11\text{MeV}, \quad \beta(0) = 20.21\text{MeV},$$

$$\gamma(0) = 20.65\text{MeV}, \quad \eta(0) = 48.00\text{MeV},$$

with the pairing energy term from Ref. [33],

$$\delta(0) = 33.0\text{MeV}.$$

For the large amount of data available now on ground-state binding energies, these constants of $V_{LDM}(T = 0)$ are re-fitted in [1–3] to get the experimental binding energies where shell corrections are determined from Myers and Swiatecki [34]. This was first done in [1, 2] for the 1995 Audi Wapstra Tables [35] of binding energies, and then in [3] for the 2003 Tables [29].

The T-dependence in the constants of Eq. (2.18) is obtained from Fig.1 of Davidson et al. [31], achieved by fitting to the canonical ensemble average of the excitation energy of over 300 nuclei for T$\leq$4 MeV, extrapolated linearly for higher temperatures.

For neutron-clusters of $x(\geq 1)$ nucleons, same procedure is used by defining [36,37] the binding energy of a cluster with x-neutrons as x times the binding energy of one-neutron (equivalently, the mass excess Δm_n=8.0713 MeV),

$$B(A_2 = xn) = x\Delta m_n, \tag{2.19}$$

The temperature dependent shell corrections in Eq. (2.17) are considered to vanish exponentially for higher excitation energies, giving T_0=1.5 MeV. Therefore only the liquid

drop part is present at still higher energies where the shell corrections vanish completely. The shell corrections according to the "empirical" formula of Myers and Swiatecki [34], for spherical shapes, are

$$\delta U = C\left[\frac{F(N)+F(Z)}{(A/2)^{\frac{2}{3}}} - cA^{\frac{1}{3}}\right] \tag{2.20}$$

where

$$F(X) = \frac{3}{5}\left(\frac{M_i^{\frac{5}{3}} - M_{i-1}^{\frac{5}{3}}}{M_i - M_{i-1}}\right)(X - M_{i-1}) - \frac{3}{5}\left(X^{\frac{5}{3}} - M_{i-1}^{\frac{5}{3}}\right) \tag{2.21}$$

with $X = N$ or Z, $M_{i-1} < X < M_i$ and M_i as the magic numbers 2, 8, 14 (or 20), 28, 50, 82, 126 and 184 for both neutrons and protons. The constants $C = 5.8\ MeV$ and $c = 0.26$.

The shell corrections play an important role in determining or empirical fitting of nuclear masses. In general, the microscopic shell correction, along with the liquid drop part, give a proper description of the binding energy of the nucleus. This method, however, does not give a proper description of light mass nuclei because of the inadequacy of shell model for such nuclei. For this reason, the macro-microscopic calculations of Möller *et al.* [30] are tabulated for $Z \geq 8$ only. Alternatively, one can use the empirical shell correction method of Myers-Swiatecki [34] which again is not satisfactory for light nuclei ($Z \leq 16$). Gupta and collaborators have modified this empirical method and obtained a better description of the shell corrections for the light as well as heavy mass region, i.e, $1 \leq Z \leq 118$ [2, 3].

2.2.4 The Coulomb potential

Coulomb potential describes the force of repulsion between two interacting nuclei due to their charges. It acts along the line joining the two nuclei. The Coulomb potential for

two interacting spherical nuclei is given as

$$V_c = \frac{Z_1 Z_2 e^2}{R} \tag{2.22}$$

For deformed and oriented interacting nuclei, different authors [38–41] have given different expressions. The Coulomb potential for two interacting hot, deformed and oriented nuclei is given as [38]:

$$V_c(Z_i, \beta_{\lambda i}, \theta_i, T) = \frac{Z_1 Z_2 e^2}{R(T)} + 3 Z_1 Z_2 e^2 \sum_{\lambda, i=1,2} \frac{R_i^{\lambda}(\alpha_i, T)}{(2\lambda+1) R(T)^{\lambda+1}} Y_{\lambda}^{(0)}(\theta_i) \left[\beta_{\lambda i} + \frac{4}{7} \beta_{\lambda i}^2 Y_{\lambda}^{(0)}(\theta_i)\right], \tag{2.23}$$

with R_i from Eq. (2.14). $Y_{\lambda}^{(0)}(\theta_i)$ are the spherical harmonics function.

2.2.5 The Proximity Potential for deformed, oriented, co-planar nuclei

When two nuclear surfaces approach each other within a small distance, comparable to the surface thickness of interacting nuclei ($\approx 2fm$), or when a nucleus is at the verge of dividing into two fragments, then the two surfaces face each other across a small crevice. In both cases, the surface energy term alone could not give rise to the strong attraction that is observed when the two surfaces are brought in close proximity. Such additional attractive forces are called proximity forces and the additional potential due to these forces is called the proximity potential.

Blocki *et al.* [42] have reanalyzed and extended a theorem, originally due to Deryagin [43], according to which the force between two gently curved surfaces in close proximity is proportional to the interaction potential per unit area between the two flat surfaces. The

original expression of Blocki based on the pocket formula was for spherical nuclei, and is given by

$$\begin{aligned} V_P(s_0) &= f(sh., geo.)\Phi(s_0) \\ &= 4\pi\bar{R}\gamma b\Phi(s_0). \end{aligned} \tag{2.24}$$

$\Phi(s_0)$ is the universal function, independent of the shapes of nuclei or the geometry of nuclear system, but depends on the minimum separation distance s_0, as

$$\Phi(s_0) = \begin{cases} -\frac{1}{2}(s_0 - 2.54)^2 - 0.0852(s_0 - 2.54)^3 \\ -3.437exp(-\frac{s_0}{0.75}) \end{cases} \tag{2.25}$$

respectively, for $s_0 \leq 1.2511$ and $s_0 \geq 1.2511$. Here, s_0 is defined in units of b, i.e. s_0 is s_0/b, where b is the diffuseness defined in Eq. 2.28. This function is defined for negative (the overlap region), zero (touching configuration) and positive values of s_0. s_0, distance of closest approach defined in Fig. 1.2 depends on deformations and orientations of reactants and products. For a fixed R, the minimum distance s_0 is defined as

$$s_0 = R - R_1 - R_2 \tag{2.26}$$

where R_i is defined in Eq. (2.14). b is the diffuseness of the nuclear surface given by

$$b = \Big[\pi/2\sqrt{3}\ln 9\Big]_{t_{10-90}} \tag{2.27}$$

where t_{10-90} is the thickness of the surface in which the density profile changes from 90%

to 10%. The value of b∼1 fm. However, the temperature dependent b is given as

$$b(T) = 0.99(1 + 0.009T^2) \tag{2.28}$$

Different values of diffuseness coefficients have been used to explore the data, and the role of b in the reaction dynamics of ^{112}Xe nucleus is studied in chapter 7.

The γ is the specific nuclear surface tension given by

$$\gamma = 0.9517 \left[1 - 1.7826 \left(\frac{N-Z}{A}\right)^2\right] MeVfm^{-2} \tag{2.29}$$

The proximity potential [38] for hot deformed nuclei is given as

$$V_p(A_i, \beta_{\lambda i}, \theta_i, T) = 4\pi \bar{R}(T)\gamma b(T)\Phi(s_0(T)). \tag{2.30}$$

$\overline{R}$ is the mean curvature radius of the reaction partners, characterizing the gap, which for spherical nuclei is given by

$$\overline{R} = \frac{R_1 R_2}{R_1 + R_2} \tag{2.31}$$

For the axially symmetric shapes, the nuclear radius parameter (to all higher multipole orders λ=2,3,4,....) is given by Eqs. (2.14) and (2.15). In terms of the radii of curvature R_{i1} and R_{i2} in the principal planes of curvature of each of the two nuclei (i=1,2) at the points of closest approach, the mean curvature radius $\bar{R}$ for deformed, oriented nuclei is given by

$$\begin{aligned} \frac{1}{\bar{R}^2} &= \frac{1}{R_{11}R_{12}} + \frac{1}{R_{21}R_{22}} + \left[\frac{1}{R_{11}R_{21}} + \frac{1}{R_{12}R_{22}}\right] sin^2\phi \\ &+ \left[\frac{1}{R_{11}R_{22}} + \frac{1}{R_{21}R_{12}}\right] cos^2\phi. \end{aligned} \tag{2.32}$$

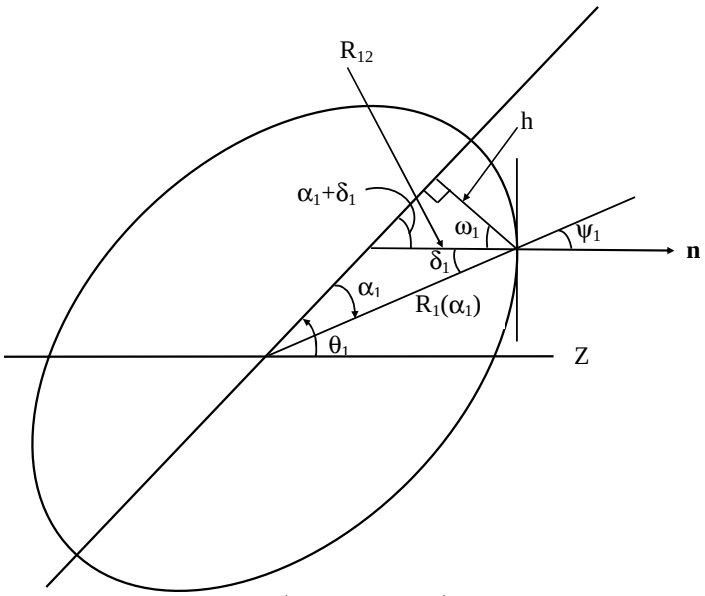

Figure 2.1 An axially symmetric (quadrupole) deformed and oriented nucleus, showing the nuclear radius parameter $R_1(\alpha_1)$ and the geometry associated with the principal radius of curvature $R_{12}(\alpha_1)$.

Here, ϕ is the azimuthal angle between the principal planes of curvature of two nuclei (for co-planar nuclei ϕ=0^0). The four principal radii of curvature are

$$\begin{aligned} R_{i1}(\alpha_i) &= \frac{\left[R_i^2(\alpha_i) + R_i'^2(\alpha_i)\right]^{3/2}}{R_i^2(\alpha_i) + 2R_i'^2(\alpha_i) - R_i(\alpha_i)R_i''(\alpha_i)} \\ R_{i2}(\alpha_i) &= \frac{R_i(\alpha_i)sin\alpha_i}{cos(\pi/2 - \alpha_i - \delta_i)}. \end{aligned} \tag{2.33}$$

where, $R_i'(\alpha_i)$ and $R_i''(\alpha_i)$ are the first and second order derivatives of $R_i(\alpha_i)$ with respect to α_i, respectively. For the derivation of the radius of curvature R_{i1}, see [44] and it follows from Fig. 2.1, and Ref. [45], that $R_{i2} = h/cos\omega_i$, with $h = R_i(\alpha_i)sin\alpha_i$ and $\omega_i = \pi/2 - \alpha_i - \delta_i$. Also, for **n** to be a normal vector

$$tan\delta_i = -\frac{R_i'(\alpha_i)}{R_i(\alpha_i)}. \tag{2.34}$$

Note that $R_{i1}(\alpha_i) = R_{i2}(\alpha_i)$, respectively, for $\alpha_1 = 0^0$ or 180^0 and $\alpha_2 = 180^0$ or 360^0. For deformed, oriented nuclei configuration, the minimum distance s_0 (see Fig. 1.2) in Eq.

(2.26) is

$$s_0 = R - X_1 - X_2 \tag{2.35}$$

with the projections X_i along the Z-axis given as

$$\begin{aligned} X_1 &= R_1(\alpha_1)cos(\theta_1 - \alpha_1) \\ X_2 &= R_2(\alpha_2)cos(180 + \theta_2 - \alpha_2) \end{aligned} \tag{2.36}$$

and the minimization conditions on s_0,

$$\frac{\partial s_0}{\partial \alpha_1} = \frac{\partial s_0}{\partial \alpha_2} = 0, \tag{2.37}$$

resulting in

$$\begin{aligned} \tan(\theta_1 - \alpha_1) &= -\frac{R_1'(\alpha_1)}{R_1(\alpha_1)} \\ \tan(180 + \theta_2 - \alpha_2) &= -\frac{R_2'(\alpha_2)}{R_2(\alpha_2)}. \end{aligned} \tag{2.38}$$

Comparing Eqs. (2.34) and (2.38), we get

$$\begin{aligned} \delta_1 &= \theta_1 - \alpha_1 \\ \delta_2 &= 180 + \theta_2 - \alpha_2, \end{aligned} \tag{2.39}$$

to be used in Eq. (2.33). Thus, for the given θ_1 and θ_2, X_1 and X_2 are obtained for the angles α_1 and α_2 satisfying the minimization conditions shown in Eq. (2.38). It may be noted that the Eq. (2.38) refer to perpendiculars (normal vectors) at the points P_1 and P_2 in Fig. 1.2. In other words, if the distance s_0 were to be shortest, the perpendicular conditions Eq. (2.38) must be used which would apparently give Eq. (2.36) for X_i.

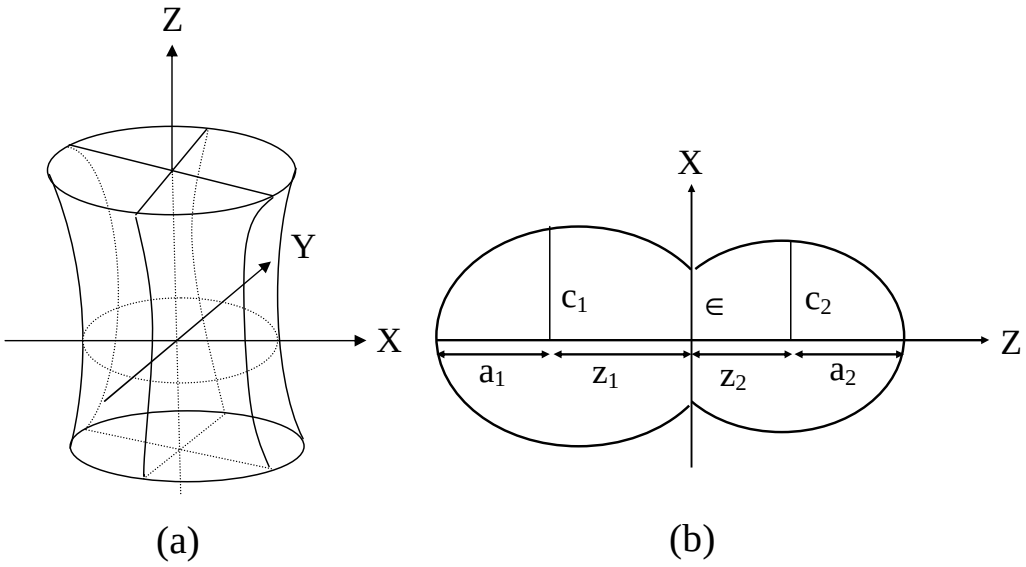

Figure 2.2 (a) Schematic representation of a hyperboloid of revolution in one sheet. (b) Sample nuclear shape formed in two center shell model [46].

Eq. (2.30) is valid for zero (touching configuration) and positive values of s_0, but is also used for negative s_0. As the two nuclei overlap ($s_0 < 0$), a crevice is formed and, in an adiabatic approximation, the system adjusts its shape parameters such that the two colliding nuclei form a single indented body in the form of a single hyperboloid of one sheet with a hyperboloidal crevice, as shown in Fig. 2.2(a). For such a necked system, shown in Fig. 2.2(b), following Blocki *et al.* [42], the proximity potential is obtained by Gupta and collaborators [15, 47] as

$$V_P(s_0) = \pi\gamma b^2 \Phi_1(s_0 = 0) \frac{(c_1^2 + c_2^2 - 2\epsilon^2)}{(z_1^2 + z_2^2)} \tag{2.40}$$

where $\Phi_1(s_0 = 0)$=-2.0306 is the first moment of the universal function Φ at $s_0 = 0$, and c_i, z_i and ϵ are the shape parameters in Fig. 2.2(b). Apparently, for two equal nuclei, $z_1 = z_2$ and $c_1 = c_2$.

2.2.6 Rotational Energy due to angular momentum

The rotational motion of nucleons gives an additional energy due to the angular momentum ℓ, defined as

$$V_\ell(R, A_i, \beta_{\lambda i}, \theta_i, T) = \frac{\hbar^2 \ell(\ell+1)}{2I(T)} \tag{2.41}$$

where I is the moment of inertia. $I(T)$=I_{NS}=μR^2, is the non-sticking limit of moment of inertia, where $\mu = \frac{A_1 A_2}{A_1+A_2} m$ is the reduced mass with m as the nucleon mass. In the complete sticking limit, the moment of inertia I is given as,

$$I_s(T) = \mu R^2 + \frac{2}{5} A_1 m R_1^2(\alpha_1, T) + \frac{2}{5} A_2 m R_2^2(\alpha_2, T). \tag{2.42}$$

with R_i from Eq. (2.14). It is relevant to mention here that the experimentally extracted value of angular momentum is based on the moment of inertia in non-sticking limit (i.e. $I_{NS} = \mu R^2$) [48]. It means that fragment emission is punctual. In a recent study [8] we find that the sticking limit is more appropriate to calculate the fusion-fission cross sections in view of the use of proximity interaction (nuclear surface $\approx$ 2fm). The use of I_S approach consequently results in to large limiting value of angular momentum. On the other hand, non sticking limit is appropriate to estimate the fission fragment anisotropies.

2.2.7 Classical Hydrodynamical Mass Parameters

The kinetic energy part of the Hamiltonian in Eq. (2.8) enters through the mass parameters. The classical mass parameters of Kröger and Scheid [49] are used here. The model of Kröger and Scheid is based on the hydrodynamical flow, as shown in Fig. 2.3. This model gives a simple analytical expression, whose predictions are shown to compare nicely with the microscopic cranking model calculations. For the $B_{\eta\eta}$ mass we get,

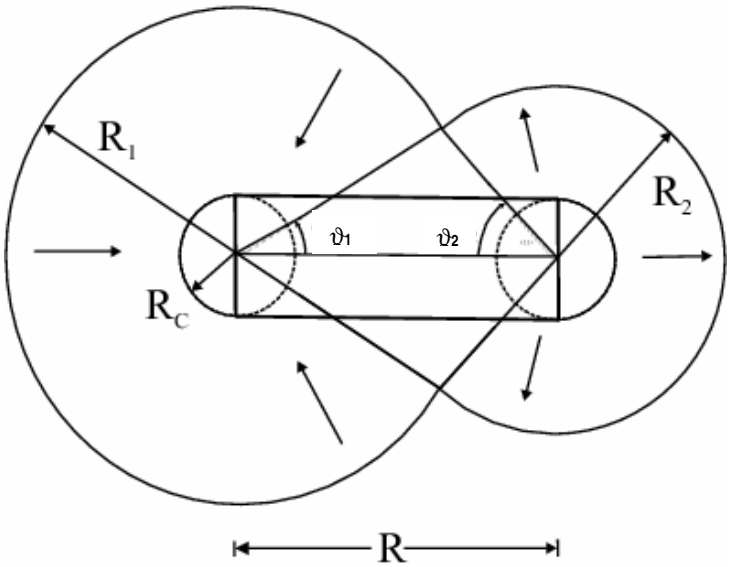

Figure 2.3 The geometry of the classical hydrodynamical model of Kröger and Scheid for calculating the mass parameter $B_{\eta\eta}$.

$$B_{\eta\eta} = \frac{AmR^2}{4}\left[\frac{v_t(1+\gamma)}{v_c(1+\delta^2)} - 1\right] \tag{2.43}$$

with

$$\gamma = \frac{R_c}{2R}\left[\frac{1}{1+\cos\vartheta_1}\left(1-\frac{R_c}{R_1}\right) + \frac{1}{1+\cos\vartheta_2}\left(1-\frac{R_c}{R_2}\right)\right] \tag{2.44}$$

$$\delta = \frac{1}{2R}\left[(1-\cos\vartheta_1)(R_1-R_c) + (1-\cos\vartheta_2)(R_2-R_c)\right] \tag{2.45}$$

$$v_c = \pi R_c^2 R \tag{2.46}$$

The angles ϑ_1 and ϑ_2 and geometry of the model are shown in Fig. 2.3. For $\vartheta_1 = \vartheta_2 = 0$, $\delta = 0$ which corresponds to two touching spheres. $R_c(\neq 0)$ is the radius of a cylinder of length R, having a homogeneous flow in it; whose existence is assumed for the

mass transfer between the two spherical fragments. This formalism have been generalized for deformed nuclei by using the radii R_1 and R_2 for hot deformed nuclei, given by Eq. (2.14).

2.2.8 Solution of the stationary Schrödinger equation and the fragment's preformation probability P_0

Once the Hamiltonian of Eq. (2.7) is established, the Schrödinger equation in mass fragmentation co-ordinate η can be solved. On solving Eq. (2.8) numerically, $|\psi^{\nu}(\eta)|^2$ gives the probability P_0 of finding the mass fragmentation η at a fixed R on the decay path.

$$P_0(A_2) \propto |\psi^{\nu}(A_2)|^2 \tag{2.47}$$

with ν=0,1,2,3... referring to ground state (ν=0) and excited state solutions. Starting from the nuclear ground state in spontaneous fission or cluster decay, and to have complete adiabaticity, only the lowest vibrational state $\nu = 0$ is occupied. Then, the mass (or charge) distribution yield, proportional to the probability $|\psi^{(0)}(\eta)|^2$ (or $|\psi^{(0)}(\eta_Z)|^2$) of finding a certain mass (or charge) fragmentation η (or η_Z) at a position R on the decay path, when scaled to, say, mass A_2 of one of the fragments ($d\eta = \frac{2}{A}$) is given by:

$$P_0 = |\psi_R^{(0)}(A_2)|^2 \frac{2}{A} \sqrt{B_{\eta\eta}(A_2)}). \tag{2.48}$$

However, if the system is excited or we allow interaction between various degrees of freedom, higher values of ν would also contribute. These enter via the excitation of higher vibrational states, and through the temperature dependent potential V and masses B_{ij}.

The effect of adding temperature on potential V and masses B_{ij} is to reduce the shell effects in them, resulting finally in the liquid drop potential V_{LDM} and smoothed (aver-

aged) masses $\bar{B}_{ij}$ for the systems to be very hot. Apparently, cold fission means taking both the potential V and masses B_{ij} with full shell effects included in them and hot fission means using the V_{LDM} and smoothed (averaged) masses $\bar{B}_{ij}$. The possible consequence of such excitations are included here by assuming a Boltzmann like occupation of excited states

$$|\psi(\eta)|^2 = \sum_{\nu=0}^{\infty} |\psi^{\nu}(\eta)|^2 \exp\left(-\frac{E_{\eta}^{\nu}}{T}\right) \tag{2.49}$$

Note that we are dealing here with a directly measurable quantity, the mass (or charge) asymmetry, which works dynamically as mass (or charge) transfer coordinate. Thus, the calculated yields $P_0(A_i)$ (or $P_0(Z_i)$) are directly comparable with experiments. The nuclear shape, once minimized in the neck ε and deformation coordinates β_1 and β_2 at a given R ($\approx R_{saddle}$), remains fixed for both the mass and charge distributions of fission or decay fragments.

For the competing, noncompound, quasi-fission (qf) decay channel, the incoming nuclei keep their identity, and hence the preformation factor P_0=1 for η_i in case of qf. The property of depicting structural effects comes via the preformation probability, which is missing in the other statistical models.

2.2.9 Penetration Probability P

For R-motion, instead of solving the Schrödinger Eq. (2.9), we use the WKB approximation to calculate the penetration probability P. For each η-value, the potential $V(R)$ for $R \geq R_t$ is calculated by using Eq. (2.12) and for $R < R_t$ it is parameterized simply as a polynomial of degree two in R, so that

$$V(R) = \begin{cases} a_1 R + a_2 R^2 & for \quad R_0 \leq R \leq R_t \\ V_c + V_p + V_\ell & for \quad R \geq R_t \end{cases} \tag{2.50}$$

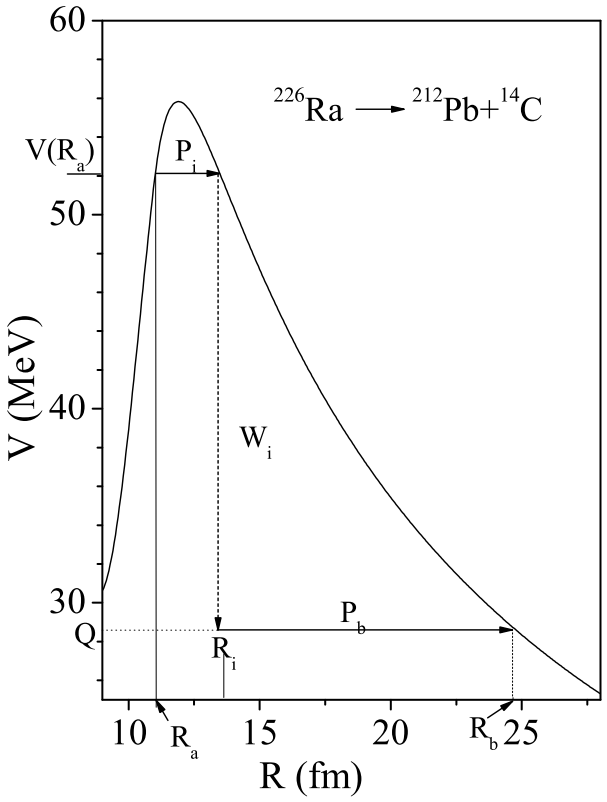

Figure 2.4 A scattering potential for ^{226}Ra* $\rightarrow$^{212}Pb+^{14}C reaction with characteristic quantities [18].

A typical scattering potential, for ^{226}Ra $\rightarrow$^{212}Pb+^{14}C taken from [18] is shown in Fig. 2.4, calculated by using Eq. (2.12) for ℓ=0 case. The path of the penetration and the related quantities are also shown .

The constants a_i $(i = 1, 2)$ occurring in the polynomial, are determined by using the following boundary conditions.

1. At $R = R_0$, $V(R) = Q$

2. At $R = R_t$, $V(R) = V(R_t)$

The first (inner) turning point R_a is chosen at R_a= R_t + ΔR, where R_t=R_1+R_2 and the outer turning point is taken at R_b to give the Q-value of the reaction, i.e., $V(R_b) = Q$. This means that the transmission probability P consists of three contributions

1. The penetrability P_i from R_a to R_i,

2. the (inner) de-excitation probability W_i at R_i and

3. the penetrability P_b from R_i to R_b

giving the penetration probability as

$$P = P_i W_i P_b. \tag{2.51}$$

The shifting of first turning point from R_t to R_0 gives the penetrability calculations similar to Shi and Swiatecki [50] for spherical nuclei, which is known not to fit the experimental data without the adjustment of assault frequency (ν_0).

Following the excitation model of M. Greiner and W. Scheid [51], the de-excitation probability W_i is given as

$$W_i = \exp(-bE_i) \tag{2.52}$$

This means that the de-excitation process is restricted to only a single transition. If the parameter b were allowed to depend on R_i, it should then become a process of multiple de-excitation and proceed as step-like process. For a heavy cluster decay into the excited states of the daughter nucleus, the $b = 0$ is assumed [51], which means

W_i=1, therefore,

$$P = P_i P_b, \tag{2.53}$$

where P_i and P_b are calculated by using WKB approximation, as

$$P_i = \exp\left[-\frac{2}{\hbar}\int_{R_a}^{R_i}\{2\mu[V(R) - V(R_i)]\}^{1/2}dR\right] \tag{2.54}$$

and

$$P_b = \exp\left[-\frac{2}{\hbar}\int_{R_i}^{R_b}\{2\mu[V(R)-Q]\}^{1/2}dR\right]. \tag{2.55}$$

Here R_a and R_b are, respectively, the first and second turning points. This means that the tunneling begins at $R = R_a$ and terminates at $R = R_b$, with $V(R_b) = Q$-value for ground state decay. The integrals of the Eqs. (2.54) and (2.55) are solved analytically by parameterizing the above calculated potential $V(R)$, as prescribed in [14, 15]. This procedure is followed for the ground state decay however for the decay from an excited

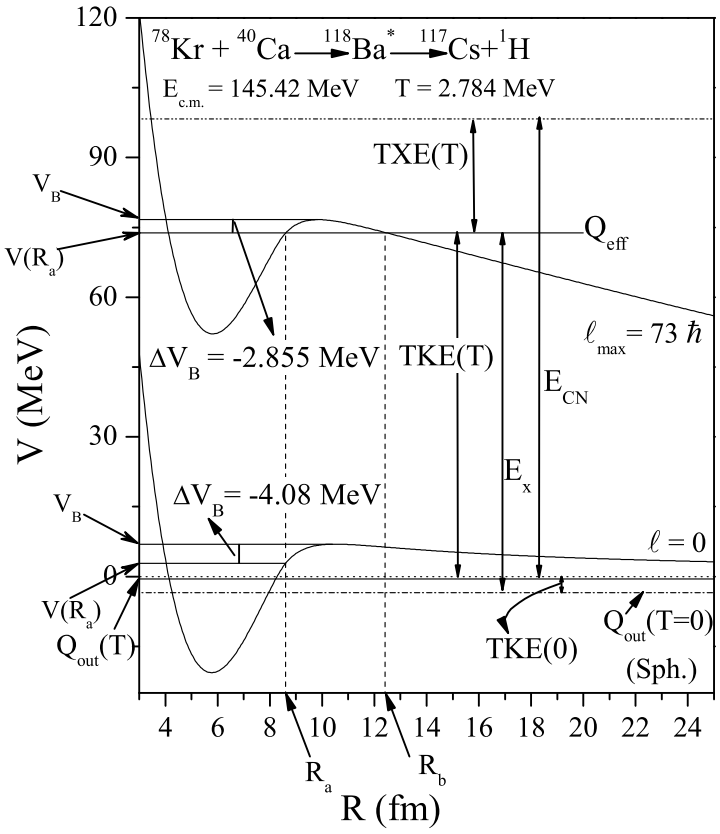

Figure 2.5 The scattering potential for ^{118}Ba* $\rightarrow$^{117}Cs+^{1}H at fixed temperature T=2.784 MeV (equivalently, $E_{c.m.}$=145.42 MeV), at extreme values of angular momentum ℓ. The barrier lowering parameter defined as $\triangle$V$_B$=V(R$_a$)-V$_B$ is also shown for ℓ=0 and ℓ=ℓ_{max} values [10].

(hot) compound nucleus with total excitation energy TXE of decaying fragments, we

consider

$$V(R_a) \;=\; V(R_b) = Q_{eff} = TKE + Q_{out} \tag{2.56}$$

as shown in Fig. 2.5. Now P=P_b given by Eq. 2.55 where Q is replaced by Q_{eff} and the limits of integration are from R_a to R_b as depicted in Fig. 2.5.

Therefore P is given as

$$P = exp[-\frac{2}{\hbar}\int_{R_a}^{R_b}\{2\mu[V(R) - Q_{eff}]\}^{1/2}dR], \tag{2.57}$$

In the following section, Eqs. (2.47) and (2.57) are used for P_0 and P for calculating the cross sections.

2.3 The Dynamical Cluster-decay Model (DCM) for hot and rotating compound nucleus

The dynamical cluster decay model (DCM) [1]- [13] for the decay of hot and rotating nucleus (i.e. angular momentum $\ell \neq 0$ and temperature $T \neq 0$) is a reformulation of the preformed cluster-decay model (PCM) [14]- [19] for ground-state (ℓ=0, T=0) decay of a nucleus. The DCM (like PCM) is based on the dynamical (or quantum mechanical) fragmentation theory [20]- [27]. The deformation and orientation effects of the decay products are duly taken care along with the temperature and angular momentum effects in the decay of excited compound nucleus within DCM. The co-ordinates η and R of fragmentation theory in DCM, characterize, respectively,

(i) the nucleon-division (or -exchange) between outgoing fragments, and

(ii) the transfer of kinetic energy of incident channel ($E_{c.m.}$) to internal excitation (total

excitation or total kinetic energy, TXE or TKE) of the outgoing channel, since the fixed $R = R_a$, at which the process is calculated, depends on temperature T as well as on η, i.e. $R(T, \eta)$. This energy transfer process follows the relation

$$E^*_{CN} + Q_{out}(T) = TKE(T) + TXE(T). \tag{2.58}$$

The CN excitation energy E^*_{CN} is related to temperature T (in MeV) via Eq.(2.16).

Using the decoupled approximation to R- and η-motions, the DCM defines the decay cross-section, in terms of partial waves, as [1]- [13]

$$\sigma = \sum_{\ell=0}^{\ell_{max}} \sigma_\ell = \frac{\pi}{k^2} \sum_{\ell=0}^{\ell_{max}} (2\ell + 1) P_0 P; \qquad k = \sqrt{\frac{2\mu E_{c.m.}}{\hbar^2}} \tag{2.59}$$

where, P_0, the preformation probability, refers to η-motion and P, the penetrability, to R-motion, discussed in Sec. 2.2.8 and Sec. 2.2.9 respectively. Apparently, for ℓ=0 (s-wave) $\sigma_0 = \frac{\pi}{k^2} P_0 P$, which is an equivalent of decay constant $\lambda = \nu_0 P_0 P$ (or decay half-life $T_{1/2} = ln2/\lambda$) with ν_0 as the barrier assault frequency. In other words, σ_0 and λ differ through a constant only. Thus, like in PCM, here the complex fragments (both light and heavy fragments) are treated as the dynamical collective mass motion of *preformed clusters or fragments* through the barrier. The structure information of the CN enters the model via the preformation probabilities P_0 (also known as the spectroscopic factors) of the fragments given by the solution of stationary Schrödinger equation in η (see Eq. 2.8) with ν=0,1,2,3... referring to ground state (ν=0) and excited state solution, at a fixed R=R_a, the first turning point of the penetration path shown in Fig. 2.5.

For the decay of a hot CN, we choose the first turning point as

$$R_a(T) = R_t + \Delta R(\eta, T) \tag{2.60}$$

where

$$R_t = R_1(\alpha_1, T) + R_2(\alpha_1, T) \tag{2.61}$$

$\Delta R(T)$ is the neck-length parameter that assimilates the neck formation effects. This method of introducing a neck length parameter is similar to that used in both the scission-point [52] and saddle-point [53, 54] statistical fission models. The R_i are radius vectors which are also made temperature dependent, given by Eqs.(2.14) and (2.15).

The corresponding potential $V(R_a)$ acts like an effective Q-value, Q_{eff}, for the decay of the hot CN at temperature T, to two exit-channel fragments observed in *ground state* (T=0), defined by

$$\begin{aligned} Q_{eff}(T) &= B(T) - [B_L(T=0) + B_H(T=0)] \\ &= TKE(T) = V(R_a(T)) \end{aligned} \tag{2.62}$$

with B's as the respective binding energies.

The above defined decay of a hot CN into two cold (T=0) fragments, via Eq. (2.62), could apparently be achieved only by emitting some light particle (s) (LPs), like n, p, α, or γ-rays of energy

$$\begin{aligned} E_x &= B(T) - B(0) = Q_{eff}(T) - Q_{out}(T=0) \\ &= TKE(T) - TKE(T=0) \end{aligned} \tag{2.63}$$

which is zero for the g.s. decay, like for cluster radioactivity [55]. Note that the second equality in Eq. (2.63) is not defined for a negative $Q_{out}(T=0)$ system since the negative TKE(T=0) has no meaning. Apparently, Eq. (2.63) w.r.t (2.62) suggest that the emission of light-particles starts early in the decay process. The exit channel fragments

in Eq. (2.62) are then obtained in the ground-state with TKE(T=0), as can be seen by calculating $E^*_{CN} - E_x$ (i.e the remaining excitation energy of the decaying system) is then:

$$E^*_{CN} - E_x = |Q_{out}(T)| + TKE(T = 0) + TXE(T). \tag{2.64}$$

Which shows that the exit channel fragments are obtained with their TKE in the ground state i.e TKE (T=0). The excitation energy TXE(T) (not treated here) is used in, the secondary emission of light particles from the fragments which are otherwise in their ground states with TKE(T=0) in the radial motion. Thus, by defining $Q_{eff}(T)$ as in Eq. (2.62), in this model we treat the LP emission at par with the heavy fragments, called intermediate mass fragments ($IMFs$) emission. Thus, in this model a non-statistical dynamical treatment is attempted for not only the emission of $IMFs$ but also of multiple LPs, understood as the statistically evaporated particles in a CN emission. It may be reminded here that the statistical model interpretation of $IMFs$ is not as good as it is for the LP production [52–54]- [56–58].

In terms of $Q_{eff}(T)$, the second turning point R_b satisfies

$$V(R_a, \ell) = V(R_b, \ell) = Q_{eff}(T, \ell) = TKE(T). \tag{2.65}$$

with the ℓ-dependence of R_a defined by

$$V(R_a) = Q_{eff}(T, \ell = 0), \tag{2.66}$$

i.e the decay path, defined in Eq. 2.65 for each ℓ, begin at R_a, fixed for the ℓ=0 case and it means that the R_a is the same for all ℓ-values, given by the above equation (Eq. 2.66), and that $V(R_a, \ell)$ acts like an effective Q-value, $Q_{eff}(T, \ell)$, given by the total kinetic

energy $TKE(T)$. Then, using Eq. (2.65), $R_b(\ell)$ is given by the ℓ-dependent scattering potentials, at fixed T for coplanar nuclei, as in Eq. (2.12), which is normalized to the exit channel binding energy $B_L(T) + B_H(T)$. The potential illustrated in Fig. 2.5, for ^{118}Ba$^* \rightarrow ^{117}$Cs+^{1}H, at extreme ℓ-values, shows that as the ℓ-value increases, the Q_{eff}(T) value increases and hence $V(R_a, \ell)$ also increases, since the decay path for all the ℓ-values begins at $R = R_a$.

Finally, the ℓ_{max}-value in Eq. (2.59) is the critical ℓ-value, in terms of the bombarding energy $E_{c.m.}$, the reduced mass μ and the first turning point R_a of the entrance channel η_{in}, given by

$$\ell_c = R_a\sqrt{2\mu[E_{c.m.} - V(R_a, \eta_{in}, \ell = 0)]}/\hbar, \tag{2.67}$$

or, alternatively, it could be fixed for the vanishing of fusion barrier of the incoming channel, called ℓ_{fus}, or else the ℓ-value where the light-particle cross-section $\sigma_{LP}(\ell) \rightarrow 0$. This, however, could also be taken as a variable parameter [53, 59].

2.3.1 Index of "barrier lowering"

The overestimation of cross sections within coupled channel calculations at sub barrier energies is termed as the fusion hindrance phenomenon. This phenomena for fusion-evaporation cross-sections in reactions such as ^{58}Ni+^{58}Ni, ^{58}Ni+^{54}Fe, ^{64}Ni+^{64}Ni and ^{64}Ni+^{100}Mo, are one of the topic of current research in Nuclear Physics [60]- [62]. Its explanation requires the modification of the shape of the potential and this is supported well within DCM in terms of its index of barrier lowering, ΔV_B. This property of 'lowering of barriers' (without modifying the depth of potential pocket) at sub-barrier energies arises in DCM in a simple way via its fitting of the neck-length parameter. The choice of parameter R_a (equivalently, ΔR) for the best fit to the data corresponds to the effects of "barrier lowering" in it for each decay channel, defined for each ℓ as the difference between

$V_B(\ell)$ and $V(R_a, \ell)$, the barrier height and the actually used barrier, as

$$\Delta V_B(\ell) = V(R_a, \ell) - V_B(\ell). \tag{2.68}$$

Note, ΔV_B for each ℓ is defined as a negative quantity as the actual barrier height is effectively lowered, as is also illustrated in Fig. 2.5 for extreme ℓ values. It is worth noting in Fig. 2.5 that, ΔV_B is higher for lower angular momentum value. Though not plotted, but ΔV_B decreases with increase in energy, being large at lower energies. This is discussed in the following chapters.

2.3.2 Fission fragment anisotropy

The dependence of anisotropy on different quantities is explored through DCM within SSPM approach [63]. The fission fragment anisotropy A is related to the total ℓ value (equivalently ℓ_{max}) of the CN, the effective moment-of-inertia I_{eff} of the fissioning nucleus in the transition state (at the saddle point), and the temperature T at the saddle point, as

$$A = 1 + \langle \ell^2 \rangle / 4K_0^2, \tag{2.69}$$

with

$$K_0^2 = T \times I_{eff}/\hbar^2, \tag{2.70}$$

Here I_{eff} is calculated by using the finite-range rotating liquid drop model [64] with T being the temperature of the fissioning nucleus. The value of ℓ_{max} depends on the use of I_S or I_{NS} in the ℓ-dependent potential V_ℓ [Eq. (2.41)]. For fission fragment anisotropies the non-sticking approach is found more suitable contrary to the fitting of evaporation residue and fission cross-sections, where sticking moment of inertia is found more suitable [8, 11].

Bibliography

[1] R. K. Gupta, R. Kumar, N. K. Dhiman, M. Balasubraniam, W. Scheid, and C. Beck, Phys. Rev. C **68**, 014610 (2003).

[2] M. Balasubraniam, R. Kumar, R. K. Gupta, C. Beck, and W. Scheid, J. Phys. G **29**, 2703 (2003).

[3] B. B. Singh, M. K. Sharma, and R. K. Gupta, Phys. Rev. C **77**, 054613 (2008).

[4] R. K. Gupta, M. Balasubraniam, R. Kumar, D. Singh, and C. Beck, Nucl. Phys. A **738**, 479c (2004). R. K. Gupta, M. Balasubramaniam, R. Kumar, D. Singh, C. Beck, and W. Greiner, Phys. Rev. C **71**, 014601 (2005).

[5] B. B. Singh, M. K. Sharma, R. K. Gupta, and W. Greiner, Int. J. Mod. Phys. E **15**, 699 (2006).

[6] S. Kanwar, M. K. Sharma, B. B. Singh, R. K. Gupta, and W. Greiner, Int. J. Mod. Phys. E **18**, 1453 (2009). S. K. Arun, R. Kumar, and R. K. Gupta, J. Phys. G: Nucl. Part. Phys. **36**, 085105 (2009).

[7] M. K. Sharma, S. Kanwar, G. Sawhney, R. K. Gupta, and W. Greiner, J. Phys. G: Nucl. Part. Phys. **38**, 055104 (2011); D. Jain, R. Kumar, M. K. Sharma, and R. K. Gupta, Phys. Rev. C **85**, 024615 (2012).

[8] M. K. Sharma, G. Sawhney, R. K. Gupta, and W. Greiner, J. Phys. G: Nucl. Part. Phys. **38**, 105101 (2011). M. K. Sharma, G. Sawhney, S. Kanwar, and R. K. Gupta, Mod. Phys. Lett. A **25**, 2022 (2010).

[9] G. Sawhney and M. K. Sharma, Eur. Phys. J. A **48**, 57 (2012). M. K. Sharma, S. Kanwar, G. Sawhney, and R. K. Gupta, Phys. Rev. C **85**, 064602 (2012).

[10] M. Kaur, R. Kumar, and M. K. Sharma, Phys. Rev. C **85**, 014609 (2012).

[11] M. Kaur and M. K. Sharma, Phys. Rev. C **85**, 054605 (2012). M. Kaur, M. K. Sharma and Raj K. Gupta, Phys. Rev. C **86**, 064610 (2012).

[12] M. Kaur and Manoj K. Sharma, *International Conference On Recent Trends in Nuclear Physics-2012*, published in AIP conf. proc. **1524**, pp.151-154 (2013).

[13] K. Sandhu, M. K. Sharma, and R. K. Gupta, Phys. Rev. C **85**, 024604 (2012). G. Kaur and M. K. Sharma, Nucl. Phys. A **884**, 36 (2012). G. Kaur and M. K. Sharma, Phys. Rev. C **87**, 044601 (2013).

[14] S. S. Malik and R. K. Gupta, Phys. Rev. C **39**, 1992 (1989).

[15] S. Kumar and R. K. Gupta, Phys. Rev. C **55**, 218 (1997).

[16] S. K. Arun, R. K. Gupta, B. B. Singh, S. Kanwar, and M. K. Sharma, Phys. Rev. C **79**, 064616 (2009).

[17] S. K. Arun, R. K. Gupta, S. Kanwar, B. B. Singh, and M. K. Sharma, Phys. Rev. C **80**, 034317 (2009).

[18] G. Sawhney, M. K. Sharma, and R. K. Gupta, Phys. Rev. C **83**, 064610 (2011).

[19] R. Kumar and M. K. Sharma, Phys. Rev. C **85**, 054612 (2012).

[20] J. Maruhn and W. Greiner, Phys. Rev. Lett. **32**, 548 (1974).

[21] R. K. Gupta, W. Scheid, and W. Greiner, Phys. Rev. Lett. **35**, 353 (1975).

[22] A. Săndulescu, R. K. Gupta, W. Scheid, and W. Greiner, Phys. Lett. B **60**, 225 (1976). R. K. Gupta, A. Săndulescu, and W. Greiner, Phys. Lett. B **67**, 257 (1977); Rev. Roum. Phys. **23**, 51 (1978).

[23] S. Yamaji, W. Scheid, H. J. Fink, and W. Greiner, Z. Phys. A **278**, 69 (1976).S. Yamaji, W. Scheid, H. J. Fink, and W. Greiner, J. Phys. G: Nucl. Phys. **2**, L189 (1976). S. Yamaji, K. H. Ziegenhain, H. J. Fink, W. Greiner, and W. Scheid, J. Phys. G: Nucl. Phys. **3**, 1283 (1977).

[24] R. K. Gupta, A. Săndulescu, and W. Greiner, Z. Naturforsch. **32a**, 704 (1977).R. K. Gupta, C. Pirvulescu, A. Săndulescu, and W. Greiner, Z. Phys. A **283**, 217 (1977); Sovt. J. Nucl. Phys. **28**, 160 (1978). R. K. Gupta, Z. Physik. A **281**, 159 (1977).

[25] A. Săndulescu, H. J. Lustig, J. Hahn, and W. Greiner, J. Phys. G: Nucl. Phys. **4**, L279 (1978).H. J. Lustig, J. A. Maruhn, and W. Greiner, J. Phys. G: Nucl. Phys. **6**, L25 (1980).

[26] H. J. Fink, W. Greiner, R. K. Gupta, S. Liran, J.H. Maruhn, W. Scheid, and O. Zohni, in Proceedings of Int. Conf. on Reaction between Complex Nuclei, Nashville, 1974, 21, (Amsterdam: North Holland), pages 2.

[27] R. K. Gupta, IANCAS Bull. (India), **6**, 2 (1990).

[28] V. M. Strutinsky, Nucl. Phys. A **95**, 420 (1967).

[29] G. Audi, A. H. Wapstra and C. Thiboult, Nucl. Phys. A **729**, 337 (2003).

[30] P. Möller, J. R. Nix, W. D. Myers, and W. J. Swiatecki, At. Data Nucl. Data Tables **59**, 185 (1995).

[31] N. J. Davidson, S. S. Hsiao, J. Markram, H. G. Miller, and Y. Tzeng, Nucl. Phys. A **570**, 61c (1994).

[32] P. A. Seeger, Nucl. Phys. **25**, 1 (1961).

[33] S. DeBenedetti, Nuclear Interactions (New York: Wiley) (1964).

[34] W. Myers and W. J. Swiatecki, Nucl. Phys. **81**, 1 (1966).

[35] G. Audi and A. H. Wapstra, Nucl. Phys. A **595**, 4 (1995).

[36] R. K. Gupta, S. Kumar, M. Balasubramaniam, G. Münzenberg, and W. Greiner, J. Phys. G : Nucl. Part. Phys. **28**, 699 (2002).

[37] R. K. Gupta, M. Balasubramaniam, S. Kumar, S. K Patra, G. Münzenberg, and W. Greiner, J. Phys. G : Nucl. Part. Phys. **32**, 565 (2006).

[38] R. K. Gupta, M. Balasubramaniam, R. Kumar, N. Singh, M. Manhas, and W. Greiner, J. Phys. G: Nucl. Part. Phys. C **31**, 631 (2005).

[39] M. Münchow, D. Hahn and W. Scheid, Nucl. Phys. A **388**, 381 (1982).

[40] M. J. Rhoades-Brown, V. E. Oberacker, M. Seiwert and W. Greiner, Z. Phys. A **310**, 287 (1983)

[41] C. Y. Wong, Phys. Rev. Lett. **31**, 766 (1973).

[42] J. Blocki, J. Randrup, W. J. Swiatecki, and C. F. Tsang, Ann. Phys. (NY) **105**, 427 (1977).

[43] Deryagin, Kolloid Z. **69**, 155 (1934).

[44] A. Gray, *Modern Differential Geometry of Curves and Surfaces with Mathematica*, 2nd Edition, CRC Press, Boca Raton, 1997, p.89.

[45] M. Seiwert, W. Greiner, V. Oberacker, and M.J. Rhoades-Brown, Phys. Rev. C **29**, 477 (1984).

[46] R. K. Gupta, N. Singh, and M. Manhas, Phys. Rev. C **70**, 034608 (2004).

[47] N. Malhotra and R. K. Gupta, Phys. Rev. C **31**, 1179 (1985).

[48] S. Kailas (private communication).

[49] H. Kröger and W. Scheid, J. Phys. G **6**, L85 (1980).

[50] Y. J. Shi and Swiatecki, Phys. Rev. C **54**, 300 (1985).

[51] M. Greiner and W. Scheid, J. Phys. G: Nucl. Phys. **12** L229 (1986).

[52] T. Matsuse, C. Beck, R. Nouicer, and D. Mahboub, Phys. Rev. C **55**, 1380 (1997).

[53] S. J. Sanders, D. G. Kovar, B. B. Back, C. Beck, D. J. Henderson, R. V. F. Janssens, T. F. Wang, and B. D. Wilkins, Phys. Rev. C **40**, 2091 (1989).

[54] S. J. Sanders, Phys. Rev. C **44**, 2676 (1991).

[55] R. K. Gupta and W. Greiner, Int. J. Mod. Phys. E, Suppl. **3**, 335 (1994).

[56] J. Gomez del Campo, R.L. Auble, J.R. Beene, M.L. Halbert, H.J. Kim, A. D'Onofrio, and J.L. Charvet, Phys. Rev. C **43**, 2689 (1991); Phys. Rev. Lett. **61**, 290 (1988).

[57] R. J. Charity, M. A. McMahan, G. J. Wozniak, R. J. McDonald, L. G. Moretto, D. G. Sarantites, L. G. Sobotka, G. Guarino, A. Pantaleo, L. Fiore, A. Gobbi and K. D. Hildenbrand, Nucl. Phys. A **483**, 371 (1988).

[58] C. Beck, R. Nouicer, D. Disdier, G. Duchêne, G. de France, R.M. Freeman, F. Haas, A. Hachem, D. Mahboub, V. Rauch, M. Rousseau, S.J. Sanders, and A. Szanto de Toledo, Phys. Rev. C **63**, 014607 (2001).

[59] S.J. Sanders, D.G. Kovar, B.B. Back, C. Beck, B.K. Dichter, D. Henderson, R.V.F. Janssens, J.G. Keller, S. Kaufman, T.-F. Wang, B. Wilkins, and F. Videbaek, Phys. Rev. Lett. **59**, 2856 (1987).

[60] S. Misicu and H. Esbensen, Phys. Rev. Lett. **96**, 112701 (2006); *ibid* Phys. Rev. C **75**, 034606 (2007).

[61] A. M. Stefanini, G. Montagnoli, L. Corradi, S. Courtin, E. Fioretto, A. Goasduff, F. Haas, P. Mason, R. Silvestri, Pushpendra P. Singh, F. Scarlassara and S. Szilner, Phys. Rev. C **81**, 037601 (2010); Phys. Rev. C **82**, 014614 (2010).

[62] C. L. Jiang et. al Phys. Rev. C **71**, 044613 (2005).

[63] R. Vandenbosch and J. R. Huizenga, *Nuclear Fission* (Academic: New York) (1973).

[64] A. J. Sierk, Phys. Rev. C **33**, 2039 (1986).

Chapter 3

Effects of deformations and orientations in the fission of actinide nuclear system ^{254}Fm* formed in ^{11}B+^{243}Am reaction

In this chapter, the decay of actinide nuclear system ^{254}Fm* formed in heavy ion induced reaction is studied using the dynamical cluster decay model [1]- [6]. The compound system ^{254}Fm* is analyzed in reference to experiment [7]. The fission cross sections calculated within DCM find nice comparison with the experiment [7]. The aim of present work [8] is to investigate the role of deformations and orientations in the decay of ^{254}Fm*. In addition to static deformation, the effect of adding temperature dependence in the deformation or(dynamical deformation) is also explored. The mass distribution of various fermium isotopes are analyzed. The fission fragment anisotropies are nicely explored and investigated for the nCN component. Besides, the spontaneous decay behavior is compared nicely with heavy ion induced decay for the first time in this work which shows

asymmetric distribution for spontaneous decay and symmetric for the heavy ion induced decay. In the following, a general introduction in reference to the decay of ^{254}Fm* formed in ^{11}B+^{243}Am reaction is described. Sec. 3.2 presents the calculations and results for the fission cross sections. Finally, a summary of the results is given in Sec. 3.3.

3.1 Introduction

Heavy ion induced reactions are appropriate to explore the dynamics of fusion-fission and related nuclear phenomena. The factors on which the fusion-fission dynamics depend are still not fully understood. Some of them are the large Coulomb repulsion, the entrance channel mass asymmetry, deformations and orientations of projectile (P) and target (T), etc. The reactions having large Coulomb repulsion may fail to form compound nucleus even if the system overcomes the fusion barrier. This is because the distance between the centers of projectile and target at the contact point are larger than that of nascent fragments at the saddle point [9]. However, the same is not true for the light projectile-target combinations, as the difference in the sizes of projectile and target is quite large. According to the pre-equilibrium fission model [10, 11], the mass asymmetry $[\alpha = (A_T - A_P)/(A_T + A_P)]$ is another quantity that plays an important role in deciding the contribution from non-compound nucleus (nCN) fission. In the context of this model if the entrance channel mass asymmetry $\alpha > \alpha_{BG}$, the Businaro Gallone mass asymmetry [12], then nCN is not expected. However, for $\alpha < \alpha_{BG}$ the nCN contribution is not ruled out. In another entrance channel dependent (ECD) K-state model of Vorkapic and Ivanisevic [13], target deformation plays an important role in deciding the contribution from nCN fission. When the collision of projectile occurs with the tip of the deformed target, the compound nucleus formation takes place only if the composite system lies

within the saddle point, otherwise the compound system is elongated enough that it may escape into the exit channel without being captured within the saddle point to form the compound nucleus, resulting in non-compound nucleus fission contribution.

The reaction ^{11}B+^{243}Am has been studied experimentally [7] whose mass asymmetry $\alpha > \alpha_{BG}$ suggests that the nCN contribution should be absent on the basis of pre-equilibrium fission model [10, 11], but the observed fission fragment anisotropies are anomalous *w.r.t.* the statistical model values [7], and hence the presence of nCN contribution is anticipated. According to the authors of this experiment [7], the mass asymmetry alone is not enough to decide the nCN contribution and that, following the entrance channel dependent (ECD) K-state model [13], the target deformation should play an important role in fixing the anomalous behavior of fission fragment anisotropies. In this chapter, this question of the role of deformations and orientations of related fission fragments of ^{254}Fm* nucleus is addressed on the basis of the dynamical cluster-decay model (DCM) [1]- [6]. In the reaction under study, the target nucleus ^{243}Am has a static quadrupole deformation β_2=0.224, taken from [14]. The compound nucleus ^{254}Fm* is also deformed (β_2=0.237). In DCM, the static deformations and orientation degrees of freedom of one or both decay fragments are expected to influence the fusion-fission probability. The dynamically induced deformations are also used since the fusion cross-sections are also expected to differ depending upon whether the deformation is static or dynamically induced [15].

Within the DCM, the decay of actinide nuclear system ^{254}Fm* formed in ^{11}B+^{243}Am reaction over a range of energies (E$_{lab}$=60-72 MeV) [7] is studied by taking the decay fragments either spherical or with quadrupole deformations (β_2) and optimum orientation (θ_i^{opt}) [16], and higher multipole deformations up to hexadecapole (β_2-β_4) with compact orientations (θ_i^c) [17]. The DCM calculated cross sections find nice agreement with experimental data of Ref. [7]. ^{254}Fm* is a fissile nucleus imparting negligible contribution to

evaporation residue. The spontaneous decay of fermium is also looked into for having a comparison of the mass distribution of the decay of ^{254}Fm in hot (temperature $T \neq 0$) as well as cold (T=0) fusion-fission processes. ^{254}Fm being a neutron rich actinide nuclear system with Z=100, also decays spontaneously [18] with an asymmetric mass distribution. The mass distributions of various isotopes ^{250,252,256,258}Fm* are also worked out at E_{lab}=60 MeV within DCM. Also, the fission fragment anisotropies are calculated within standard saddle-point statistical model (SSPM) [19] approach using the DCM based parameters.

It is worth mentioning here that the comparison of β_2 (static) and β_2 (dynamic) is made by making static deformation $\beta_2(0)$ taken from [14], temperature dependent through the relation,

$$\beta_2(T) = \beta_2(0)e^{-T/T_0},$$

where T_0=1.5 MeV. This temperature dependence of β_2 is consistent with experiments at zero temperature [20].

3.2 Calculations

A comparative study of the fragmentation paths of ^{254}Fm* is made, using the spherical, quadrupole (β_2)-alone deformed and higher multipole deformation (β_2-β_4) deformed cases over a wide range of available incident energies [7]. In addition to this, comparison of static-β_2 with dynamic-β_2 deformation is worked out. The DCM based calculations confirm that ^{254}Fm* decays mainly via the fission path and the predicted ER cross sections are negligibly small. Besides this, the issues related to spontaneous fission, isotopic dependence, angular momentum, temperature and fission fragment anisotropies, etc., are also explored.

The scattering potential in Fig. 3.1 at $E_{c.m.}$=57.40 MeV for ℓ_{max} case show that, with

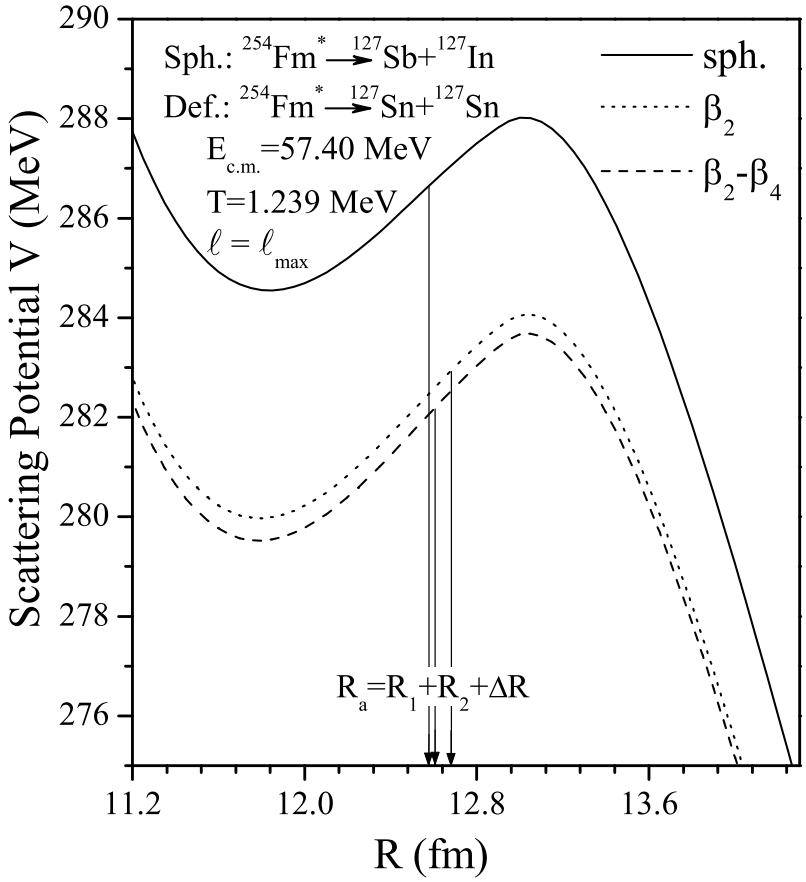

Figure 3.1 Scattering potentials $V(R, \ell)$ as a function of R for fixed ℓ, for the decay ^{254}Fm* $\rightarrow ^{127}$Sb+^{127}In for the spherical and ^{254}Fm* $\rightarrow ^{127}$Sn+^{127}Sn for the deformed (β_2 and β_2-β_4) choices of fragmentations at $E_{c.m.}$=57.40 MeV.

the inclusion of deformation and orientation effects, the barrier height gets modified and hence the penetration point through the barrier. Therefore deformation and orientation degrees of freedom play a significant role in the decay of ^{254}Fm*.

First of all, the behavior of potential energy surfaces is observed in the decay of actinide compound nucleus ^{254}Fm* formed in ^{11}B+^{243}Am reaction, calculated using DCM for the three possible fragmentation paths (i) spherical (ii) β_2 static with optimum orientations (θ_i^{opt}) and (iii) higher multipole static deformations (β_2-β_4) with compact orientation (θ_i^{c})). Figs. 3.2(a) and (b) illustrate the fragmentation potentials as a function of fragment mass A_2 for ℓ=0 and $\ell = \ell_{max}$ values for the above said three cases. The optimum orientations θ_i^{opt} are uniquely fixed on the basis of the quadrupole deformation alone of nuclei [16] and

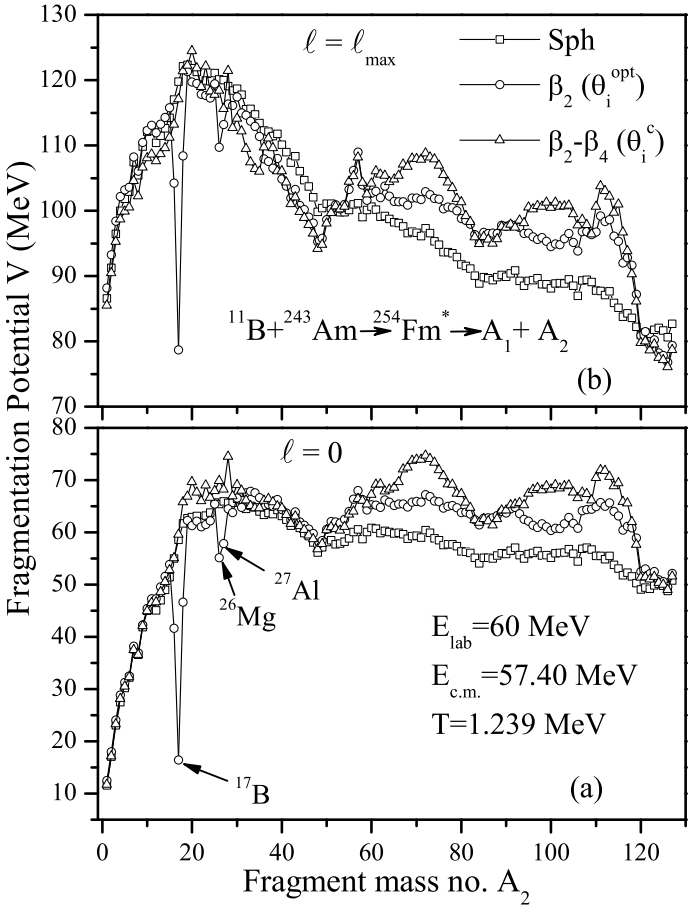

Figure 3.2 Fragmentation potential as a function of light mass fragment A_2 for the decay of ^{254}Fm* formed in ^{11}B+^{243}Am reaction channel for spherical as well as deformed considerations at (a) ℓ=0 and (b) $\ell = \ell_{max}$.

compact orientations θ_i^c for higher-multipole deformations (β_2-β_4) are calculated as per prescription in [17], using hot configurations in both cases. Figs. 3.2(a) and (b) show that the potential surfaces are nearly smooth for the spherical choice of fragmentations at ℓ=0 and $\ell = \ell_{max}$, which, however, show enough structure with the inclusion of deformations, and certain minima (^{17}B,^{26}Mg,^{27}Al) are observed to be rather deep for the β_2 (static) deformations with optimum orientations. However, these deeper minima do not make any significant contribution since the penetration probability of these fragments is negligibly small. The emergence of these unexpected minimas may be due to the inappropriate values of optimized β_2-deformations used in the calculations and occur mainly because

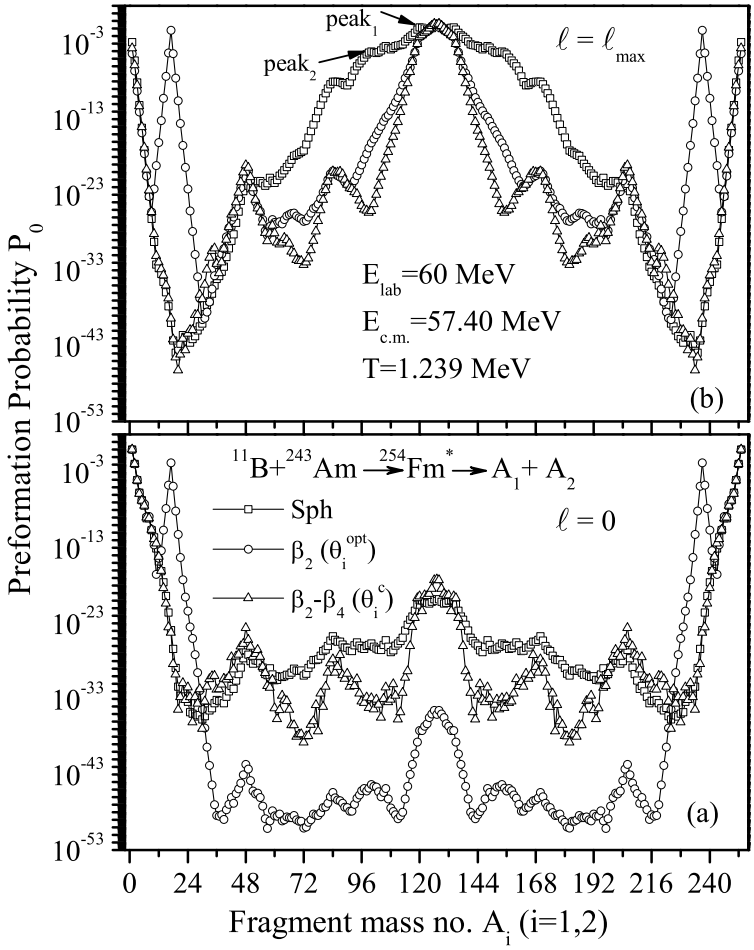

Figure 3.3 Same as for Fig.3.2, but for the preformation probability P_0 as a function of fragment mass A_i (i=1,2).

of the proximity (V_P) part of the fragmentation potential. It is further noticed that at ℓ=0, the light fragments (representing ER) are more dominant whereas with the increase in ℓ-value the fission fragments start appearing such that at ℓ=ℓ_{max} value, the symmetric fission dominates the ER channel. This aspect is further explored in Fig. 3.3 showing the preformation probability P_0, obtained by solving the stationary Schrödinger equation in η-coordinate.

Fig. 3.3 clearly depicts that the decay of ^{254}Fm* follows a symmetric pattern, independent of the deformation effects, though a shoulder structure is seen in the spherical considerations, a signature of asymmetric fission fragments, which vanishes with the ad-

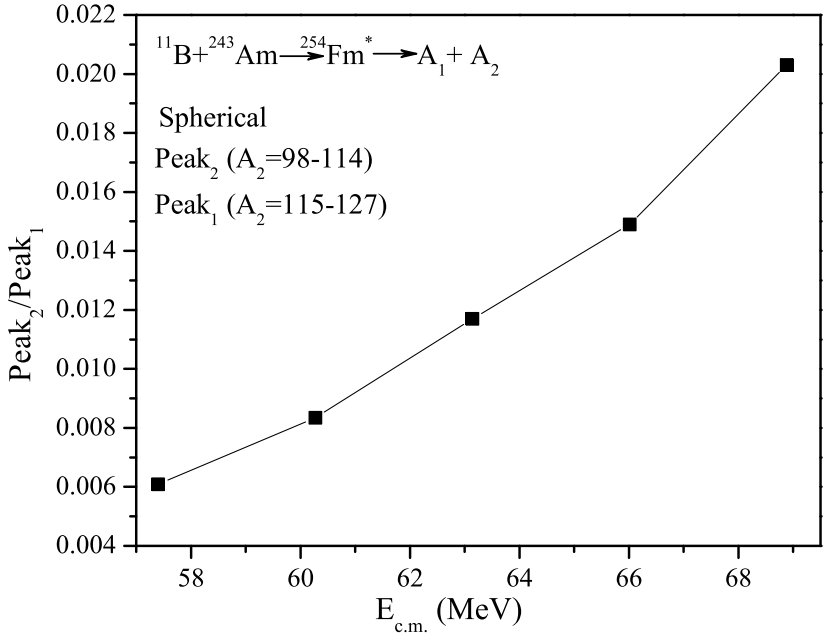

Figure 3.4 The ratio of the asymmetric to symmetric fission yields as a function of $E_{c.m.}$ for the spherical choice of nuclei in the fragmentation process of the decay of $^{254}Fm^{*}$.

dition of deformation effects. One may note, however, that the contribution of fragments forming the shoulder is very small. This is depicted in Fig. 3.4, which shows the asymmetric to symmetric peak ratio ($\frac{Peak_2}{Peak_1}$) as a function of $E_{c.m.}$. The $Peak_2$ represents the fragments with mass number A_2=98-114 and $Peak_1$ to masses A_2=115-127. It is clear from Fig. 3.4 that contribution of $Peak_2$ is very small. It is approximately 0.6% at the lowest energy and increases to a maximum of 2% at the highest energy. This implies that the contribution of the asymmetric fragments even for spherical choice of fragmentation is negligibly small. One may conclude here that the symmetric fragmentation is preferred in the decay of $^{254}Fm^{*}$, independent of spherical, alone β_2-deformation or (β_2-β_4) deformations.

The fission cross sections are calculated, in reference to experimental data of [7], within the DCM by fitting the only parameter of the model, the neck-length parameter ΔR which itself varies as a function of center of mass (c.m.) energy. It is observed

Table 3.1 DCM calculated fission cross-sections ($\sigma_{fission}$), compared with experimental data [7], and the predicted ER cross-sections (σ_{ER}), for the decay of ^{254}Fm* formed in ^{11}B+^{243}Am reaction, considering spherical as well as deformed choice of fragments.

$E_{c.m.}$	T	$\triangle$R$_{fission}$			$\sigma_{fission}$(DCM)			$\sigma_{fission}$	σ_{ER}(DCM) at $\triangle$R$_{fission}$		
		sph	β_2	β_2-β_4	sph	β_2	β_2-β_4	(Expt.)	sph	β_2	β_2-β_4
(MeV)	(MeV)	(fm)	(fm)	(fm)	(mb)	(mb)	(mb)	(mb)	(mb)	(mb)	(mb)
									($\times10^{-5}$)	($\times10^{-5}$)	($\times10^{-5}$)
57.40	1.239	0.9	1.0025	0.929	175.4	175.6	173.4	176.86	0.0337	0.0186	0.0556
60.27	1.28	1.0	1.038	0.986	354	356	352	357.96	0.512	0.247	0.313
63.142	1.32	1.042	1.0575	1.017	452	450	450	453.41	1.59	0.922	0.796
66.012	1.359	1.0589	1.076	1.0618	610	608	606	609.27	2.69	2.25	2.72
68.882	1.396	1.074	1.088	1.0775	710	708	710	709.87	4.42	3.96	4.78

that for each center of mass energy, the fits can be achieved by the spherical as well as deformed considerations within the single neck-length parameter ΔR. Fig. 3.5 and Table 3.1 show that the DCM calculated fission cross-sections are in excellent agreement with the experimental data for all the three choices of fragmentation. It is further clear from Table 3.1 that the decay is a pure fission decay, with the almost negligible evaporation residue (ER) cross sections calculated at the fission fitted ΔR values. Fig. 3.6 shows the variation of ΔR with E$_{c.m.}$ for the three choices of shapes of fragments. One may notice that ΔR increases with increase in energy, and that it has higher magnitude for the β_2 deformations, compared to both spherical and including β_4 deformations. Another quantity of interest, related to ΔR, is the variation of barrier lowering parameter ΔV_B as a function of $E_{c.m.}$, an important property at near and sub-barrier energies [21]. Fig. 3.7 shows that ΔV_B is the largest for the case of β_2-β_4 at near barrier energies. On the other hand, at above barrier energies, the barrier modification is small and comparable for the three cases.

In order to see the relative behavior of static and dynamic deformations Fig. 3.8 is

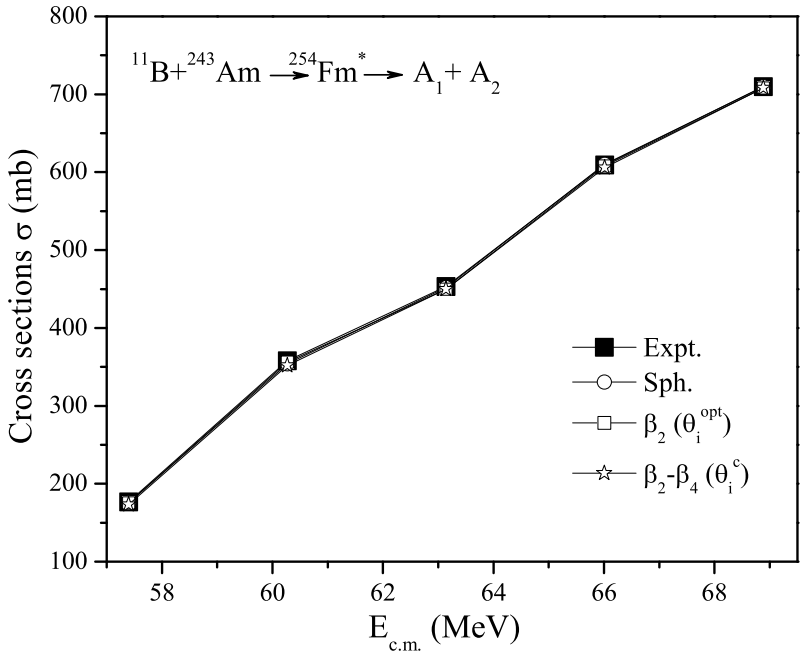

Figure 3.5 The DCM calculated fission cross-sections, compared with the experimental data [7], for the decay of ^{254}Fm* formed in ^{11}B+^{243}Am reaction as a function of $E_{c.m.}$ for spherical, alone β_2 deformation and higher multipole deformations upto hexadecapole (β_2-β_4) choices of the fragmentation process.

plotted which shows the role of dynamic-β_2, compared with static-β_2 deformations with optimum orientations, for the preformation probability P_0 as a function of fragment mass A_i (i=1,2) for the decay of ^{254}Fm*. It can be noticed that the distribution is symmetric for both the choices of β_2 (static and dynamic), although a small shoulder is formed for the dynamic-β_2 choice of fragmentation, similar to what was seen in the case of spherical choice of fragmentation for static-β_2 (refer to Fig. 3.3). It may be noted that the angular momentum ℓ_{max} involved here in the reaction dynamics is having higher values. This is because of the use of sticking moment of inertia (I_S) in the centrifugal potential (V_ℓ) term. It is relevant to mention here that non sticking (I_{NS}) approximation gives larger centrifugal potential as compared to sticking(I_S) limit for the moment of inertia, at the same R [1, 22]. Therefore, one would expect larger ℓ-values for the use of I_S approach as compared to that for I_{NS}.

Since we are using proximity interaction in our model, the use of I_S is more appropriate

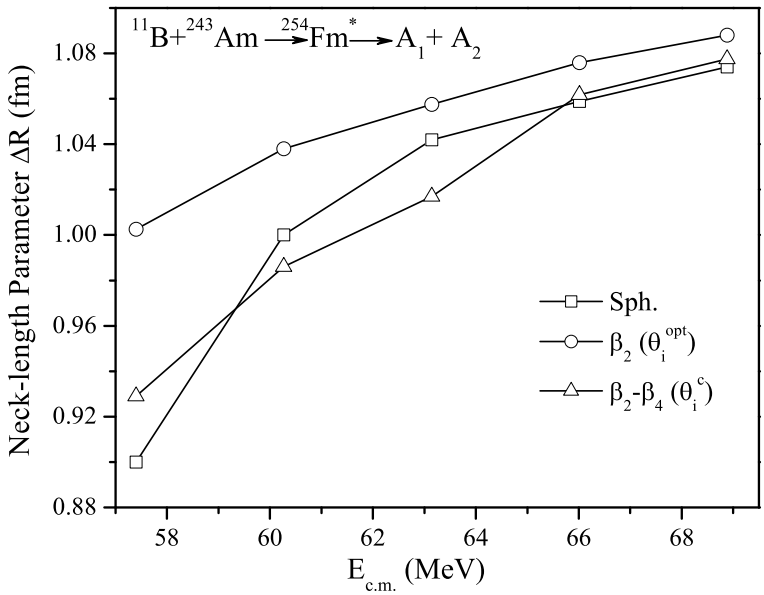

Figure 3.6 The fitted neck-length parameter $\triangle$R for fission decay of ^{254}Fm* formed in ^{11}B+^{243}Am reaction, as function of E$_{c.m.}$, for spherical as well as deformed considerations.

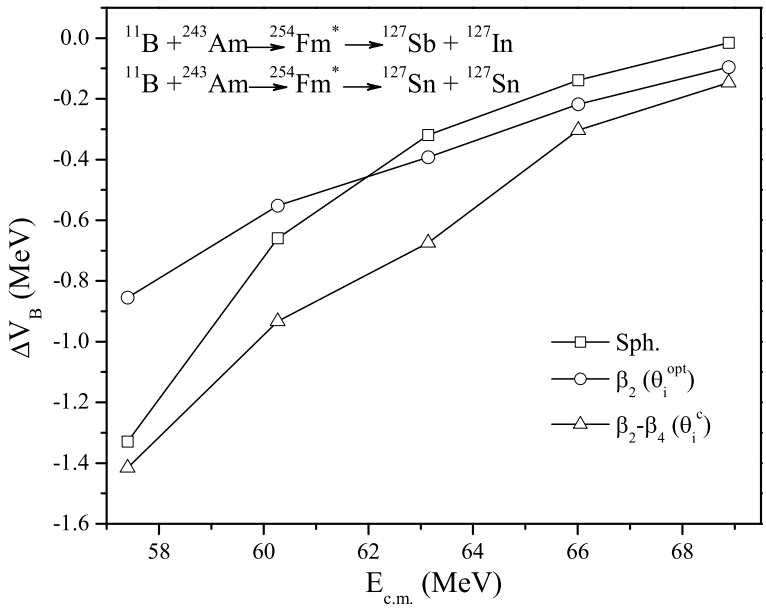

Figure 3.7 The barrier lowering parameter $\triangle V_B$ as a function of $E_{c.m.}$ for the decay ^{254}Fm* $\rightarrow ^{127}$Sb+^{127}In for spherical fragments, and ^{254}Fm* $\rightarrow ^{127}$Sn+^{127}Sn for deformed (β_2 and β_2-β_4) fragments.

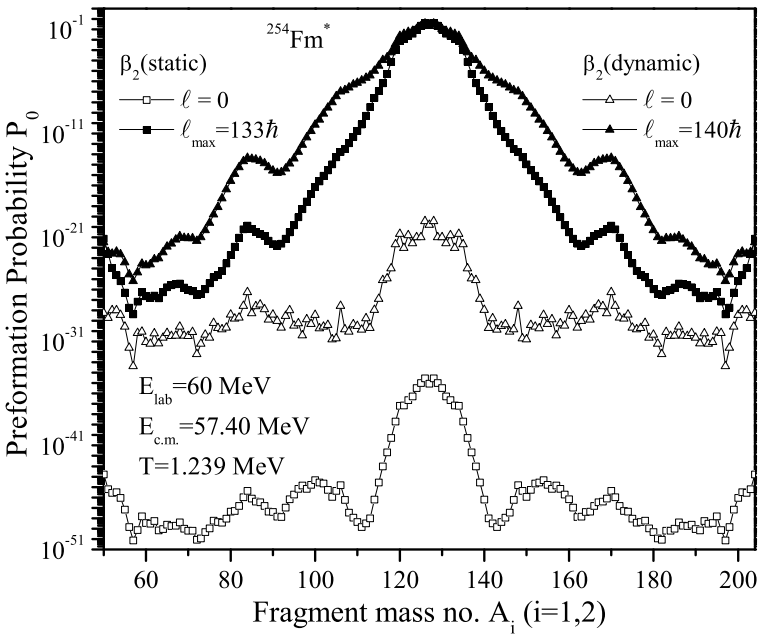

Figure 3.8 Preformation probability P_0 as a function of fragment mass number A_i (i=1,2) for the decay of ^{254}Fm* formed in ^{11}B+^{243}Am reaction channel at E_{lab}=60 MeV for β_2-dynamic compared with β_2-static deformations of fragments.

as structure effects due to proximity forces are more visible for the use of sticking choice of moment of inertia. It may be noted that the use of I_{NS} approach in centrifugal potential weakens the (attractive) nuclear proximity interaction and hence $V_\ell(I_S)$ with relatively lower magnitude is preferred.

The fission cross-sections with dynamic-β_2 deformations are also calculated, by fitting again the neck-length parameter ΔR. The two ΔR's are compared in Fig. 3.9(a), showing that the static ΔR values are higher than for dynamic β_2 choice of fragmentations. A similar comparison for ΔV_B values for β_2-static and β_2-dynamic is shown in Fig. 3.9(b) which clearly depicts that the barrier lowering at near barrier energies is more for the β_2 dynamic than for β_2 static choice of fragmentation. At higher energies, however, the difference becomes minimal and $\triangle V_B$ goes to zero in both the cases.

It is of further interest to look for the fragmentation behavior of the various isotopes of fermium. Fig. 3.10 shows the calculated preformation probability P_0 for various isotopes

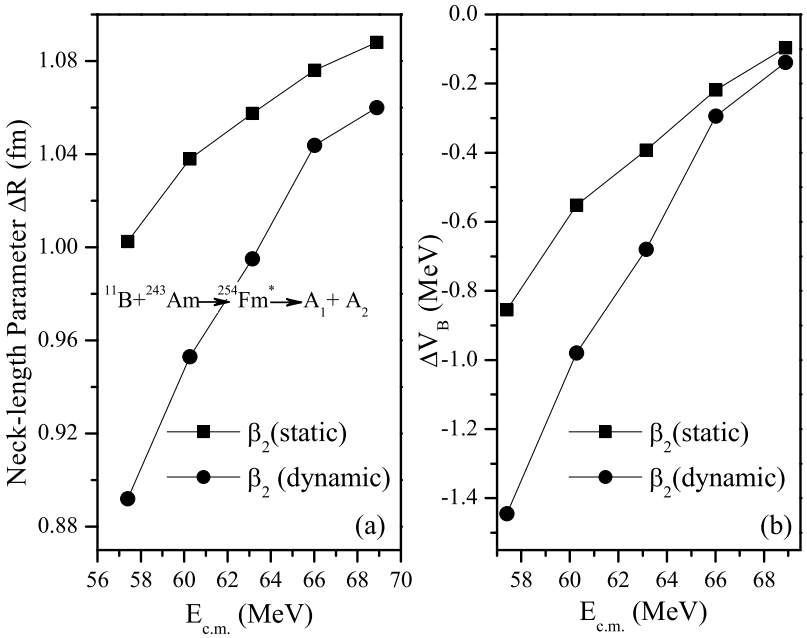

Figure 3.9 (a) The fitted neck-length parameter △R and (b) the barrier lowering parameter $\triangle V_B$ for fission, as a function of $E_{c.m.}$, for the β_2-static as well as β_2-dynamic deformations.

of fermium ($^{250-258}$Fm*) as a function of fragment mass number A$_i$ (i=1,2). The calculations are made at E_{lab}=60 MeV by taking the same value for the neck-length parameter ΔR and ℓ_{max}-value as for ^{254}Fm* at the said energy. Only the case of β_2-deformed fragmentation is considered. One may notice in Fig. 3.10 that the decay of fermium isotopes still follow the symmetric distribution when 2 or 4 neutrons are added to or subtracted from ^{254}Fm*. Although a small hump is seen for the neutron deficient ^{250}Fm*, similar to the one observed in the case of spherical fragmentation of ^{254}Fm*, but the contribution of this asymmetric hump is again negligibly small.

It can be seen from Figs. 3.3 and 3.10 that the mass distribution is symmetric for the decay of excited ^{254}Fm* and its isotopes ^{252,256,258}Fm* formed in heavy-ion reactions. This result may, however, be not valid for the spontaneous (T=0) decay of ^{254}Fm. Fig. 3.11 shows the preformation probability P_0 as a function of fragment mass for the spontaneous decay of ^{254}Fm for cold elongated configuration with β_2-deformed, optimum orientation

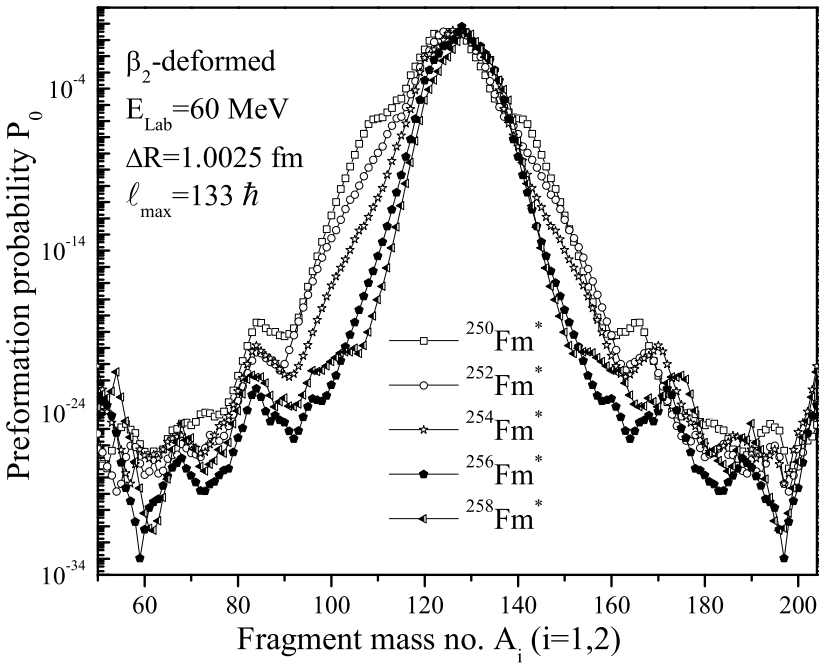

Figure 3.10 Preformation probability P_0 as a function of fragment mass number A_i (i=1,2) for $^{250-258}$Fm* isotopes at E_{lab}=60 MeV.

approach. It is clear from Fig. 3.11 that the mass distribution is asymmetric for the spontaneous decay, in contrast to it's being symmetric for the heavy-ion induced decay in Figs. 3.3 and 3.10. One can also observe from Fig. 3.11 that the angular momentum (ℓ) does not affect much the structure of P_0.

Finally, the fission fragment anisotropies are calculated within the SSPM approach using DCM calculated ℓ_{max} values for the non-sticking limit for the moment-of-inertia (I_{NS}) using β_2-deformed consideration. It is relevant to remind here that the non sticking moment-of-inertia limit (I_{NS}) is preferred for fission fragment anisotropy calculations and the sticking limit (I_S) for cross sections [22]. In Fig. 3.12, the DCM calculated fission fragment anisotropies are shown at ΔR-values same as that for fission, which means using same neck length as the one used for cross section fitting with the sticking moment-of-inertia limit I_S. Statistical model calculations, with and without ($\nu_{pre} \neq 0$ or $=0$) correction for prefission neutrons, are also given for comparisons. One can notice that

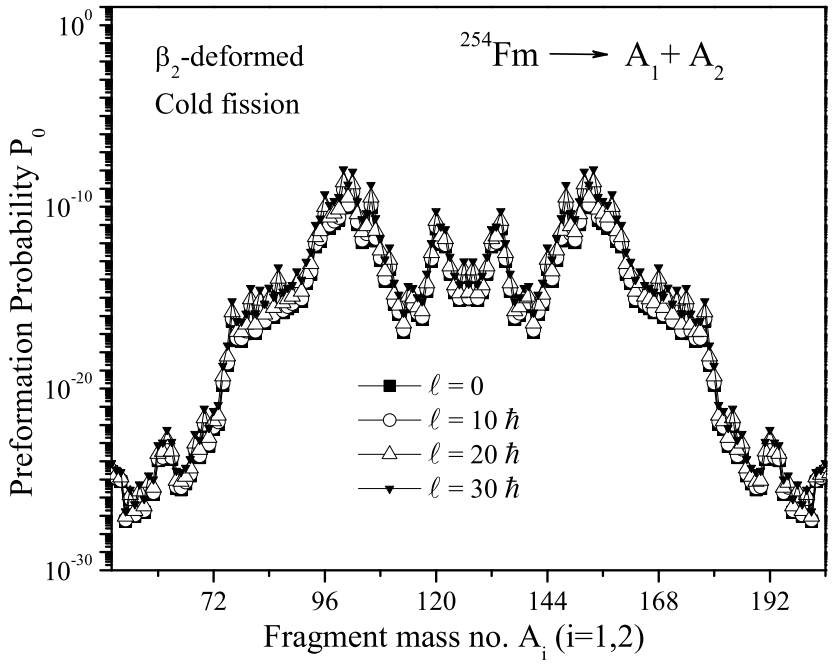

Figure 3.11 Preformation probability P_0 as a function of fragment mass number A_i (i=1,2) for the spontaneous decay (cold fission) of ^{254}Fm using β_2-deformed cold (T=0) elongated configuration at different ℓ values.

the DCM calculated fission fragment anisotropies for $\Delta R_{fission}$ are comparable with the statistical model calculations without correcting for prefission neutrons (ν_{pre}=0), but not with the experimental data. Knowing that ΔR for I_{NS} is larger than for I_S [22], the calculations are also made by increasing the $\Delta R_{fission}$ by 0.3 fm. As expected, for this choice of ΔR, calculated fission fragment anisotropies start approaching the lower limit of experimental values. Apparently, best fit for $\Delta R_{fission}$-plus- a constant, or ΔR for I_{NS} could be obtained, but is not attempted here. Lastly, an attempt is made to see the contribution of competing non-compound nucleus (nCN) quasi fission (qf) channel in the decay of ^{254}Fm*. The calculations are done by taking P_0=1 for the incident channel ^{11}B+^{243}Am since the incoming fragments do not loose their identity in qf process. The DCM based qf contribution is maximum upto 3% of the fission cross-section.

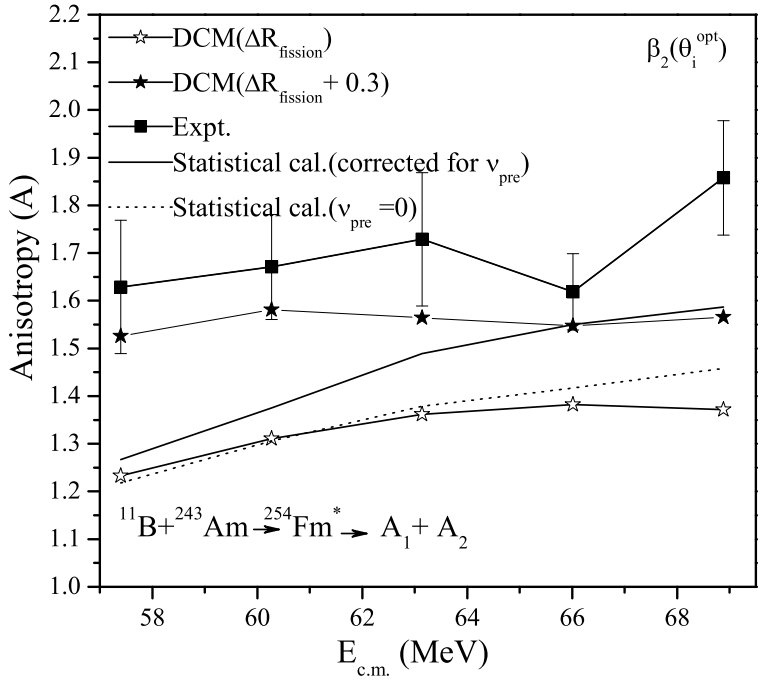

Figure 3.12 The DCM calculated fission fragment anisotropies for the case of β_2-deformation, compared with the experimental data [7] and statistical model calculations (with and without correcting for prefission neutrons).

3.3 Summary

In this chapter, the decay of actinide nuclear system $^{254}Fm^{*}$ formed in $^{11}B+^{243}Am$ reaction is studied. The fusion-fission excitation functions of $^{254}Fm^{*}$ for $^{11}B+^{243}Am$ reaction have been calculated using the spherical, β_2-alone, and higher multipole (β_2-β_4) deformations with proper compact orientations of fragments. The nice comparison between the DCM calculated and experimental fission cross-sections at all energies suggests that the contribution of competing non-compound nucleus quasi-fission (qf) component is quite small, amounting to maximum upto 3% of fission cross section. The comparison of β_2-static and β_2-dynamic deformation is also worked out for the fragmentation path of $^{254}Fm^{*}$ nucleus. In the case of spontaneous decay of ^{254}Fm, an asymmetric fission is preferred whereas in the heavy-ion induced decay of $^{254}Fm^{*}$ the mass distribution is clearly symmetric, independent of the deformation effects. The various isotopes of compound nucleus fermium

($^{250-258}$Fm*) also show symmetric behavior in their fragmentation path. The fission fragment anisotropies, calculated at $\Delta R_{fission}$ are in agreement with the statistical model calculations, but for ΔR increased to bring it close to I_{NS} value, the anisotropies start approaching the experimental data. The neck-length parameter ΔR is found to be relatively larger for β_2-deformed case, and comparable for spherical and β_2-β_4 deformations. Although the fragmentation behavior is influenced due to the inclusion of deformation effects, but the overall fission path remains symmetric for the excited ^{254}Fm* and its neighboring isotopes.

Bibliography

[1] B. B. Singh, M. K. Sharma and R. K. Gupta, Phys. Rev. C **77**, 054613 (2008).

[2] Niyti, R. K. Gupta and W. Greiner, J. Phys. G: Nucl. Part. Phys. **37**, 115103 (2010); R. K. Gupta, Niyti, M. Manhas and W. Greiner, J. Phys. G: Nucl. Part. Phys. **36**, 115105 (2009).

[3] S. Kanwar, M. K. Sharma, B. B. Singh, R. K. Gupta and W. Greiner, Int. J. Mod. Phys E **18**, 1453 (2009).

[4] M. K. Sharma, S. Kanwar, G. Sawhney, R. K. Gupta and W. Greiner, J. Phys. G: Nucl. Part. Phys. **38**, 055104 (2011); D. Jain, R. Kumar, M. K. Sharma and R. K. Gupta, Phys. Rev. C **85**, 024615 (2012).

[5] M. Kaur, R. Kumar and M. K. Sharma, Phys. Rev. C **85**, 014609 (2012).

[6] K. Sandhu, M. K. Sharma and R. K. Gupta, Phys. Rev. C **85**, 024604 (2012).

[7] R. Tripathi, K. Sudarshan, S. Sodaye, S. K. Sharma, and A. V. R. Reddy, Phys. Rev. C **75**, 024609 (2007).

[8] M. Kaur, M. K. Sharma and Raj K. Gupta, Phys. Rev. C **86**, 064610 (2012).

[9] K. Nishio, H. Ikezoe, S. Mitsuoka, K. Satou, and S. C. Jeong, Phys. Rev. C **63**, 044610 (2001).

[10] V. S. Ramamurthy and S. S. Kapoor, Phys. Rev.Lett. **54**, 178 (1985).

[11] V. S. Ramamurthy, S. S. Kapoor, R. K. Choudhury, A. Saxena, D. M. Nadkarni, A. K. Mohanty, B. K. Nayak, S. V. Sastry, S. Kailas, A. Chatterjee, P. Singh and A. Navin, Phys. Rev. Lett. **65**, 25 (1990).

[12] K. U. L. Businaro and S. Gallone, Nuovo Cimento **5**, 315 (1957); K. T. R. Davies and A. J. Sierk, Phys. Rev. C **31**, 915 (1985).

[13] D. Vorkapic and B. Ivanisevic, Phys. Rev. C **52**, 1980 (1995).

[14] P. Moller, J. R. Nix, W. D. Myers, W. J. Swiatecki, At. Data Nucl. Data Tables, **59**, 185 (1995).

[15] R. G. Stokstad, Y. Eisen, S. Kaplanis, D. Pelte, U. Smilansky, and I. Tserruya, Phys. Rev. Lett. **41**, 465 (1978).

[16] R. K. Gupta, M. Balasubramaniam, R. Kumar, N. Singh, M. Manhas and W. Greiner, J. Phys.G : Nucl. Part. Phys. **31**, 631 (2005).

[17] R. K. Gupta, M. Manhas and W. Greiner, Phys. Rev. C **73**, 054307 (2006).

[18] J. E. Gindler, K. F. Flynn, L. E. Glendenin, and R. K. Sjoblom, Phys. Rev. C **16**, 1483 (1977).

[19] R. Vandenbosch and J. R. Huizenga Nuclear Fission (New York: Academic) (1973).

[20] T. Cooper, W. Bertozzi, J. Heisenberg, S. Kowalski, W. Turchinetz, C. Williamson, L. Cardman, S. Fivozinsky, J. Lightbody, Jr., and S. Penner, Phys. Rev. C **13**, 1083 (1976).

[21] S. K. Arun, R. Kumar and R. K. Gupta, J. Phys. G: Nucl. Part. Phys. **36**, 085105 (2009).

[22] M. K. Sharma, G. Sawhney, R. K. Gupta and W. Greiner, J. Phys. G: Nucl. Part. Phys. **38**, 105101 (2011); M. K. Sharma, G. Sawhney, S. Kanwar and R. K. Gupta, Mod. Phys. Lett. A **25**, 2022 (2010).

Chapter 4

Analysis of fragment distribution and associated effects in ^{12,13}C + ^{208,207}Pb reactions

In the previous chapter, the decay of ^{254}Fm* formed in ^{11}B+^{243}Am reaction was studied using DCM. The effect of adding higher multipole deformations and related orientations were investigated. The mass distribution for spontaneous and heavy ion induced decay were analyzed. Beside this, the effect of static and dynamic deformation, role of angular momentum and presence of nCN component etc. was discussed. Here in present chapter, the dynamics of ^{220}Ra* nuclear system formed in ^{12,13}C + ^{208,207}Pb reaction channels is analyzed in reference to complete fusion (CF) and incomplete fusion (ICF) processes over a wide range of energies using DCM [1]- [11]. Various possible decay mechanisms are worked out in reference to [12]. The entrance channel and angular momentum effects are nicely explored. The fragment mass distribution is analyzed by considering the weakly bound projectile ^{13}C incident on different targets.

4.1 Introduction

One of the most interesting feature of heavy ion reactions is its theoretical description. One can understand the reaction mechanism by carrying theoretical calculations, whose agreement with experimental data can lead to various new developments in the related area. The heavy ion induced reactions are generally described in terms of Complete fusion (CF) process where the projectile fuses completely with the target to form a composite system (known as compound nucleus (CN)) which equilibrates in all degrees of freedom. The nuclear reaction is a two step process, in the first step the formation of compound nucleus takes place and the subsequent decay occurs in the second step. It is relevant to mention here that the decay and formation process are generally treated separately, by employing relevant methodologies. It is so because the compound nucleus looses the memory of its formation and it allows an independent description of the decay process where it may de excite in a number of ways such as neutron(n)-decay, evaporation residue (ER), fission etc.. In ER light particles with mass $A_2 \leq 4$ are formed and fission is a process in which the composite system decays into two comparable fragments and it involves the rearrangement of nucleons inside the nucleus before the division. Besides this, one may also observe subsequent decay such as neutron evaporation followed by α-decay, popularly known as αxn process.

Prior to interaction with target, a projectile may also breakup into two fragments where a part of the projectile fuses with the target to form a reduced composite mass which contributes toward ICF cross sections, and the residual part acts as a mere spectator. The time evolution of the so formed composite system via CF or ICF process can be understood by the systematic study of the related reaction dynamics. There are a number of parameters which govern the dynamics of a nuclear reaction e.g. driving angular momentum, mass asymmetry, projectile type, binding energy, deformation of interacting

partners, related orientations and excitation energy involved. Generally the lower angular momentum states are supposed to contribute towards CF process and higher angular momentum states of the projectile are responsible for ICF component. Mass asymmetry (η) is another quantity which plays an important role in the reaction dynamics. It has been reported that ICF contribution increases with entrance channel mass asymmetry [13] i.e the system which is more asymmetric contributes more towards ICF. The type of projectile is another parameter which decides the ICF process and the study involving weakly bound stable projectile is of considerable interest over the last decade [14,15]. The reaction where the colliding nuclei have low binding energy, the breakup process becomes important. There are a number of stable as well as weakly bound nuclei involving different isotopes of Li, Be, B and C which have been used in a variety of nuclear reactions to address and understand the issues related to breakup process.

In the present work, the decay of ^{220}Ra* formed in ^{12}C+^{208}Pb and ^{13}C+^{207}Pb reaction channels is analyzed using the Dynamical cluster decay model (DCM) at comparable compound nucleus energies (E_{CN}) in reference to the experimental data of [12]. It is well known fact that the reactions involving weakly bound light nuclei show suppression of complete fusion cross sections at above barrier energies. This is associated with the low binding energy of the projectile which results in breakup of projectile in the vicinity of target nucleus and lead to ICF. In order to understand this phenomena, the experiment [12] was performed considering ^{12,13}C as the projectiles incident on ^{208,207}Pb forming the same compound nucleus ^{220}Ra* over a wide range of energies. The complete fusion cross sections as well as incomplete fusion cross sections following breakup were measured in [12]. In the present work, the dynamics of ^{12,13}C induced reactions is analyzed in the framework of DCM. This method was applied earlier [9], to investigate the decay pattern of ^{219,220}Ra* formed in ^{10,11}B based reactions. Here the decay of ^{220}Ra* formed in different

reaction channels involving ^{12}C and ^{13}C as projectile is studied. The cross-sections of possible decay processes of ^{220}Ra* are estimated using DCM by duely incorporating the β_2-deformations with optimum (θ_i^{opt}) orientations. The entrance channel and angular momentum effects on the basis of fragment mass distribution profile are addressed. Besides this, different decay mechanism of ^{220}Ra* involving ER, n-decay, fission, αxn decay channels are explored. The fragmentation behavior and preformation of decaying fragments is analyzed by increasing mass of the target nucleus leading to different composite systems in the ^{13}C+^{159}Tb, ^{13}C+^{181}Ta and ^{13}C+^{207}Pb reactions. Finally the ICF component is evaluated for both the channels ^{12,13}C+ ^{208,207}Pb.

The organization of the chapter is as follows: The results of DCM based calculations for the decay of ^{220}Ra are discussed in Sec 4.2 and the same are summarized in Sec. 4.3.

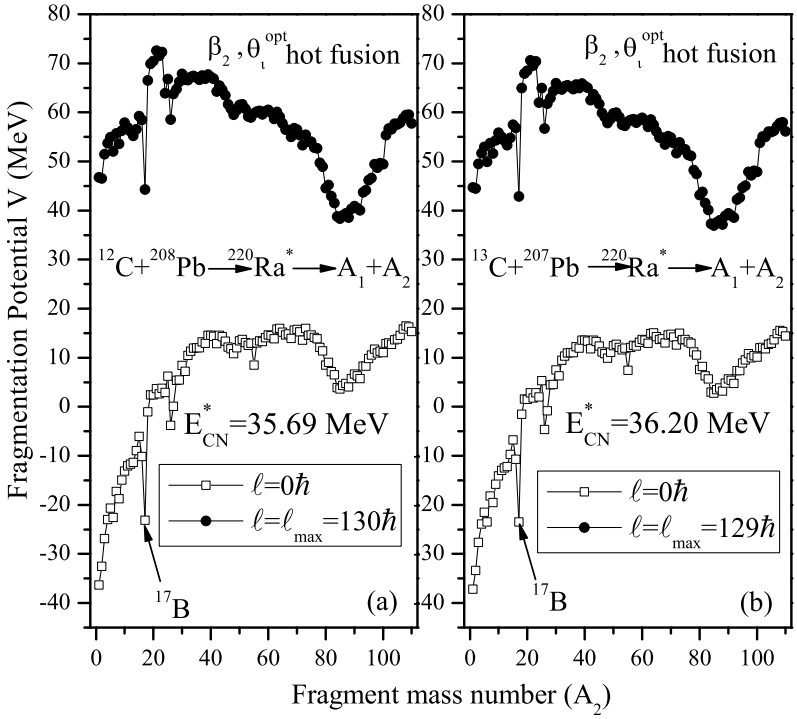

Figure 4.1 Fragmentation potential as a function of light mass fragment A_2 for the decay of ^{220}Ra* considering β_2 deformations at extreme ℓ values formed in (a) ^{12}C+^{208}Pb and (b) ^{13}C+^{207}Pb reaction channels.

Table 4.1 DCM calculated decay cross-sections for fission ($\sigma_{fission}$), ER (σ_{ER}) and complete fusion (σ_{CF}) for the decay of ^{220}Ra* formed in ^{12}C+^{208}Pb and ^{13}C+^{207}Pb reaction channel considering β_2 deformed fragmentation path, compared with the experimental data.

E_{lab}	$E_{c.m.}$	E_{CN}	T	ER			fission			σ_{CF}		
				$\triangle$R	ℓ_{max}	σ_{DCM}	$\triangle$R	ℓ_{max}	σ_{DCM}	σ_{Expt}	DCM($_{ER+fission}$)	Expt
(MeV)	(MeV)	(MeV)	(MeV)	(fm)	($\hbar$)	(mb)	(fm)	($\hbar$)	(mb)	(mb)	(mb)	(mb)
				^{12}C+^{208}Pb$\rightarrow^{220}$Ra$^*\rightarrow$A$_1$+A$_2$								
71.50	67.56	35.69	1.229	2.039	119	438.24	1.042	130	160.4	160±3	598.64	599.5±17
76.00	71.81	39.95	1.299	2.062	119	489.73	1.112	130	292	292±3	781.73	783±15
82.00	77.49	45.62	1.387	2.07	120	503.90	1.179	130	488	491±5	991.9	994±13
88.00	83.16	51.29	1.469	2.061	122	465.40	1.2023	131	704	707±7	1172.4	1172±13
94.00	88.83	56.96	1.547	2.033	123	387.58	1.374	131	910	910±9	1297.58	1299±15
				^{13}C+^{207}Pb$\rightarrow^{220}$Ra$^*\rightarrow$A$_1$+A$_2$								
69.27	65.18	36.20	1.237	2.029	120	418.8	1.047	129	159.8	160.54±2.33	578.6	581±7
73.81	69.45	40.47	1.307	2.059	120	500.7	1.11	130	292	290±3	792.7	790±8
79.82	75.10	46.12	1.394	2.074	120	534.73	1.171	131	492	496.41±5	1026.73	1032±7
85.85	80.78	51.80	1.476	2.069	122	506.6	1.202	131	710	716.04±6	1216.6	1225±16
91.87	86.44	57.46	1.553	2.055	123	464.38	1.37	131	916	918±9	1380.38	1384±14

4.2 Calculations

DCM is used to study the dynamics of the reaction ^{12}C+^{208}Pb and ^{13}C+^{207}Pb forming the compound nucleus ^{220}Ra* at comparable E_{CN} energies. Firstly in Section 4.2.1, the entrance channel independence is worked out on the basis of fragment mass distribution in context of decay of ^{220}Ra*. Then the fragmentation profile of different possible decay mechanism such as ER, n-decay, αxn channel, fission etc. is explored. In Section 4.2.2, an attempt is made to investigate the effect of target mass on the fragmentation path of compound systems formed in ^{13}C induced channels. Finally, the ICF contribution towards

Table 4.2 DCM calculated cross-sections for the neutron decay of ^{220}Ra* formed in ^{12}C+^{208}Pb and ^{13}C+^{207}Pb reaction channel compared with experimental data. It may be noted that neutron evaporation residues are obtained by summing xn (x=1-4) cross sections.

E_{lab}	$E_{c.m.}$	E_{CN}	T	$\triangle$R	ℓ_{max}	$\Sigma_{xn}\ \sigma_{Ra}$	
						DCM(x=1-4)	Expt.
(MeV)	(MeV)	(MeV)	(MeV)	(fm)	($\hbar$)	(mb)	(mb)
^{12}C+^{208}Pb$\rightarrow^{220}$Ra*$\rightarrow$A$_1$+A$_2$							
71.50	67.56	35.69	1.229	2.039	119	438	438±17
76.00	71.81	39.95	1.299	2.061	119	486	486±15
82.00	77.49	45.62	1.387	2.068	120	494.48	495±12
88.00	83.16	51.29	1.469	2.059	121	452.86	453±11
94.00	88.83	56.96	1.547	2.032	123	374	376±12
^{13}C+^{207}Pb$\rightarrow^{220}$Ra*$\rightarrow$A$_1$+A$_2$							
69.27	65.18	36.20	1.237	2.029	120	418	420±16
73.81	69.45	40.47	1.307	2.059	120	499.62	500±13
79.82	75.10	46.12	1.394	2.075	120	534.48	535±18
85.85	80.78	51.80	1.4764	2.071	121	505	507.4±25
91.87	86.44	57.46	1.553	2.059	123	463	464.49±18

total fusion cross section is worked out for both the reactions in Section 4.2.3.

4.2.1 Entrance channel effect and competing decay mechanism in CF process

First of all, the fragmentation path of ^{220}Ra* compound system formed in ^{12,13}C induced channels is investigated. Fig. 4.1 illustrates the fragmentation potential as a function of fragment mass number for the decay of ^{220}Ra* formed in ^{12}C+^{208}Pb and ^{13}C+^{207}Pb reactions at comparable compound nucleus energy E^*_{CN}, by using β_2-deformations with optimum orientation (θ_i^{opt}) at extreme ℓ-values. The deformation parameter β_{2i} are taken from [16] and optimum orientation are used as in [11]. The results evident from Fig. 4.1 are: (i) Both the channels exhibit asymmetric fragmentation path and the ℓ=0 state

Table 4.3 DCM calculated cross-sections for charged particle (αxn) evaporation residues formed via the complete fusion in the ^{13}C+^{207}Pb reaction compared with the experiment.

E_{lab}	$E_{c.m.}$	E_{CN}	$\triangle$R	$\sigma_{\alpha 1n}(^{215}$Rn)	$\sigma_{\alpha 2n}(^{214}$Rn)	$\sigma_{\alpha 3n}(^{213}$Rn)	$\sigma_{\alpha 4n}(^{212}$Rn)	$\Sigma\sigma$Rn	
								DCM	Expt.
(MeV)	(MeV)	(MeV)	(fm)	(mb)	(mb)	(mb)	(mb)	(mb)	(mb)
69.27	65.18	36.20	1.34	0.1615	0.0205	4.46×10^{-4}	7.35×10^{-4}	0.183	0.186
73.81	69.45	40.47	1.368	0.2626	0.0497	7.9×10^{-4}	7.76×10^{-4}	0.314	0.330
79.82	75.10	46.12	1.42	0.593	0.1329	2.1×10^{-3}	1.0×10^{-3}	0.729	0.757
85.85	80.78	51.80	1.455	0.9754	0.2562	7.11×10^{-3}	1.34×10^{-3}	1.24	1.269
91.87	86.44	57.46	1.466	1.1116	0.3454	6.86×10^{-3}	1.53×10^{-3}	1.465	1.490

contribute more towards the light particle emission (ER) where as the contribution of asymmetric fission fragments start contributing at higher ℓ value. (ii) the potential energy surfaces are almost similar for the two entrance channels ^{12}C+^{208}Pb and ^{13}C+^{207}Pb at ℓ=0 as well as at ℓ=ℓ_{max} values. The potential energy dip at fragment ^{17}B appears for ℓ=0 as well as ℓ=ℓ_{max} values independent of the entrance channel, possibly due to the use of inappropriate deformations for this fragment, but do not affect the cross sections as the emergence of this fragment is suppressed due to negligibly small penetrability. As almost identical fragments are preformed for both the channels so entrance channel effect seems absent from the analysis of fragmentation behavior. This fact is further emphasized in Fig. 4.2 which shows the preformation probability as a function of fragment mass number A_2. One may notice in Fig. 4.2 that maximum yields are obtained for the asymmetric region i.e the decay of ^{220}Ra* follows asymmetric behavior where fragments with A_2=82-93 (plus complementary heavy fragments) contribute towards fission cross sections. Further Fig. 4.2 shows a peak near the intermediate mass fragments (IMF) whose contribution is quite small. The contribution of IMF cross sections at lowest energy is of the order of 10^{-3} mb which increases to about 1mb at highest energy, independent of the choice of entrance channel. Therefore the contribution of IMF's is negligibly small in either of the chosen

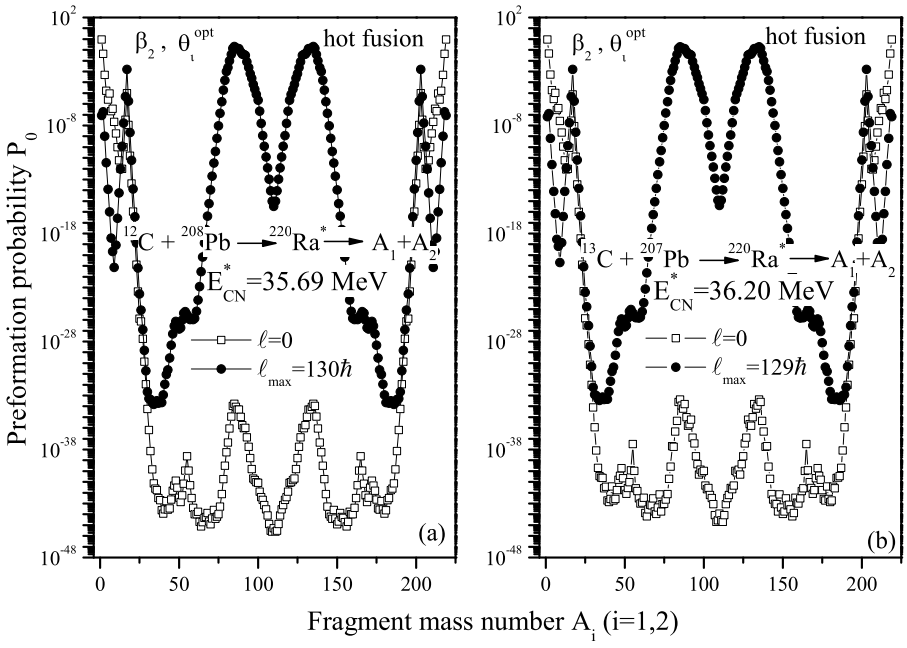

Figure 4.2 Preformation probability as a function of fragment mass number (A_i) (i=1,2) for the decay of ^{220}Ra* considering β_2 deformations at extreme ℓ values formed in (a) ^{12}C+^{208}Pb and (b) ^{13}C+^{207}Pb reaction channels.

reactions. From entrance channel point of view, Figs. 4.2 (a and b) clearly depict that the fragment profile of ER, IMF, and asymmetric fission distribution do not depend on the choice of entrance channel. For further validation of entrance channel independence, the decay barrier height are plotted as a function of fragment mass number for ^{12}C+^{208}Pb and ^{13}C+^{207}Pb reactions at extreme values of angular momentum in Fig. 4.3. It can be seen from Fig. 4.3 that the decay barrier height increases with ℓ as well as with fragment mass for both the reactions. Almost similar barrier height profile of all decaying fragments suggest that the entrance channel effects are not applicable in context of the chosen reaction.

Besides fission, there are different decay mechanism possible in the decay of ^{220}Ra* nuclear system that are ER, n-decay, and charged particle (αxn) etc.. Fig. 4.4 shows the preformation probability (P_0), of different decay mechanism of ^{220}Ra* nuclear system as a function of light fragment mass (A_2). It is clear from Fig. 4.4 that although different

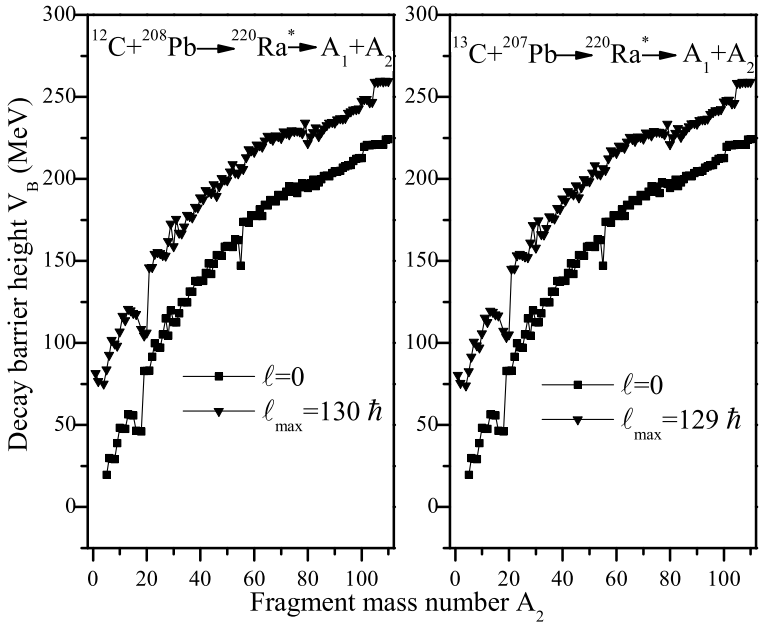

Figure 4.3 The barrier heights V_B as a function of light fragment mass number (A_2) for the decay of ^{220}Ra* considering β_2 deformations at extreme ℓ values for ^{12}C+^{208}Pb and ^{13}C+^{207}Pb reaction channels.

decay paths are possible in the dynamics of ^{220}Ra* but the preformation profile of decaying fragments do not change much i.e potential energy surfaces remain almost similar with some variation in magnitude. Only exception is the fission channel which shows the emergence of an IMF peak. In view of discussion of Fig. 4.2, the effective contribution of this IMF channel is negligible towards the total cross section. Therefore one may conclude that different decay mechanisms exhibit similar fragmentation paths in the decay of ^{220}Ra* nucleus. It may be noted here that the fragmentation path of different decay mechanism is calculated at different neck length parameter ($\triangle$R) values. Tables 4.1 and 4.2 show that ER, fission and neutron cross sections find nice comparison with experimental data for both the reactions. It may be noted that in DCM based calculations the cross section for 1n channel is dominant followed by 2n, 3n, 4n channels in sequence which is contrary to the experiment [12] where 3n-6n decay contribute for the ^{13}C+^{207}Pb reaction channel and 2n-6n cross sections are measured for ^{12}C+^{208}Pb reaction. It is relevant to mention

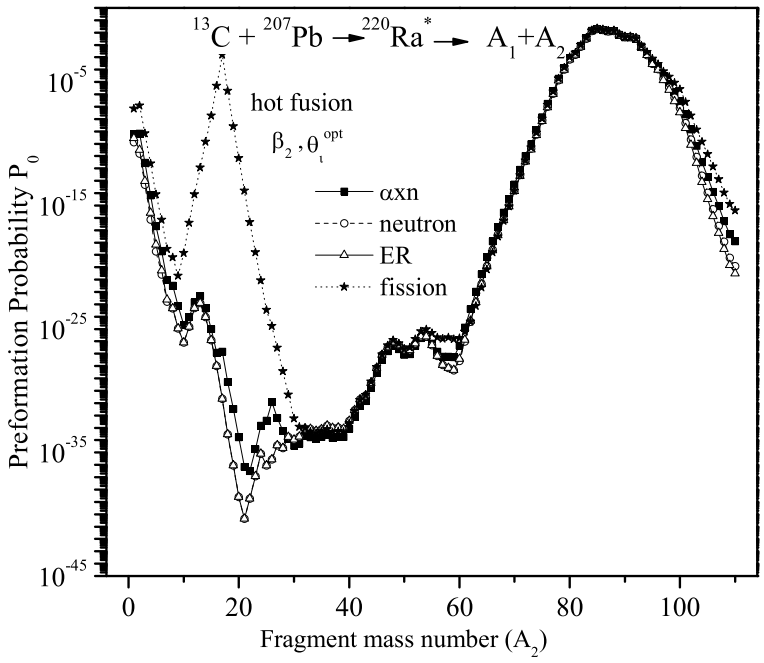

Figure 4.4 Preformation probability for the various possible decay mechanism of ^{220}Ra* as a function of fragment mass number (A_2).

here that owing to the range of nuclear interaction and nuclear surface thickness (≈2fm), the neck length "ΔR" is confined upto ≈2fm. Alternatively, if one takes ΔR>2fm then the neutron cross section data may also be achieved without inclusion of 1n or 2n decay contributions. But as the nuclear proximity interaction plays significant role in reaction dynamics, so the upper limit on ΔR is kept close to 2fm and as a consequence of this the contribution of 1n channel becomes indispensable. Table 4.1 and Fig. 4.5 (a and b) show the variation of △R as a function of E_{CN}. It can be seen from Fig. 4.5(a) that the △R values are higher for ER and lower in magnitude for fission, which implies the two processes are not occurring simultaneously. This statement is true for both the entrance channels ^{12}C+^{208}Pb and ^{13}C+^{207}Pb. One may see that independent of choice of entrance channel, the neck length parameter is almost identical for ER and for fission process. Therefore the neck length parameter (△R) also confirms the non-existence of entrance channel effects in the chosen reactions. Fig. 4.5(b) represents the △R variation

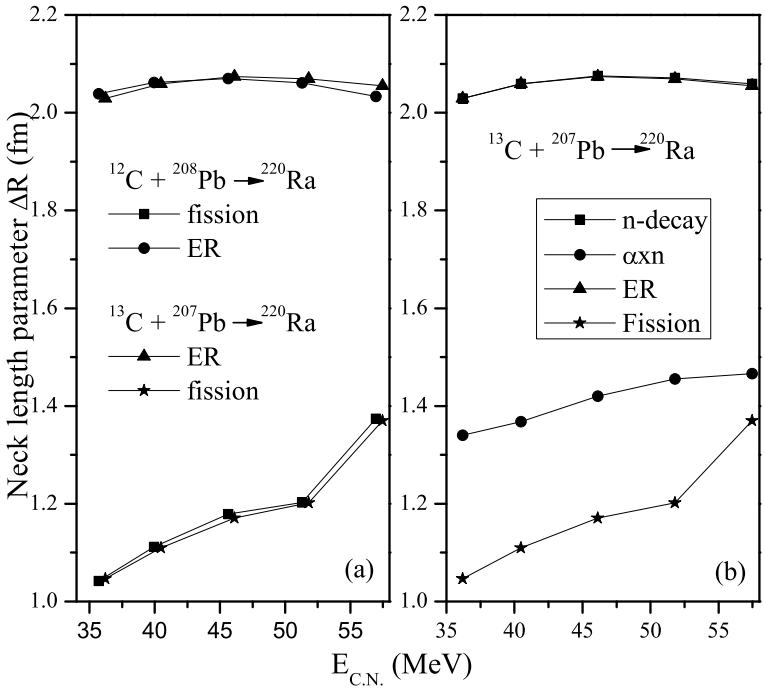

Figure 4.5 The fitted neck-length parameter (△R) for (a) fission and ER for the channels ^{12}C+^{208}Pb and ^{13}C+^{207}Pb (b) for various possible decay of ^{220}Ra* nuclear system formed in ^{13}C+^{207}Pb reaction.

for different decay mechanism for ^{13}C+^{207}Pb reaction channel. Fig. 4.5(b) shows that △R for n-decay is almost similar to ER. Also the neck length parameter △R for αxn decay is higher than fission but lower than ER. This implies that different decay proceses are occurring at different time scales. Higher values of ΔR means that the respective process occurs first, i.e. n-decay or ER occur first and αxn and fission follow in sequence. The ΔR is the only parameter of the model and its value decides the penetration point through the barrier.

By fitting the necklength parameter △R, the cross sections are calculated. It can be seen from Table 4.1 that the DCM calculated fission as well as ER cross sections find nice comparison with the experiment [12] for both the reaction channels, where $\sigma_{ER} = [\sigma_{CF} - \sigma_{fission}^{Expt}]$. It may be noted that fission cross sections are attributed solely to complete fusion as the partially fused composite following breakup is less fissile, as in ICF (discussed later in section 4.2.3) the part of projectile which fuses with target is

Table 4.4 The DCM calculated incomplete fusion (ICF) products resulting from the fusion of ^{9}Be (from ^{13}C) with ^{207}Pb forming ^{216}Rn* with the corrected center of mass energy, compared with the reported experimental values.

$E^{c}_{c.m.}$	T	$\triangle$R	ℓ_{max}	$\sigma_{1n}(^{215}$Rn)	$\sigma_{2n}(^{214}$Rn)	$\sigma_{3n}(^{213}$Rn)	$\sigma_{4n}(^{212}$Rn)	$\Sigma\sigma$Rn	
								DCM	Expt.
(MeV)	(MeV)	(fm)	($\hbar$)	(mb)	(mb)	(mb)	(mb)	(mb)	(mb)
45.96	1.232	1.445	135	5.89	0.118	4.55×10^{-4}	2.79×10^{-6}	6.0084	6.014±0.97
48.97	1.283	1.485	135	9.93	0.224	9.96×10^{-4}	7.7×10^{-6}	10.155	10.67±0.94
52.96	1.347	1.564	135	24.2	0.597	3.09×10^{-3}	2.91×10^{-5}	24.80	24.473±2.9
56.96	1.408	1.615	135	40.4	1.12	6.97×10^{-3}	6.8×10^{-5}	41.52	41.031±4.8
60.95	1.467	1.633	135	47.1	1.52	1.09×10^{-2}	1.25×10^{-4}	48.63	48.161±4.8

Table 4.5 The DCM calculated incomplete fusion (ICF) products resulting from the fusion of ^{8}Be (from ^{12}C) with ^{208}Pb forming ^{216}Rn* with the corrected center of mass energy, compared with the reported experimental values.

$E^{c}_{c.m.}$	T	$\triangle$R	ℓ_{max}	$\sigma_{1n}(^{215}$Rn)	$\sigma_{2n}(^{214}$Rn)	$\sigma_{3n}(^{213}$Rn)	$\sigma_{4n}(^{212}$Rn)	$\Sigma\sigma$Rn	
								DCM	Expt.
(MeV)	(MeV)	(fm)	($\hbar$)	(mb)	(mb)	(mb)	(mb)	(mb)	(mb)
45.90	1.124	1.5	133	10.5	0.162	5.38×10^{-4}	2.74×10^{-6}	10.662	10.674±1.76
48.79	1.178	1.6	133	36.5	0.63	2.3×10^{-3}	1.47×10^{-5}	37.13	37.549±2.64
52.64	1.245	1.643	133	55.6	1.11	4.69×10^{-3}	3.82×10^{-5}	56.7	57.279±4.4
56.49	1.309	1.687	133	82.9	1.87	8.76×10^{-3}	8.69×10^{-5}	84.8	84.894±4.4
60.34	1.370	1.703	133	92.0	2.33	1.34×10^{-2}	1.41×10^{-4}	94.4	94.609±3.52

having lower angular momentum than that for the actual projectile. Consequently in ICF process, the reduced compound nucleus so formed is less fissile and hence prefers to decay via neutron evaporation with negligible contribution towards fission.

Another decay mechanism investigated in [12] is αxn i.e charged particle decay. After the evaporation of the neutrons from ^{220}Ra* compound nucleus, the reminisce residue left is α active which undergo α-emission to form Radon (Rn) isotopes. Table 4.3 shows the contribution of various isotopes of Rn towards total Rn cross sections calculated for the best fit to the experimental σ_{Rn} cross sections. It is important to note that DCM calculations suggest most prominent contribution for α1n channel, followed by α2n. On

the other hand α3n and α4n channel contribution towards αxn cross sections is negligibly small. It may be noted here that the αxn decay channel leads to Radon (Rn) isotopes which may also be populated through ICF (this point is explored further in section 4.2.3). The Radon (Rn) isotopes are populated via complete fusion (CF) as follows: when the projectile ^{13}C completely fuses with ^{207}Pb target nucleus to form excited ^{220}Ra*, it may decay via neutron evaporation leaving an α-active leftover residue. This residual nucleus then decays via α-emission giving rise to Rn isotopes forming αxn decay channel.

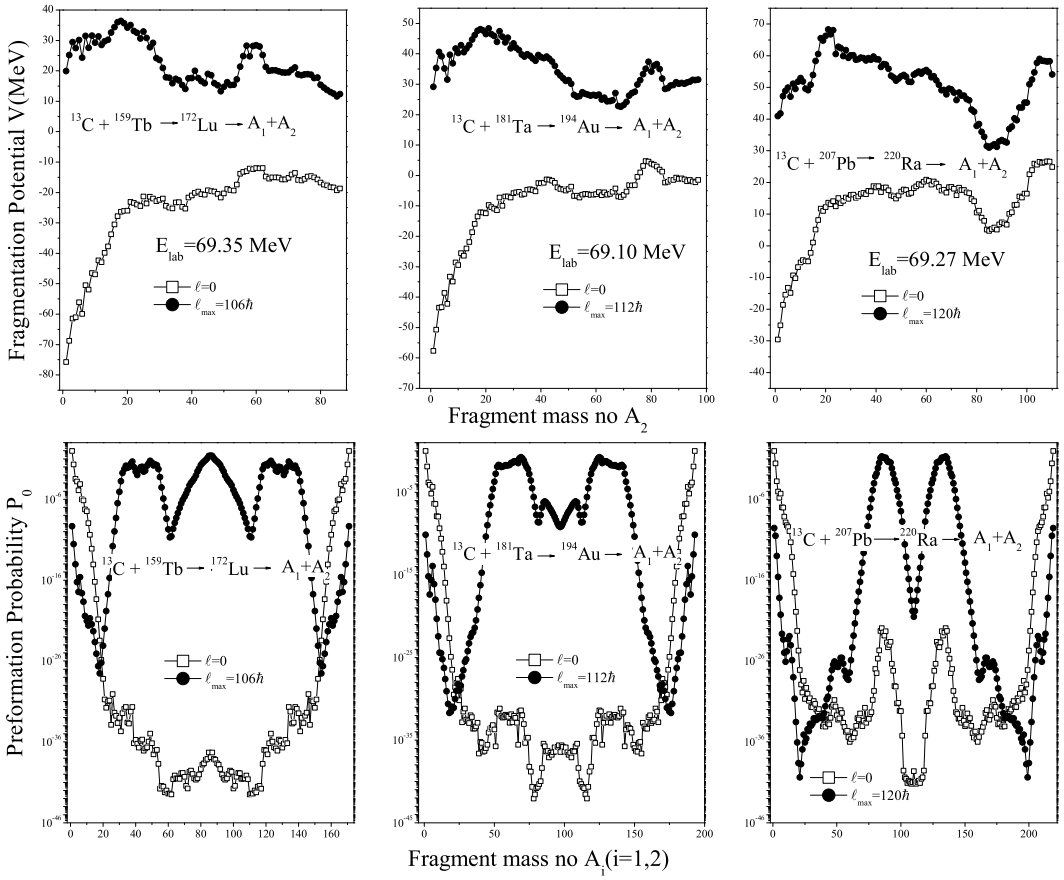

Figure 4.6 Fragmentation potential as a function of fragment mass number (A_2) for the ^{13}C+^{159}Tb, ^{13}C+^{181}Ta, ^{13}C+^{207}Pb reaction channels in the upper panel and Preformation probability as function of fragment mass for the same reactions in the lower panel considering β_2 deformation at a comparable E_{lab} value.

4.2.2 Effect of target mass on fragmentation path

In order to investigate the fragmentation behavior when the target mass changes from medium to heavy mass keeping the projectile same, the dynamics of ^{13}C+^{159}Tb, ^{13}C+^{181}Ta and ^{13}C+^{207}Pb reactions forming compound systems ^{172}Lu, ^{194}Au, ^{220}Ra respectively have been studied, having mass asymmetry η=0.848, 0.865, 0.881 i.e all the chosen reactions correspond to asymmetric target-projectile combinations. Fig. 4.6 shows the fragmentation potential (upper panel) and preformation probability (lower panel) for the above mentioned reaction channels at a comparable incident energy $E_{lab} \approx 69$ MeV. Fig. 4.6 depicts that the mass distribution of ^{172}Lu is symmetric with shoulders of asymmetric fragments however for ^{194}Au, the asymmetric fragments are more favorable than the symmetric fragments i.e the mass distribution shows marginal contribution for the symmetric fragments which altogether vanishes for ^{220}Ra which follows completely asymmetric mass distribution in the fissioning region. So it can be inferred that keeping the projectile same if the target is varied from medium mass to heavier mass, the mass distribution changes from near symmetric to asymmetric.

After comprehensive analysis of CF process, the relative ICF contribution in the above mentioned reaction channels is analyzed in the following subsection.

4.2.3 Contribution of incomplete fusion (ICF)

As discussed earlier, the loosely bound projectile may break up prior to fusing with the target and contribute towards ICF cross sections. In reference to the experiment [12], the ICF cross sections are calculated involving the break up of ^{12}C as well as that of ^{13}C projectile. The Radon (Rn) isotopes as discussed earlier are populated via CF and ICF processes. In the ICF process, the projectiles ^{12,13}C may break up into its constituents α cluster as (^{8,9}Be+^{4}He) respectively. One of the fragment ^{8}Be fuses with the target ^{208}Pb

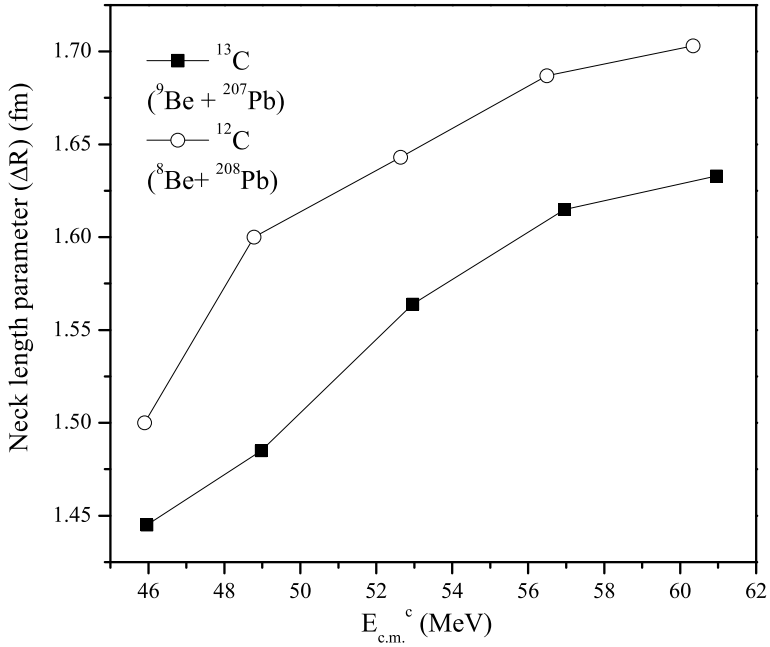

Figure 4.7 The fitted neck-length parameter ($\triangle$R) as a function of corrected center of mass energy for the ICF process for both the channels.

in case of ^{12}C projectile and ^{9}Be fuses with the target ^{207}Pb in case of ^{13}C projectile to form residual compound system ^{216}Rn and the remnant (^{4}He) behaves as a spectator. The new compound system so formed may decay via neutron emission to produce Rn isotopes. This can be understood as

^{12}C(^{8}Be+^{4}He)+^{208}Pb$\rightarrow$^{216}Rn$\rightarrow$A$_1$+A$_2$

^{13}C(^{9}Be+^{4}He)+^{207}Pb$\rightarrow$^{216}Rn$\rightarrow$A$_1$+A$_2$

The above reactions in which fragment ^{8}Be of ^{12}C projectile and ^{9}Be of ^{13}C projectile interact respectively with ^{208}Pb and ^{207}Pb targets are termed as ^{8,9}Be transfer reactions and the other fragment ^{4}He acts as a spectator. The newly formed composite system ^{216}Rn undergo neutron evaporation to form different isotopes of Rn. To study this incomplete fusion (ICF) process, one has to apply the corrections in the incident energy involved, in view of the breakup of the projectile prior to its interaction with target. Assuming that energy is shared equally among all the nucleons of the projectile, the modified energy of new projectile is calculated as stated in [6]. Consequently, the ICF cross sections are

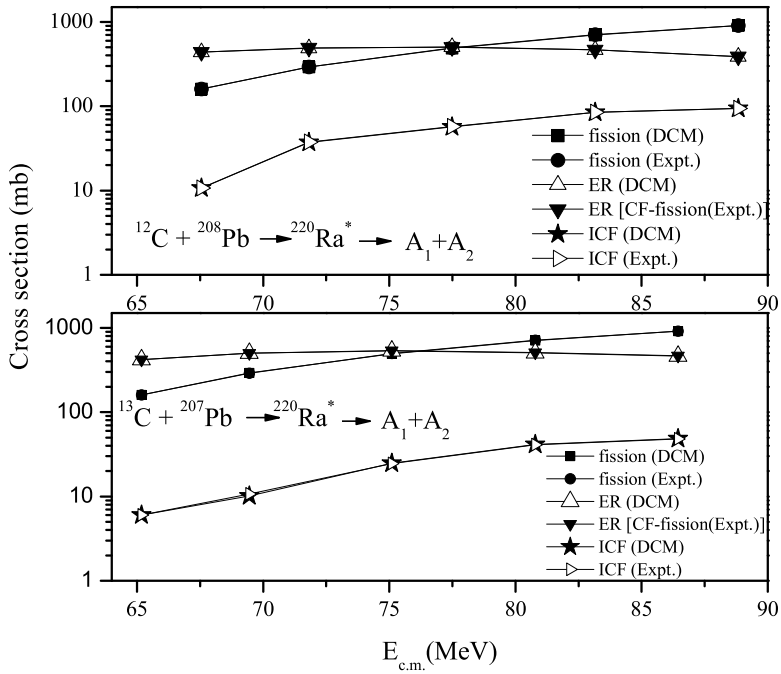

Figure 4.8 DCM calculated fission, ER and incomplete fusion (ICF) cross sections compared with experimental cross section values.

calculated within DCM for the channels ^{12}C+^{208}Pb and ^{13}C+^{207}Pb. Table 4.4 and Table 4.5 show the ICF cross section calculated using DCM, which find nice agreement with the reported experimental data of [12]. The cross sections are calculated within DCM by fitting the neck length parameter. Fig. 4.7 shows the variation of ΔR for the ICF process as a function of corrected center of mass energy for both the reaction channels involving breakup of ^{12}C and ^{13}C. Fig. 4.7 shows that the ΔR values are higher in magnitude for ^{12}C channel as compared to that for ^{13}C. On the other hand neck length parameter increases with energy for both the reaction channels. The ICF contribution increases with energy, which simply mean that the breakup probability of the projectile increases with energy. The Tables 4.1-4.5 and Fig. 4.8 clearly show that DCM calculated ER, n-decay, fission, αxn and ICF cross sections find nice agreement with experimental data for both the reaction channels. One may note that ER dominates at lower energies but fission cross sections are larger at higher energies and the contribution of ICF cross sections is much

lower at all energies. Further to explore the ICF systematics, the ICF% is calculated as ICF%=$\frac{\sigma_{ICF}}{\sigma_{TF}}$×100 (where σ_{TF}=σ_{CF} + σ_{ICF}) and is plotted as a function of Z_pZ_t (proton

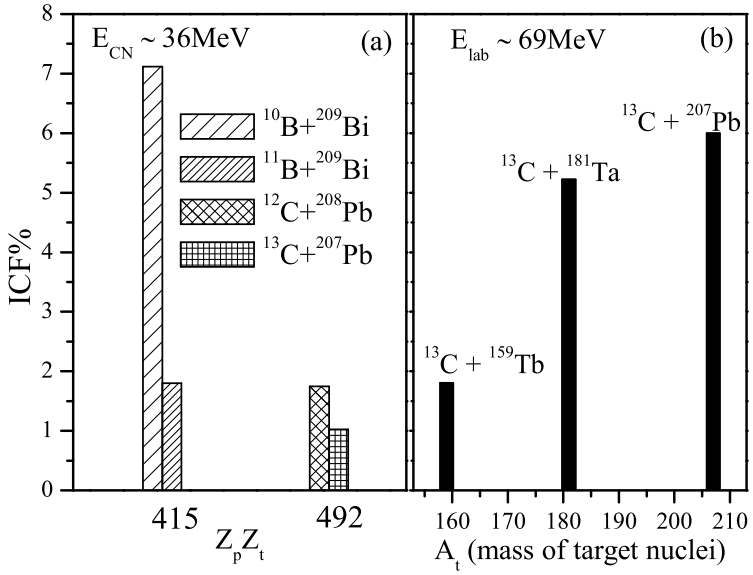

Figure 4.9(a)ICF% as a function of Z_pZ_t for ^{10,11}B and ^{12,13}C induced reactions. (b) ICF% as a function of target mass (A_t) for the ^{13}C+^{159}Tb, ^{13}C+^{181}Ta and ^{13}C+^{207}Pb reactions.

number of projectile and target respectively). It can be seen from Fig. 4.9 (a) that at a particular value of Z_pZ_t, the ICF% is higher for the channel having projectile with lower N/Z value (i.e for more asymmetric channel) which is consistent with the morgenstern systematics [13]. The data for ^{12,13}C at a comparable energy is fitted using DCM in reference to experiment [12] and the same for ^{10,11}B is taken from [9, 17]. In Fig. 4.9(a), ^{11}B and ^{12,13}C projectiles are forming the same compound nucleus ^{220}Ra* and compound nucleus ^{219}Ra* is formed in case of ^{10}B projectile. In other words Fig. 4.9(a) represents the systematics of different target projectile combinations forming same/ similar compound system. In the following, the systematics of ICF cross sections are emphasized, when a loosely bound projectile hits a variety of targets with increasing mass. Here ^{13}C is considered as the projectile incident on different targets forming ^{13}C+^{159}Tb, ^{13}C+^{181}Ta, ^{13}C+^{207}Pb reaction channels where the projectile ^{13}C breaks up into an ^{4}He and ^{8,9}Be. The

ICF cross sections for these three reactions are fitted in reference to data of [12, 18, 19], whose CF profile is discussed in Fig. 4.6. It may be noted that in Fig. 4.9(b), the contribution of both the cases (when ^{8,9}Be fuses with the target and ^{4}He acts as a spectator and other, when ^{4}He fuses with the target and ^{8,9}Be act as a spectator) have been taken into consideration to account for the ICF cross sections. The ICF% as a function of A_t (mass of target) is plotted in Fig. 4.9(b) . It is clear from Fig.4.9(b) that ICF% increases with increase in mass of the target. It can be said that for asymmetric reaction channels if the projectile remains same, the ICF% increases as a function of target mass (A_t). The fragmentation profile of composite systems formed in ICF channel of ^{13}C induced reactions discussed in Fig. 4.9(b) is depicted in Fig. 4.10. A closer look of Fig. 4.6 (upper panel) and Fig. 4.10, suggest that there is no significant change in the potential energy surfaces formed in CF (Fig. 4.6) and ICF (Fig. 4.10) process. The switching of behavior from near symmetric to asymmetric with increase in target mass seems evident for either of the two processes.

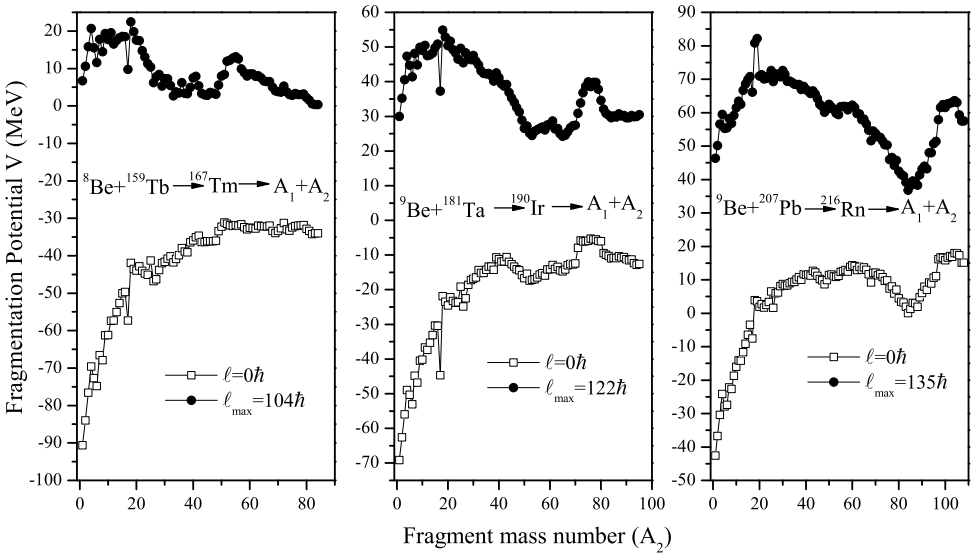

Figure 4.10 Fragmentation potential as a function of fragment mass number (A_2) for the ICF process in ^{13}C+^{159}Tb, ^{13}C+^{181}Ta and ^{13}C+^{207}Pb reaction channels.

4.3 Summary

In this chapter, the excitation functions are calculated for the decay of $^{220}Ra^*$ compound nucleus formed in $^{12}C+^{208}Pb$ and $^{13}C+^{207}Pb$ reaction channels using DCM approach. Different decay paths of $^{220}Ra^*$ involving n-decay, ER, fission, charged particle decay (αxn) and competing ICF process are investigated and the calculated cross sections find nice comparison with the experimental data. The fitted neck length parameter is higher for ER and n-decay as compared to that for fission. The neck length parameter for αxn and ICF is observed to be inbetween that for ER and fission process. Consequently, it is concluded that ER or n-decay occur almost simultaneously at an early stage, followed by ICF, αxn and fission decay in sequence. The neck length parameter exhibit nice description of sequence regarding the occurance of different decay possibilities. On the basis of fragmentation path, preformation profile, angular momentum, barrier characteristics and neck length parameter, the entrance channel effect seems to be absent in context of the chosen reactions. Besides this, the fragmentation behavior of different nuclear systems formed by striking ^{13}C projectile on increasing mass targets is explored using CF and ICF process, which shows that the mass distribution changes from near symmetric to asymmetric when the target changes from medium mass to heavy mass region. The ICF% systematics is worked out as a function of compound nucleus mass and target mass.

Bibliography

[1] M. Kaur, R. Kumar and M. K. Sharma, Phys. Rev. C **85**, 014609 (2012). M. Kaur and M. K. Sharma, Phys. Rev. C **85**, 054605 (2012).

[2] M. Kaur, M. K. Sharma and Raj K. Gupta, Phys. Rev. C **86**, 064610 (2012).

[3] B. B. Singh, M. K. Sharma and R. K. Gupta, Phys. Rev. C **77**, 054613 (2008).

[4] M. K. Sharma, S. Kanwar, G. Sawhney, R. K. Gupta and W. Greiner, J. Phys. G: Nucl. Part. Phys. **38**, 055104 (2011). D. Jain, R. Kumar, M. K. Sharma and R. K. Gupta, Phys. Rev. C **85**,024615 (2012).

[5] S. Kanwar, M. K. Sharma, B. B. Singh, R. K. Gupta and W. Greiner, Int. J. Mod. Phys E **18**, 1453 (2009).

[6] G. Kaur and M. K. Sharma, Nucl. Phys. A **884**, 36 (2012). G. Kaur and M. K. Sharma, Phys. Rev. C **87**, 044601 (2013).

[7] M. K. Sharma, G. Sawhney, R. K. Gupta and W. Greiner, J. Phys. G: Nucl. Part. Phys. **38**, 105101 (2011). M. K. Sharma, S. Kanwar, G. Sawhney and R. K. Gupta, Phys. Rev. C **85**, 064602 (2012).

[8] K. Sandhu, M. K. Sharma and R. K. Gupta, Phys. Rev. C **85**, 024604 (2012). K. Sandhu, M. K. Sharma and R. K. Gupta, Phys. Rev. C **86**, 064611 (2012).

[9] G. Sawhney and M. K. Sharma, Eur. Phys. J. A **48**, 57 (2012).

[10] M. Kaur and Manoj K. Sharma, *International Conference On Recent Trends in Nuclear Physics-2012*, published in AIP conf. proc. **1524**, pp.151-154 (2013).

[11] R. K. Gupta, M. Balasubramaniam, R. Kumar, N. Singh, M. Manhas and W. Greiner, J. Phys.G : Nucl. Part. Phys. **31**, 631 (2005).

[12] K. Kalita, J. Phys. G: Nucl. Part. Phys. **38**, 095104 (2011).

[13] H. Morgenstern, W. Bohne, W. Galster, K. Grabisch, and A. Kyanowski, Phys. Rev. lett. **52**, 1104 (1984).

[14] L. F. Canto et al, Phys. Rep. **424**, 1 (2006).

[15] N. Keeley et al, Prog. Part. Nucl. Phys. **59**, 579 (2007).

[16] P. Moller, J. R. Nix, W. D. Myers, W. J. Swiatecki, At. Data Nucl. Data Tables, **59**, 185 (1995).

[17] L. R. Gasques, D. J. Hinde, M. Dasgupta, A. Mukherjee, R. G. Thomas, Phys. Rev. C **79**, 034605 (2009).

[18] A. Yadav, V. R. Sharma, P. P. Singh, R. Kumar, D. P. Singh, Unnati, M. K. Sharma, B. P. Singh and R. Prasad, Phys. Rev. C **86**, 014603 (2012).

[19] K. S. Babu, R. Tripathi, K. Sudarshan, B. D. Shrivastava, A. Goswami and B. S. Tomar, J. Phys. G: Nucl. Part. Phys. **29**, 1011-1022 (2003).

Chapter 5

Decay mechanism of ^{204}Po* compound nucleus formed in ^{16}O and ^{28}Si induced reactions

In this chapter, the decay of hot and rotating compound nucleus ^{204}Po* formed in ^{16}O + ^{188}Os and ^{28}Si + ^{176}Yb reaction channels is studied using the DCM by simultaneously fitting the necklength parameter "ΔR". It is important to note here that so far in this thesis the calculations are done by fitting the neck length parameter independently for various decay processes (i.e ER, fission etc.) to calculate the respective cross sections. However in this chapter, the calculations are done by simultaneously fitting the neck length parameter for the ER and fission process. Depending upon the mass asymmetry of the entrance channel, the possibility of CN and nCN component is explored in the decay of ^{204}Po*. This work is published in [1].

5.1 Introduction

As we know, the decay of heavy nuclear systems under the extreme conditions of temperature, angular momentum, deformations etc. has been studied extensively in recent times in order to find useful information regarding fusion-fission and other competing decay processes. The fusion cross-section is the sum of measured cross-section due to evaporation residue, fission and other competing decay processes. After the capture of the projectile into target nucleus, the system so formed may reseparate prematurely, i.e without forming a true compound nucleus. Such events represent the transition between non compound nucleus (nCN) processes and complete fusion. In deep inelastic collision (one of the nCN processes) the entrance channel mass asymmetry is preserved but it involves large dissipation of kinetic energy and angular momentum [2] whereas compound nucleus (CN) formation involves complete loss of identity of the entrance channel and it equilibrates in all degrees of freedom. In addition to this, it is quite important to explore the fusion hinderance phenomena and its implications in reference to nuclear dynamics. Fusion hinderance in pre-actinide region is an important area of research in the field of heavy ion reactions. The observation of fusion hinderance is attributed to different phenomena, one of them being the entrance channel mass asymmetry, $\alpha=\frac{A_t-A_p}{A_t+A_p}$ (A_t, A_p being the mass number of target and projectile respectively). If $\alpha<\alpha_{BG}$ (Businaro Gallone mass asymmetry) [3] then there may be some contribution from non-compound nucleus (nCN) decay.

Recently fission cross sections were measured [4] for $^{16}O + {}^{188}Os \rightarrow {}^{204}Po^*$ reaction over a wide range of incident energies (E_{lab} = 84-99 MeV). This fission cross section data was used to extract statistical model parameters and consequently complete fusion and evaporation residue cross-sections for $^{16}O + {}^{188}Os \rightarrow {}^{204}Po^*$ and $^{28}Si + {}^{176}Yb \rightarrow {}^{204}Po^*$ reactions were predicted respectively using the code CCFUS [5] and CASCADE [6] over an energy

range (E_{lab} = 84-155 MeV). The reaction channels ^{16}O + ^{188}Os and ^{28}Si +^{176}Yb are having different mass asymmetry α, i.e for the entrance channel ^{16}O + ^{188}Os, α=0.84 which is almost the same as the α_{BG} [3] value of 0.85. Thus, according to the pre-equilibrium fission model [7, 8], contribution from non-compound nucleus fission is not expected in this reaction. However for the ^{28}Si +^{176}Yb channel, α = 0.73 which is lower as compared to α_{BG} value of 0.85. Therefore some amount of nCN is expected for ^{28}Si induced reaction. Also for the reaction system with large entrance channel Coulomb repulsion (Z_p Z_t product, Z_p,Z_t being the proton number of projectile and target respectively) the fusion hinderance or non compound nucleus (nCN) process is expected to contribute. Based on the work [9] it was proposed that, the fusion hinderance or non compound nucleus (nCN) fission is expected around Z_p Z_t ≈1000. It may be worth noting that the product Z_p Z_t is 608 and 980 respectively for ^{16}O and ^{28}Si induced channel. Therefore ^{28}Si induced channel being close to predicted limit, seems a possible candidate for nCN process.

In the present work, decay of ^{204}Po* for the two entrance channels ^{16}O + ^{188}Os and ^{28}Si +^{176}Yb have been studied using Dynamical cluster decay model (DCM) [10]- [19]. The evaporation residue cross-sections and fission cross-sections are worked out over wide range of center of mass energies in reference to [4]. The calculations are done by fitting the only parameter ΔR (neck-length parameter) simultaneously for both evaporation residue and fission. The calculations are started with the spherical choice of fragmentation however it is observed that the role of deformations is extremely desirable in order to fit the available data. Therefore the deformation and orientation effects are included to calculate the ER and fission cross sections. The fission fragment anisotropies are also calculated using non-sticking limit of moment of inertia and the effect of adding two neutrons is seen by comparing ^{204}Po* decay with ^{202}Po* nucleus, both being formed in ^{16}O induced reaction at comparable $E_{c.m.}/V_c$ value.

5.2 Calculations

The decay of ^{204}Po* nuclear system formed in ^{16}O + ^{188}Os and ^{28}Si +^{176}Yb reaction channels is studied considering the spherical as well as deformed choice of fragmentation. In section 5.2.1, the behavior of fragmentation potential, preformation probability, penetrability, decay barrier height, barrier lowering effect, fusion excitation function due to both fission and ER is discussed and looked for the possibility of nCN process in context of these reactions. In section 5.2.2, fission fragment anisotropy is calculated using ℓ-values within non-sticking approach and finally in section 5.2.3, the effect of adding neutrons in ^{202}Po* nucleus is explored.

5.2.1 Fusion excitation function [ER and fission]:

The decay of ^{204}Po* nucleus formed in ^{16}O + ^{188}Os and ^{28}Si +^{176}Yb reaction channels is studied over a wide range of center of mass energies and having comparable $E_{c.m.}/V_c$ value in reference to experimental data [4].

Calculations are made within DCM using different ΔR (neck-length parameter), chosen to fit the available experimental data [4] along with the ER data calculated using the code CASCADE [6] and the complete fusion cross-sections calculated using the code CCFUS [5]. The ER cross section data was subtracted from the complete fusion cross-section data to get the cross-sections for fission (see Table 5.1). Fig. 5.1 shows the fragmentation potentials for the decay of ^{204}Po* formed in the above mentioned reactions at the extreme ℓ values, using spherical fragmentation as well as for the deformation effects of β_{2i} at optimum orientations of hot compact configurations. It may be noted that only fission data is fitted with spherical choice of fragmentation and hence the deformation effects upto β_2 are included to account for total fusion cross-sections. The optimum orientations θ_i^{opt} are uniquely fixed on the basis of the quadrupole deformation alone of nuclei [13].

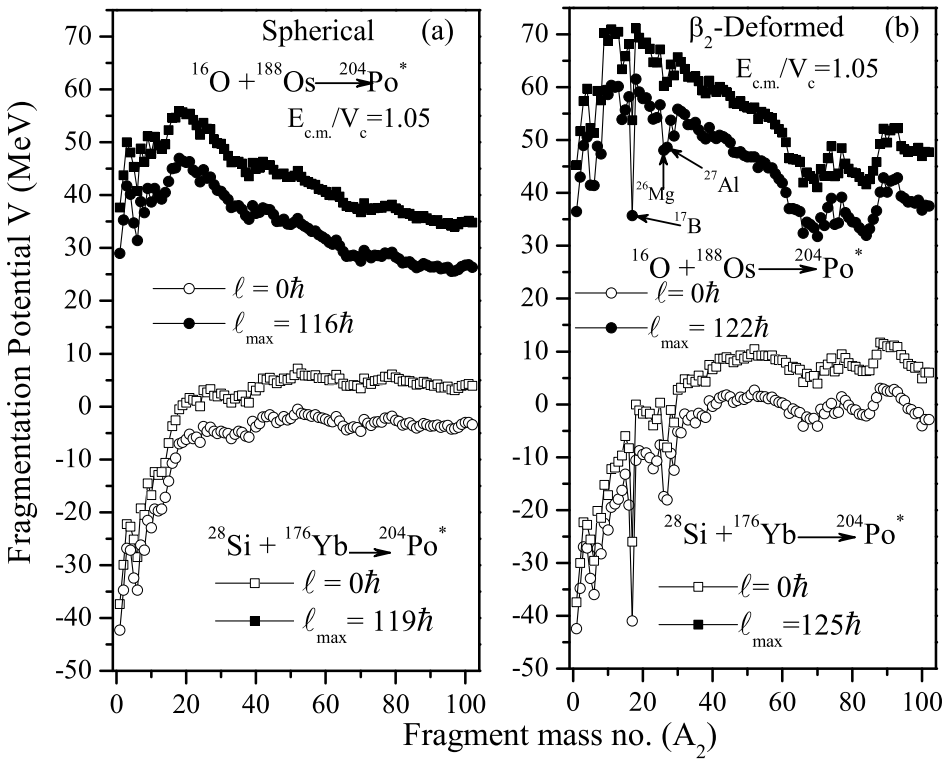

Figure 5.1 Fragmentation potential as a function of light mass fragment A_2 for the decay of $^{204}Po^{*}$ formed in ^{16}O + ^{188}Os and ^{28}Si +^{176}Yb reaction channels at comparable $E_{c.m.}/V_c$ value using (a) spherical and (b) β_2-deformed considerations.

In order to make comparison between the two incoming channels ^{16}O + ^{188}Os and ^{28}Si +^{176}Yb, the fragmentation path is plotted at comparable $E_{c.m.}/V_c$ value in Fig. 5.1. It can be seen from Fig. 5.1 that the fission distribution is clearly symmetric for spherical (non-deformed) decaying fragments and becomes asymmetric when β_2-deformation effects are included. This means that the structure of potential energy surfaces changes significantly with the inclusion of deformation and orientation effects at lower as well as at higher ℓ-values. This implies that deformations play an important role in the decay of pre-actinide nuclear system $^{204}Po^{*}$ almost independent of the entrance channel. The fragmentation potential show some dips in case of deformed considerations which are missing in the spherical choices of fragmentation. Although the sharp minima in the β_2-deformed fragmentation show the preference for the clusters (^{17}B,^{26}Mg,^{27}Al) but they get ruled out

because of their small penetrability as shown in Fig. 5.4.

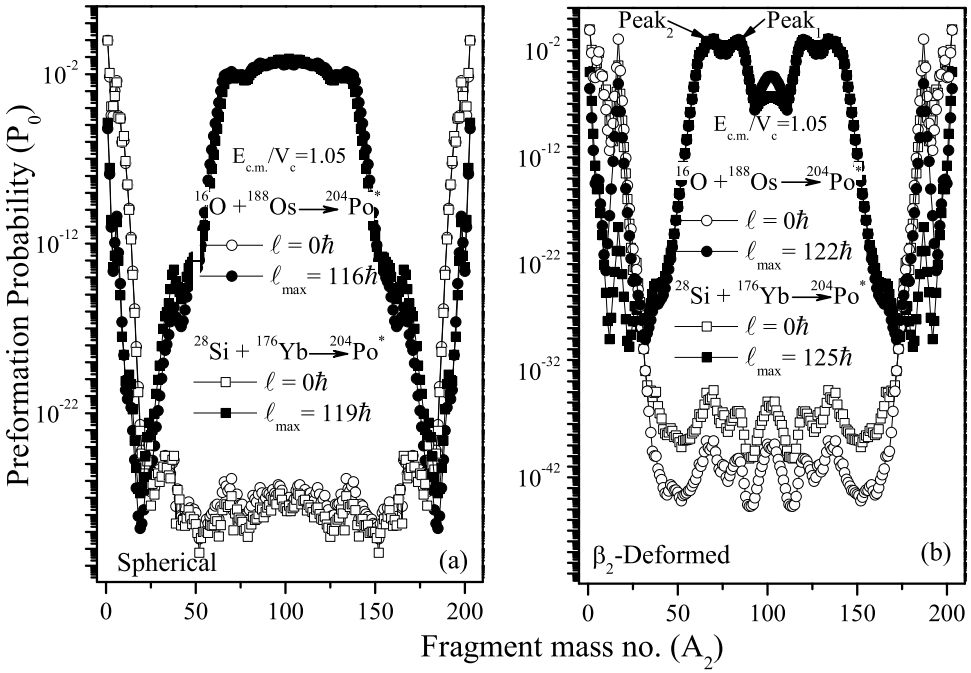

Figure 5.2 Preformation probability as a function of fragment mass number (A_2) for the decay of ^{204}Po* formed in ^{16}O + ^{188}Os and ^{28}Si +^{176}Yb reaction channels at comparable $E_{c.m.}/V_c$ value using (a) spherical and (b) β_2-deformed choice of fragmentation at extreme ℓ values.

Fig. 5.2 shows the behavior of preformation probability as a function of fragment mass A_2 for the decay of ^{204}Po* formed in the reaction channels ^{16}O + ^{188}Os and ^{28}Si +^{176}Yb at extreme ℓ values for the spherical and deformed choice of fragmentation. It is further clear from Fig. 5.2 that fission distribution is symmetric for spherical case however with inclusion of β_2-deformation and orientation effects asymmetric fragments show dominance i.e the fragment mass distribution for the decay of ^{204}Po is asymmetric in nature for the β_2-deformed choice of fragmentation.

Within the contributing fission fragments in β_2-deformed path, there seems a shoulder structure (asymmetric peak) which gives rise to possibilities of sub structure among fission fragments. One may clearly see a double humped fission distribution for both the channels for the deformed choice and fragments A_2= 65-72, 75-76, 79-86 seem to con-

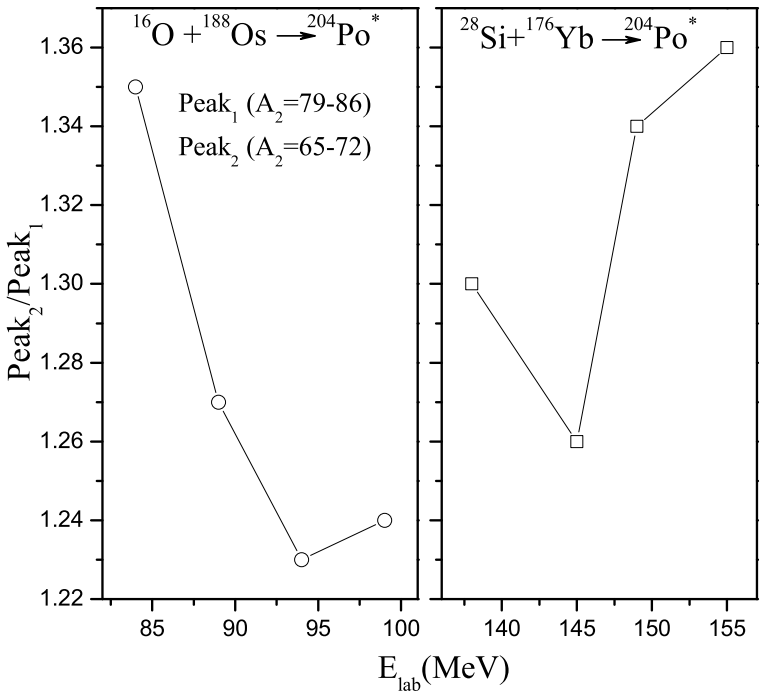

Figure 5.3 The ratio of the peak values of asymmetric fragments and near symmetric fragments window as a function of E_{lab}.

tribute towards fission cross-sections. The possible sub structure among fission fragments is studied by calculating asymmetric peak to near symmetric peak ratio ($\frac{Peak_2}{Peak_1}$) as shown in Fig. 5.3. One may notice in Fig. 5.3 that Peak$_2$ (A$_2$=65-72) contributes more than Peak$_1$ (A$_2$=79-86), further strengthening the fact that contribution of asymmetric fission fragments dominates the fission cross-sections. The contribution of in between fragments (A$_2$=75-76) is quite small.

It is important to note that there is significant difference between entrance channel Coulomb repulsion (Z_pZ_t product) for these reactions. Therefore the broadening in the fission fragment mass distribution is expected specifically for $^{28}Si + ^{176}Yb \rightarrow ^{204}Po^{*}$ as Z_pZ_t for this reaction is quite close to the onset suggested for fusion hinderance [9]. However one may see from Fig. 5.1 and 5.2 that fission fragment mass distribution is almost identical in both the reactions and seem to behave similarly at two extreme ℓ-values despite having significant mass asymmetry variation. Also at ℓ=0, ER is dominant whereas the

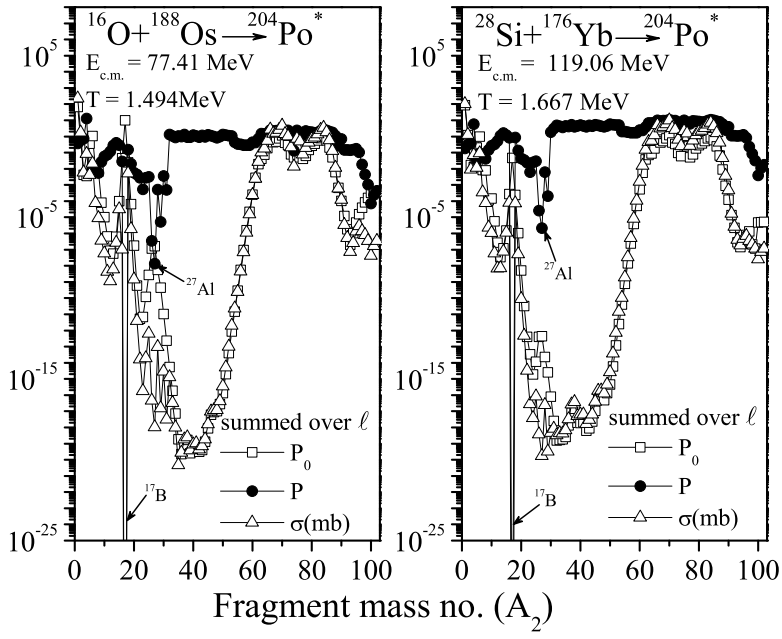

Figure 5.4 The ℓ-summed preformation probability (P_0), penetrability (P) and cross section (σ) as a function of fragment mass number (A_2) for the decay of ^{204}Po* formed in ^{16}O + ^{188}Os and ^{28}Si +^{176}Yb reaction channels at comparable $E_{c.m.}/V_c$ value.

situation gets reversed at higher ℓ-values i.e fission fragments start competing with evaporation residue (ER) process at higher ℓ-values independent of entrance channel. Therefore entrance channel effects seem absent at least on the fragmentation and preformation behavior point of view. The contribution of asymmetric peak (Fig. 5.3) is also dominant in either of the channels. However one may see in Fig. 5.3 that for ^{16}O induced channel peak$_2$ becomes relatively weak with increase in projectile energy whereas reverse trend is observed for ^{28}Si induced reaction. But as the energy range for ^{16}O and ^{28}Si induced reactions is quite different so the above observation need further investigations at comparable E_{lab} values.

Fig. 5.4 shows the ℓ-summed preformation probability (P_0), penetrability (P) and cross-section (σ) as a function of fragment mass number A_2 for the two channels at comparable $E_{c.m.}/V_c$ value. It can be seen from Fig. 5.4 that the cross-sections follow the behavior of P_0, indicating that P_0 carries the necessary nuclear structure information.

Table 5.1 DCM calculated decay cross-sections for ER (σ_{ER}) and fission ($\sigma_{fission}$) for the decay of $^{204}Po^*$ formed in ^{16}O + ^{188}Os and ^{28}Si +^{176}Yb reaction channels considering β_2 deformed choice of fragmentation, compared with the available data [4].

E_{lab}	$E_{c.m.}$	T	ℓ_{max}	$\triangle R$		$\sigma_{fission}$			σ_{ER}	
				ER	fission	DCM	Expt [4]	CC [5]-C [6]	DCM	C [6]
(MeV)	(MeV)	(MeV)	($\hbar$)	(fm)	(fm)	(mb)	(mb)	(mb)	(mb)	(mb)
^{16}O + $^{188}Os \rightarrow ^{204}Po$										
84	77.41	1.494	122	1.860	1.040	58.4	60.5	51	230	234
89	82.02	1.562	123	1.858	1.138	160.4	160.53	171	318	328
94	86.63	1.627	125	1.856	1.210	330	330.69	369	322	322
99	91.24	1.689	126	1.836	1.237	500	505.10	590	270	273
^{28}Si +$^{176}Yb \rightarrow ^{204}Po$										
138	119.06	1.667	125	1.765	1.154	132.4	-	137	103	103
145	125.10	1.746	128	1.752	1.225	318	-	319	101	103
149	128.55	1.790	128	1.738	1.253	428	-	433	90.7	91
155	133.73	1.853	131	1.687	1.500	480	-	606	64.2	65

*CC refers to CCFUS and C refers to CASCADE

One may notice that ℓ-summed P is almost constant as a function of fragment mass number A_2 and thus contributes mainly to the magnitude of cross section and not to the structure, however the deeper minima for P means that the contribution of these fragments is negligibly small. It may be noted that dips in Fig. 5.4 for penetrability (P) correspond to the potential energy surface dips shown in Fig. 5.1(b) which arise possibly due to inappropriate choice of deformation values. However these deeper minima in P, don't make significant difference in context of present calculations as enhanced preformation factor (P_0) is counterbalanced by negligible penetration values. Furthermore, one may notice in Fig. 5.4 that P_0 and cross-section (σ) for the upper end of HMFs or asymmetric fission fragments start comparing with ER, indicating that ER and fission are competing with each other. From Table 5.1, it is clear that fission dominates at higher energies whereas ER is much preferred decay path at relatively smaller incident energies.

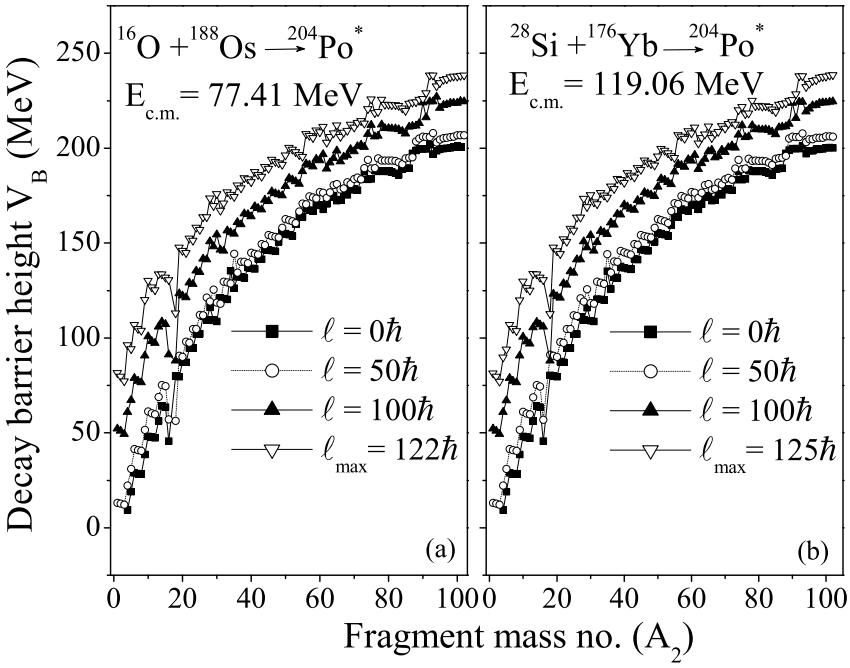

Figure 5.5 The barrier heights V_B as a function of fragment mass number (A_2) for the decay of ^{204}Po* formed in ^{16}O + ^{188}Os and ^{28}Si +^{176}Yb reaction channels at various ℓ- values.

Now to see the effect of entrance channel and angular momentum (ℓ), the barrier heights V_B is plotted as a function of fragment mass A_2 for the decay of ^{204}Po* formed in the above mentioned reaction channels at various ℓ-values in Fig. 5.5. It is clear from Fig. 5.5 that the decay barrier-height increases as a function of fragment mass, independent of the entrance channel as well as the angular momentum (ℓ) values. This behavior is in agreement with the one observed for heavy compound nucleus ^{215}Fr* [18] where fission is the major contributor for decay cross-sections. However this ℓ-dependence behavior is contrary to the one for lighter nuclear system ^{48}Cr* [16] where only light particles (LP) and intermediate fragments (IMF) contribute. Therefore one may conclude that for light compound nuclear systems where only LPs or IMFs contribute, decay barrier height decreases with increase in ℓ-values and reverse behavior is seen in case of heavy nuclear systems having fission or both ER and fission as prominent decay channels. Fig. 5.5 clearly depicts that the decay barrier height is independent of entrance channel as well as

angular momentum for $^{204}Po^{*}$ nucleus.

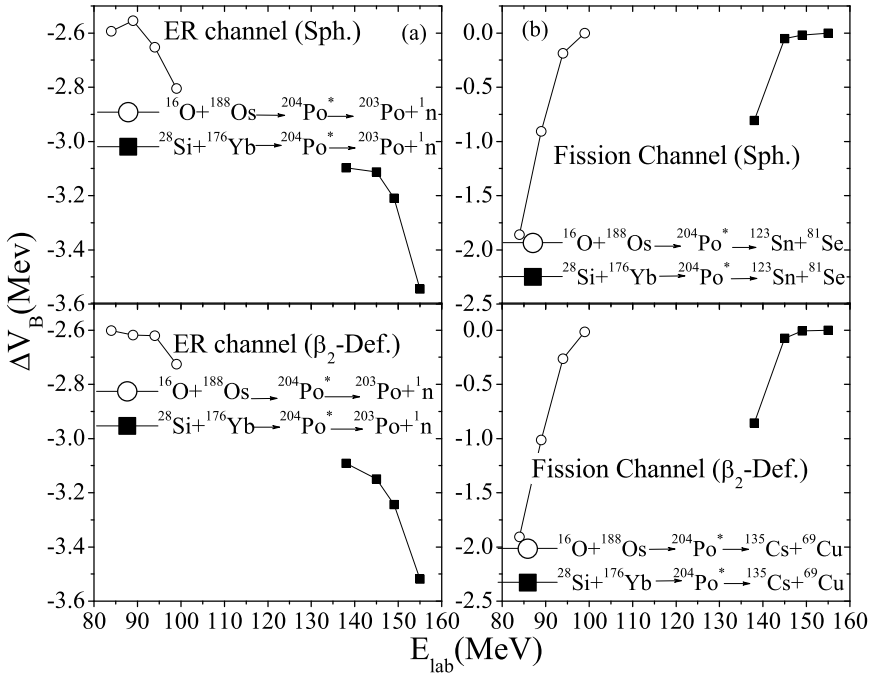

Figure 5.6 The barrier lowering parameter '$\triangle V_B$' as a function of E_{lab} for the decay of $^{204}Po^{*}$ to ^{135}Cs $+^{69}Cu$ and ^{123}Sn $+^{81}Se$ respectively for deformed and spherical choice of fragmentation for fission and to ^{203}Po $+^{1}n$ for ER.

An important aspect of DCM is its inbuilt property of barrier lowering at near and sub barrier energies [20,21]. Fig. 5.6 shows the barrier lowering parameter ΔV_B as a function of E_{lab} for the decay of $^{204}Po^{*}$, to most probable fission fragments ^{135}Cs + ^{69}Cu and ^{123}Sn + ^{81}Se respectively for deformed and spherical choice of fragmentation for fission and to ^{203}Po + ^{1}n for ER. It can be seen from Fig. 5.6 (a) and (b) that ΔV_B increases (in magnitude) as E_{lab} increases for the ER case (left panel) for both spherical as well as deformed choices whereas it increases (in magnitude) as E_{lab} decreases for fission case (right panel). Interesting point to be noted in Fig. 5.6 is that ΔV_B is higher for ^{28}Si channel for ER case whereas the same is not true for fission decay. On the other hand it is clear from Fig. 5.7 that ΔV_B increases (in magnitude) with decrease in angular momentum for fission as well as ER for spherical and deformed considerations. This property of lowering of barrier at near barrier energies depends on the corresponding

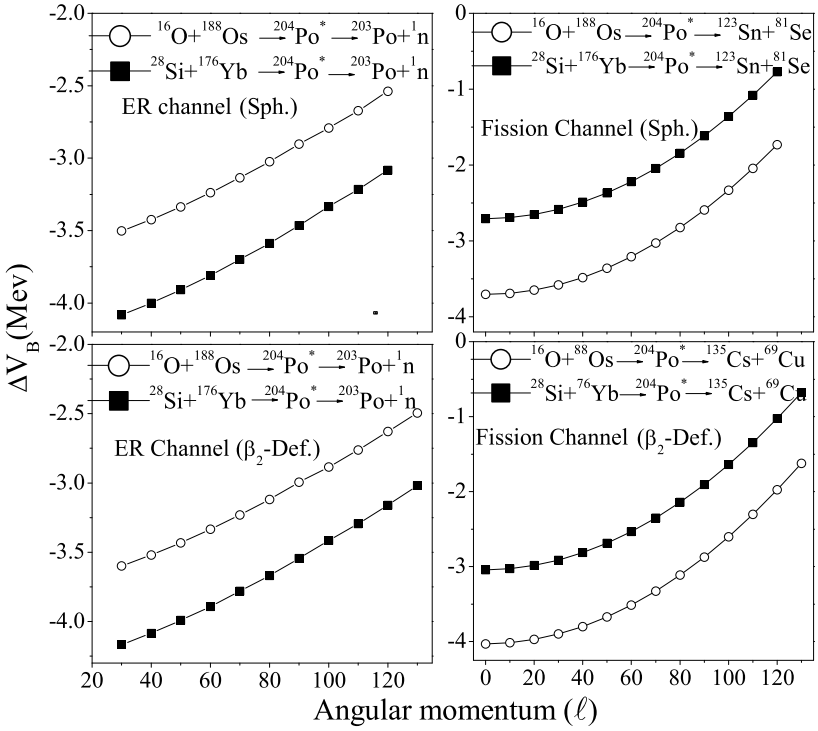

Figure 5.7 Same as that Fig.7, but as a function of angular momentum (ℓ).

values of neck-length parameter (ΔR) used in order to fit the available data [4].

To investigate further, the role of angular momentum in the ER and fission process of ^{204}Po* formed in ^{16}O + ^{188}Os and ^{28}Si +^{176}Yb reactions, the A_i - summed P_0 and P are plotted for the ER (A_2=1-4) and fission fragments (A_2=65-72,75-76,79-86 which contribute towards the fission cross-sections). It can be seen from Fig. 5.8 that at higher ℓ-values, both P_0 and P rise in case of fission process, indicating that the higher angular momentum (ℓ) values contribute more towards the fission of ^{204}Po* as discussed in Figs. 5.1 and 5.2. Although the values of fission-cross sections are summed from ℓ=0 to ℓ_{max}, it is found that even by summing them from ℓ=90 to ℓ_{max}, one gets almost similar values for the fission cross-sections. This implies that lower ℓ-values are not contributing much and angular momentum in window $90 \leq \ell \leq \ell_{max}$ contribute towards fission cross-sections. On the contrary for ER, preformation probability P_0 is large at lower ℓ-values and decreases abruptly near ℓ_{max} value. The penetrability behavior for ER is similar to fission with only

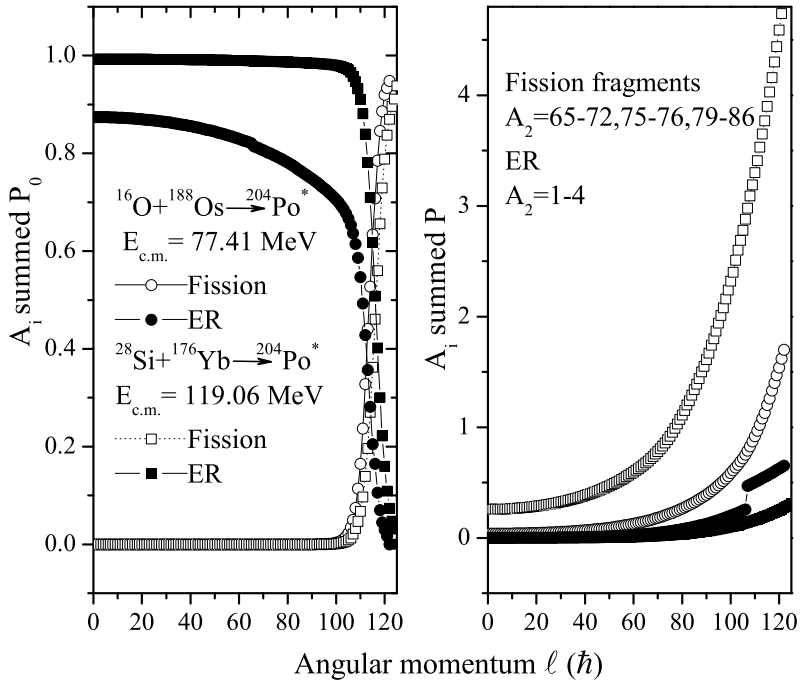

Figure 5.8 The A_i-summed P_0 and P for the fission fragments (A_2=65-72,75-76,79-86) and evaporation residue (A_2=1-4) plotted as a function of angular momentum (ℓ) for the decay of $^{204}Po^{*}$ formed in ^{16}O + ^{188}Os and ^{28}Si +^{176}Yb reaction channels.

difference that magnitude is quite small in case of ER.

The available data [4] consists of fusion cross-sections (calculated by using code CCFUS [5]) and the ER cross-sections (calculated by using code CASCADE [6]) besides experimental data for fission cross-sections in ^{16}O induced channel. Subtracting the ER cross-sections from the fusion cross-sections, the fission cross-section data is obtained. The evaporation residue and the fission cross-sections are fitted in reference to the experimental and available data at various incident energies for the decay of $^{204}Po^{*}$ formed in ^{16}O + ^{188}Os and ^{28}Si +^{176}Yb reaction channels, by fitting the neck-length parameter (ΔR) simultaneously for both ER and fission processes using DCM. The calculations started with the spherical choice were able to fit fission data alone and ER couldn't be fitted with spherical choice of fragmentation. This observation suggested for the possible role of deformations in the decay of $^{204}Po^{*}$ nucleus. Therefore the deformation effects are

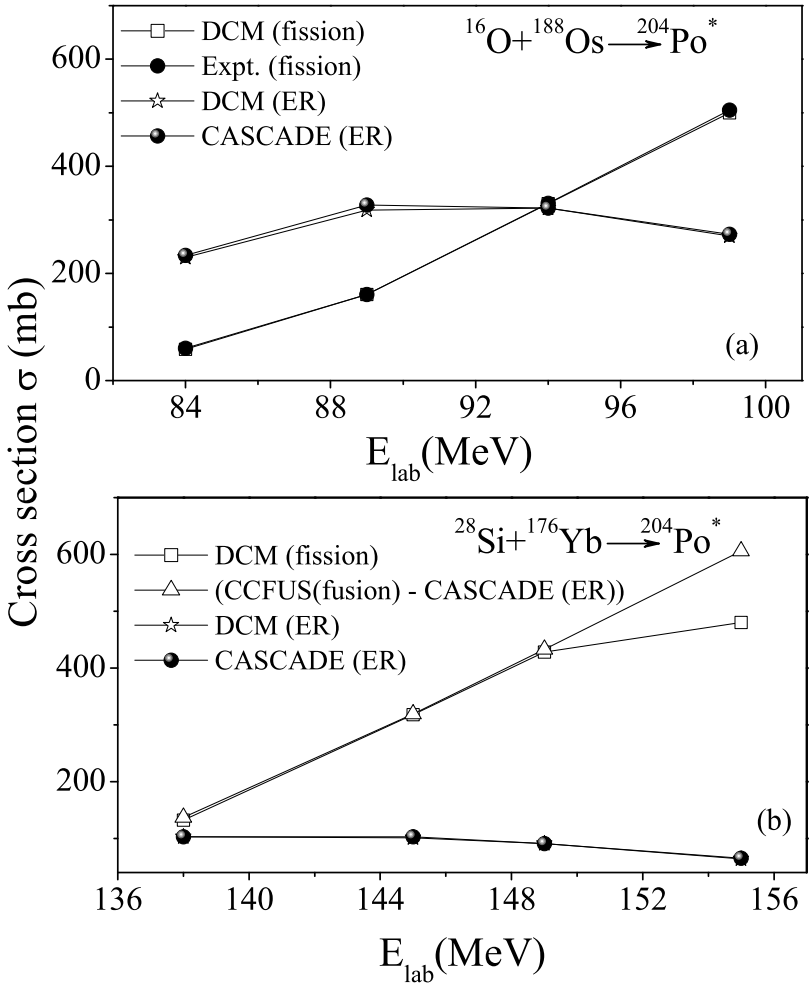

Figure 5.9 The DCM calculated cross-sections compared with the available data [4] for the decay of ^{204}Po* formed in ^{16}O + ^{188}Os and ^{28}Si +^{176}Yb reaction channels at various E_{lab} values.

included and consequently, accounted reasonably well for the available data on fission and ER both.

It can be seen in Fig. 5.9 and Table 5.1 that the calculated evaporation residue (ER) cross-sections and fission cross-sections show excellent agreement with the experimental as well as theoretical available data at all incident energies, except at one highest energy for the channel ^{28}Si +^{176}Yb for fission. This difference at highest energy in case of fission may be because of some amount of non compound nucleus (nCN) contribution for ^{28}Si induced channel. In order to explore this point further the fission fragment anisotropies are calculated in the non sticking limit for moment of inertia (discussed later in section

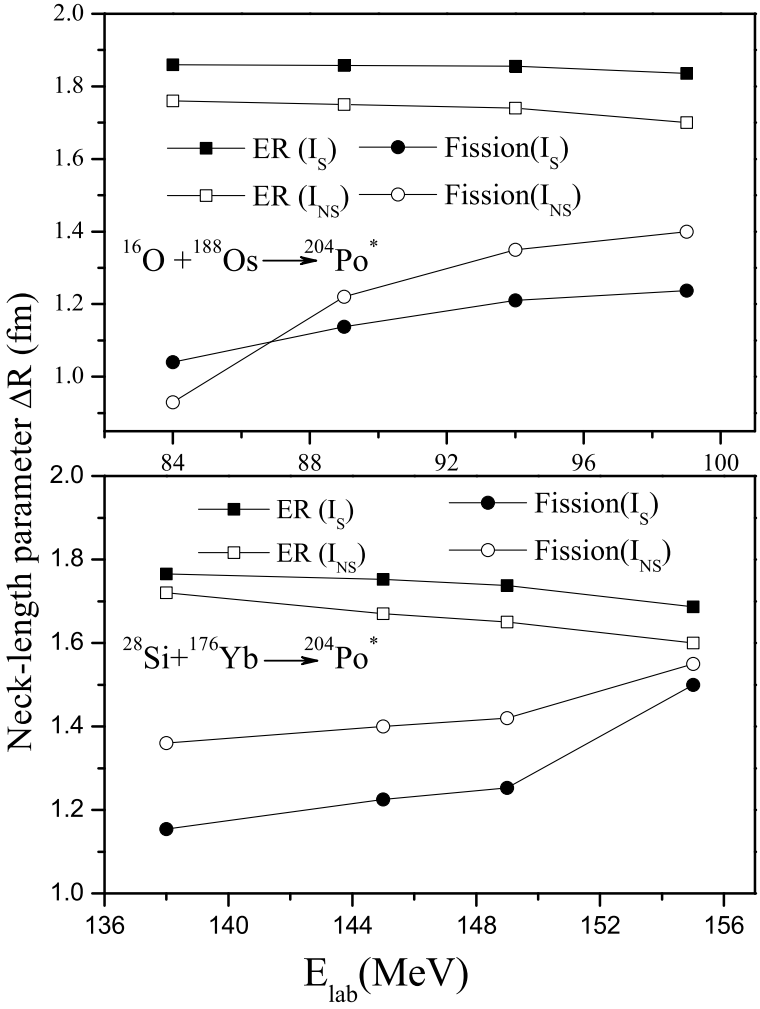

Figure 5.10 The simultaneous fitted neck-length parameter ($\triangle$R) as function of E_{lab} for fission and evaporation residue in the sticking (I_S)and non-sticking (I_{NS}) limit for moment of inertia for the decay of $^{204}Po^{*}$.

5.2.2). The calculations for cross-sections are done for the sticking moment of inertia, as for fitting the cross-sections, the sticking moment of inertia is more appropriate in context of proximity interactions used in calculations of DCM.

Different ΔR values are taken for the fragment mass region of two possible decays ER and fission at each excitation energy (equivalently temperature). This choice clearly means to indicate that the two decay processes ER and fission do not occur simultaneously i.e they occur in different time scales and evolve subject to the nature of dynamics of compound nucleus. Fig. 5.10 shows the variation of neck-length parameter ΔR values

for ER and fission process as a function of E_{lab} for ^{16}O + ^{188}Os and ^{28}Si +^{176}Yb reaction channel for sticking (I_S) and non-sticking (I_{NS}) moment of inertia. It is emphasized again that I_S approach is used to fit cross-sections and I_{NS} is used to account for fission anisotropies. It is clear from Fig. 5.10 that ΔR increases with E_{lab} or center of mass energies for both the channels for fission data however it is almost constant for evaporation residue. The values of ΔR are higher for ER than for fission which simply means that ER process occurs first and fission process follows it in sequence. This observation holds true, independent of sticking or non-sticking moment of inertia approaches.

5.2.2 Fission fragment Anisotropies

The calculations of fission cross-sections shown in Fig. 5.9, indicate the possible presence of non-compound nucleus contribution at one highest energy for the reaction channel ^{28}Si +^{176}Yb. As part of this study, the fission fragment anisotropies are calculated in the non-sticking limit for moment of inertia by using Eq. 2.69 within SSPM approach [22] and DCM based ℓ_{max} for non sticking moment of inertia (I_{NS}). The variation of ΔR values for the non-sticking limit can be seen in Fig. 5.10.

Fig. 5.11 shows the fission fragment anisotropies calculated using DCM based ℓ_{max} value for the non-sticking moment of inertia, within the SSPM approach for the decay of $^{204}Po^*$ formed in ^{16}O + ^{188}Os and ^{28}Si +^{176}Yb reaction channels at various $E_{c.m.}/V_c$ values. The calculated fission fragment anisotropies find reasonable comparison with the experimental data. Therefore nothing concrete could be said about the nCN contribution on the basis of fission fragment anisotropies, in agreement with [4]. It may be noted that in calculations of ER and fission cross-sections only β_2-effect within optimum orientation features are included. It will however be interesting to see the possibility of nCN contribution for ^{28}Si induced channel at highest energy with inclusion of higher multipole

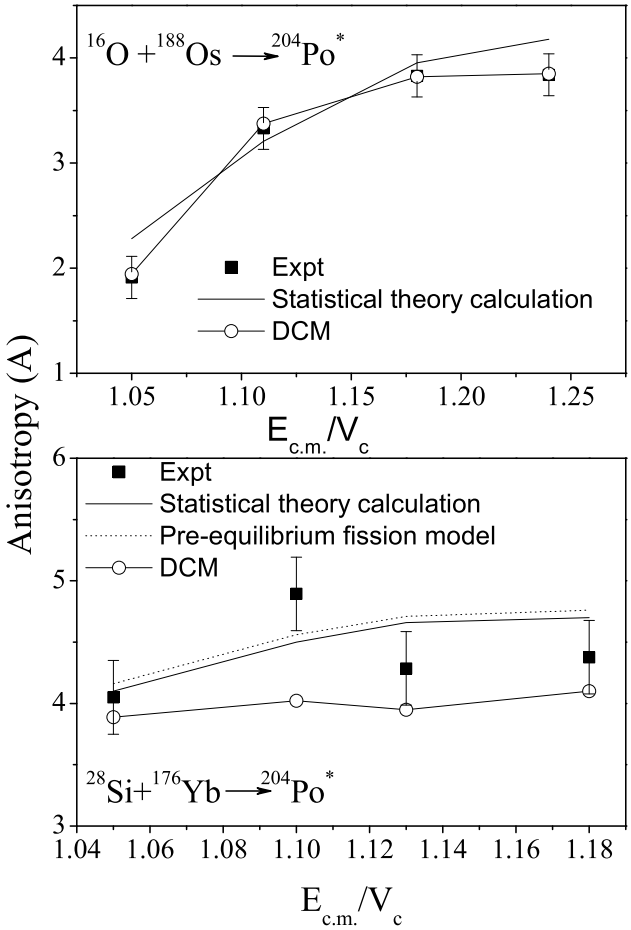

Figure 5.11 The DCM calculated anisotropy compared with experimental, Statistical theory and Pre-equilibrium model calculations for the decay of $^{204}Po^{*}$ formed in ^{16}O + ^{188}Os and ^{28}Si +^{176}Yb reaction channels at various $E_{c.m.}/V_c$ values.

deformation within compact orientation approach [23].

5.2.3 Effect of adding neutrons

The effect of adding two neutrons is seen by studying the decay of $^{204}Po^{*}$ and $^{202}Po^{*}$ formed respectively in ^{16}O + ^{188}Os and ^{16}O + ^{186}Os reaction channels at comparable $E_{c.m.}/V_c$ ($\approx$1.05). The data for $^{204}Po^{*}$ is taken from [4] and for $^{202}Po^{*}$ is taken from [9] and is fitted within DCM. The interesting aspect of this study is that the ℓ_{max} value for β_2-deformed choice of fragmentation is same i.e ℓ_{max}=122 $\hbar$ for both $^{202}Po^{*}$ and $^{204}Po^{*}$. It can be seen from Fig. 5.12, which shows the preformation probability (P_0) of $^{202}Po^{*}$ and $^{204}Po^{*}$ as a

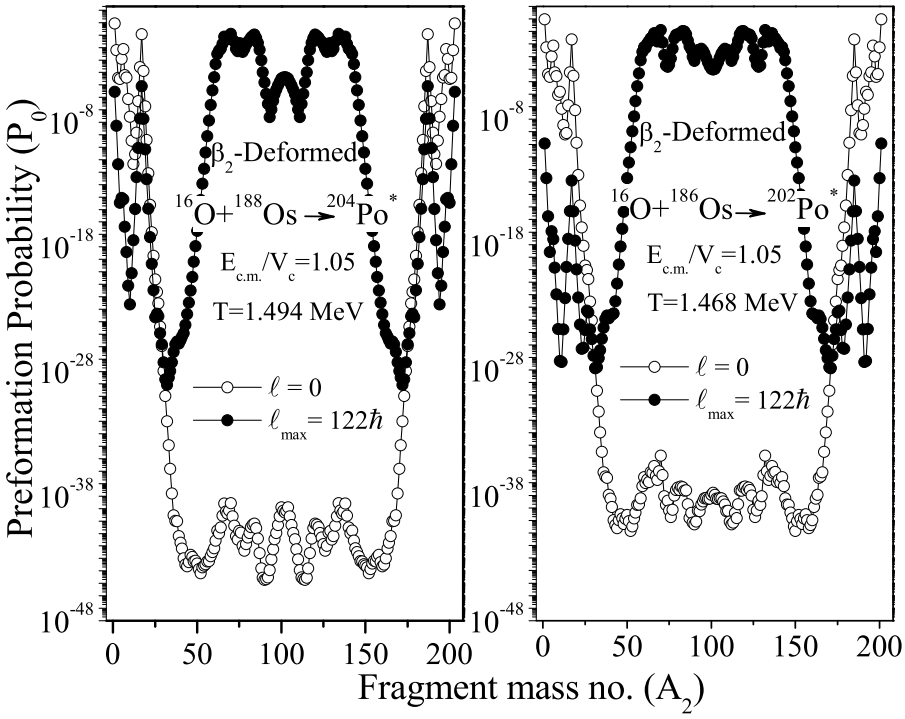

Figure 5.12 Preformation probability as a function of fragment mass number (A_2) for the decay of ^{204}Po* and ^{202}Po* formed in ^{16}O + ^{188}Os and ^{16}O + ^{186}Os reaction channels respectively at comparable $E_{c.m.}/V_c$ value.

function of fragment mass number (A_2), that though the ℓ_{max} value is same for ^{202}Po* and ^{204}Po* but the structure of preformation probability changes significantly particularly in fissioning region. This implies that the addition of two neutrons lead to change in the structure of preformation probability however the contributing fragments towards fission remains similar. This change of fission fragment distribution with addition of two neutrons account for the isospin and sub structure effects in the decay of Po isotopes.

5.3 Summary

The decay of compound nucleus ^{204}Po* formed via two different reaction channels ^{16}O + ^{188}Os and ^{28}Si +^{176}Yb having different mass asymmetry is studied in this chapter. The available data for evaporation residue and fission is fitted simultaneously by choosing

appropriate neck length parameter (ΔR). The spherical choice of fragmentation couldn't fit the ER data therefore the β_2-deformation effects were included in calculations. With the deformed choice, the calculated evaporation residue cross-sections and fission cross-sections find excellent agreement with the available data at all incident center of mass energies, except at one highest energy for the channel ^{28}Si +^{176}Yb in case of fission process. This indicates the presence of some amount of nCN contribution at this energy. However the fission fragment anisotropies calculated within SSPM approach using DCM based ℓ_{max} values for the non sticking moment of inertia, show reasonable comparison with the experimental data. Also the effect of adding two neutrons is seen, by studying the decay of ^{202,204}Po* at comparable $E_{c.m.}/V_c$ value in ^{16}O induced reactions. The modification in preformation probability with addition of two neutrons impart important information regarding sub structure of fission fragments in decay of Po isotopes. Also, in addition to ℓ-independence, the decay barrier heights show entrance channel independence for the heavy nuclear system ^{204}Po* formed in ^{16}O and ^{28}Si induced reactions. The higher values of $\triangle$R for evaporation residue (ER) mean that evaporation residue process occurs, before the fission process takes off. The fission fragment distribution changes from symmetric to asymmetric with inclusion of β_2-deformation effects, asymmetric peak imparting dominant contribution towards fission cross-sections.

Bibliography

[1] M. Kaur and M. K. Sharma, Phys. Rev. C **85**, 054605 (2012).

[2] W. U. Schröder and J. R. Huizenga, in *Damped nuclear reactions, Treatise on Heavy-ion Science*, edited by D. A. Bromley (Plenum Press, New York, 1984), Vol. **II**, p. 115.

[3] K. U. L. Businaro and S. Gallone, Nuovo Cimento **5**, 315 (1957); K. T. R. Davies and A. J. Sierk, Phys. Rev. C **31**, 915 (1985).

[4] R. Tripathi, K. Sudarshan, S. K. Sharma, K. Ramachandran, A. V. R. Reddy, P. K. Pujari, and A. Goswami, Phys. Rev. C **79**, 064607 (2009).

[5] C. H. Dasso and S. Landowne, Comput. Phys. Commun. **46**, 187 (1987).

[6] F. Puhlhofer, Nucl. Phys. A **280**, 267 (1977).

[7] V. S. Ramamurthy and S. S. Kapoor, Phys. Rev.Lett. **54**, 178 (1985).

[8] V. S. Ramamurthy, S. S. Kapoor, R. K. Choudhury, A. Saxena, D. M. Nadkarni, A. K. Mohanty, B. K. Nayak, S. V. Sastry, S. Kailas, A. Chatterjee, P. Singh and A. Navin, Phys. Rev. Lett. **65**, 25 (1990).

[9] R. Rafiei, R. G. Thomas, D. J. Hinde, M. Dasgupta, C. R. Morton, L. R. Gasques, M. L. Brown, and M. D. Rodriquez, Phys. Rev. C **77**, 024606 (2008).

[10] R. K. Gupta, M. Balasubramaniam, R. Kumar, D. Singh, S. K. Arun and W. Greiner, J. Phys. G: Nucl. Part. Phys. **32**, 345 (2006).

[11] S. S. Malik and R. K. Gupta, Phys. Rev. C **39**, 1992 (1989).

[12] R. K. Gupta, S. K. Arun, R. Kumar and Niyti, Int. Rev. Phys. (IREPHY) **2**, 369 (2008).

[13] R. K. Gupta, M. Balasubramaniam, R. Kumar, N. Singh, M. Manhas and W. Greiner, J. Phys.G : Nucl. Part. Phys. **31**, 631 (2005).

[14] B. B. Singh, M. K. Sharma and R. K. Gupta, Phys. Rev. C **77**, 054613 (2008).

[15] Niyti, R. K. Gupta and W. Greiner, J. Phys. G: Nucl. Part. Phys. **37**, 115103 (2010). R. K. Gupta, Niyti, M. Manhas and W. Greiner, J. Phys. G: Nucl. Part. Phys. **36**, 115105 (2009) .

[16] B. B. Singh, M. K. Sharma, R. K. Gupta and W. Greiner, Int. J. Mod. Phys E **15**, 699 (2006).

[17] M. Balasubramaniam, R. Kumar, R. K. Gupta, C. Beck and W. Scheid, J. Phys. G : Nucl. Part. Phys. **29**, 2703 (2003).

[18] M. K. Sharma, G. Sawhney, R. K. Gupta and W. Greiner, J. Phys. G: Nucl. Part. Phys. **38**, 105101 (2011). M. K. Sharma, G. Sawhney, S. Kanwar and R. K. Gupta, Modern Physics letters A **25**, 2022 (2010).

[19] M. Kaur, R. Kumar and M. K. Sharma, Phys. Rev. C **85**, 014609 (2012).

[20] M. K. Sharma, S. Kanwar, G. Sawhney, R. K. Gupta and W. Greiner, J. Phys. G: Nucl. Part. Phys. **38**, 055104 (2011); D. Jain, R. Kumar, M. K. Sharma and R. K. Gupta, Phys. Rev. C **85**, 024615 (2012).

[21] S. K. Arun, R. Kumar and R. K. Gupta, J. Phys. G: Nucl. Part. Phys. **36**, 085105 (2009).

[22] R. Vandenbosch and J. R. Huizenga Nuclear Fission (New York: Academic) (1973).

[23] R. K. Gupta, M. Manhas and W. Greiner, Phys. Rev. C **73**, 054307 (2006).

Chapter 6

Decay of Ba isotopes formed in Kr induced reactions

In the previous chapter, the decay of ^{204}Po* was studied using DCM. The calculations were made by simultaneously fitting the ER and fission cross sections by choosing appropriate neck length parameter. The role of angular momentum, presence of nCN component etc. were analyzed. In addition to these features, in this chapter, the study of medium mass nuclear systems ^{118,122}Ba* formed in ^{78,82}Kr induced reactions is made where the neck length is fitted simultaneously for different mass regions (evaporation residue (ER), intermediate mass fragments (IMF), heavy mass fragments (HMF), and fission), since the different mass regions are seen to behave differently. It is relevant to mention here that so far in this thesis, the ER, fission, quasi fission etc. are addressed whereas the present work also involves the individual fragment cross sections. In other words, the data for the whole charge spectrum is available for the chosen reactions. Using DCM, the decay of ^{118,122}Ba* is investigated in reference to [1]. It is important to note here that so far the proximity potential V_P of Blocki et. al. [2,3] is used whereas here the effect of different versions of proximity potential [4]- [6] and level density is worked out and finally the presence of nCN

component is advocated. This work is published in [7]. In the following, some general features relevant to this work are discussed and the details of the calculations are given in the subsequent sections.

6.1 Introduction

Compound nuclei formed in low energy (E<15 MeV/nucleon) heavy ion reactions are highly excited and carry large angular momenta. The compound system so formed decays by emitting multiple light particles (n,p,α) and γ rays, giving rise to evaporation residue (ER) cross-sections and is accompanied by the so called intermediate mass fragments (IMF) and the near symmetric and symmetric fission component. Different mass regions of compound nuclei show different combinations of these three processes (ER, IMF and fission fragments (FF)) or any one of them as a dominant mode. The regime of warm medium mass (A$\sim$100-130) compound nuclei formed in fusion reactions at above mentioned energy range have been of much interest from time to time. The intermediate mass fragments emitted from excited compound system ^{116}Ba* were observed at medium [8, 9] and high [10, 11] energies. The measured σ_{IMFs} for ^{116}Ba* decay were studied by Gupta and collaborators using the dynamical cluster decay model (DCM) [12].

Recently the GANIL experiment, was performed at a lower energy of 5.5 MeV/nucleon for ^{78,82}Kr incident on ^{40}Ca target ($E_{c.m.}$= 145.42 and 147.87 MeV respectively). This experiment is important as it opens the possibility to account for N/Z dependence of decay fragments. Also the availability of IMF cross-sections is extremely useful in order to understand the complete dynamics of a nuclear reaction particularly in this mass region.

In this work, the data of the GANIL experiment [1] for ^{118,122}Ba* is studied using the DCM [13]- [22] approach and the role of level density parameter and different nuclear

proximity potentials are explored in the process. Earlier Gupta and collaborators studied the preliminary data of the same experiment for ^{118,122}Ba* [23] using DCM and were able to account for the IMFs, the heavy mass fragments (HMFs) and fission except for a small narrow region of HMFs [24]. The experimental ER cross-sections are now available for the ^{78}Kr + ^{40}Ca and ^{82}Kr+^{40}Ca reactions which were otherwise missing in the preliminary data. Moreover the contribution of Z=3,4,5 fragments is available in the final data [1] contrary to the preliminary data [23]. The interesting result is that the fission as well as ER cross-sections given in the final data is having larger value for ^{78}Kr + ^{40}Ca channel i.e. the neutron deficient one. The individual fission fragment cross-section data is also available for the fragments with atomic no. 3<Z<28. The ratio $\sigma_{^{118}Ba}/\sigma_{^{122}Ba}$ is >1 for majority of IMF, HMF and fission fragments. The preliminary data for the individual fission fragment cross-section was lower in magnitude by a factor of 3-4 (i.e the newer data is having values approximately 3 to 4 times that of preliminary data). Also the authors of [1] analyzed the ^{118,122}Ba* data by using the statistical models, the BUSCO, GEMINI codes and the DNS model. In BUSCO code [11], the Hauser-Feshbach has been extended to the IMF emission in their ground state as well as excited state and used the value of level density parameter a=A/8.5. The GEMINI code [25] combines Hauser-Feshbach and transition state formalisms to describe the disintegration of hot compound nucleus by emission of products spanning the whole mass (charge) range from neutron to the fragment corresponding to the symmetric fission. The level density parameter is taken as a=A/8. The DNS model takes into account the decay of initial compound nucleus and collisional stage preceding the compound nucleus formation along with the competing quasi fission phenomena. The level density parameter is used as a=A/6.8. The maximum angular momentum ℓ_{max}, instead of being given by the measured fusion cross-section was considered as the free parameter to be fitted to yield around the symmetric splitting for

statistical models. However in the DNS model, the largest value of angular momentum is taken as the critical value. GEMINI and BUSCO codes reproduce the Z distribution of the measured cross-sections in parts [1] and a better global agreement was reported within the DNS framework. In view of the earlier work on ^{116}Ba* [12] and preliminary work of ^{118,122}Ba* [24], the decay of ^{118,122}Ba* compound nuclei is investigated in view of latest data [1] and the role of level density parameter, proximity potentials, pairing strength and N/Z dependence is investigated.

The organization of chapter is as follows: The DCM calculated cross sections and results are presented in sec. 6.2 and the summary of results is given in sec. 6.3

6.2 Calculations

Here in section 6.2.1, the calculations and observations regarding the decay of ^{118,122}Ba* formed in ^{78,82}Kr + ^{40}Ca reactions are discussed respectively at $E_{c.m.}$=145.42 MeV and 147.87 MeV. The ER cross-sections and the total fission cross-sections are fitted and the role of deformations is duly investigated. The fragmentation potential and preformation probability are looked into for the related nuclear structure effects. Then in section 6.2.2, the individual fragment cross-sections are addressed, and the effect of the level density parameter, non-zero pairing strength and that of different versions of proximity potentials is analyzed. The non-compound nucleus contribution is also predicted for the unfitted valley. Finally in section 6.2.3, the N/Z dependence in the decay of Ba isotopes is explored.

Table 6.1 Evaporation residue cross-section (σ_{ER}) and fission cross-section ($\sigma_{fission}$) calculated using DCM for spherical case, are compared with the experimental data, GEMINI and DNS calculations.

	^{78}Kr + ^{40}Ca		^{82}Kr + ^{40}Ca	
	σ_{ER}(mb)	$\sigma_{fission}$ (mb)	σ_{ER}(mb)	$\sigma_{fission}$ (mb)
DCM	538	447(318+129*)	491	331.2(296+35.2*)
Expt	539±100	447±46	492±90	332±35
GEMINI	237	600	285	547
DNS	601	349	638	208

* refers to quasi fission component.

6.2.1 Evaporation residue (ER) and total fission cross-sections

The available data for total fission and ER cross-sections have been fitted simultaneously by adjusting the neck length parameter ($\triangle$R) of the dynamical cluster decay model within spherical fragmentation approach. The $\triangle$R is the only parameter of the model and controls the barrier lowering parameter $\triangle V_B$. The $\triangle$R values used to fit the available data are 1.587 fm and 1.600 fm respectively for ER and fission part of ^{118}Ba* and 1.539 fm and 1.580 fm respectively for ER and fission of ^{122}Ba*. In agreement with experimental predictions, some quasi fission (qf) contribution is also observed in available fission data. The qf component seem to be dominant $\approx$ 28% for neutron deficient ^{78}Kr + ^{40}Ca reaction as compared to ^{82}Kr + ^{40}Ca reaction where its contribution is $\approx$ 10%. The data of GEMINI and DNS code is also available for the ER and fission part, where the GEMINI code is overestimating the fission data and underestimating the ER data, the DNS code is overestimating the ER data and underestimating the fission data. However within DCM approach (as clear from Table 6.1) the ER and the fission part are accounted nicely by taking the spherical choice of fragmentation. It may be noted that ER is nicely fitted within DCM approach, the fission component calls for additional quasi fission contribution and the ($\sigma_{fission}$+σ_{qf}) together fit the available fission data. Interestingly, if one takes

the deformed choice of fragmentation, DCM fits the ER cross-sections but not the fission cross-sections data. This implies that the role of deformation is explicitly present in the

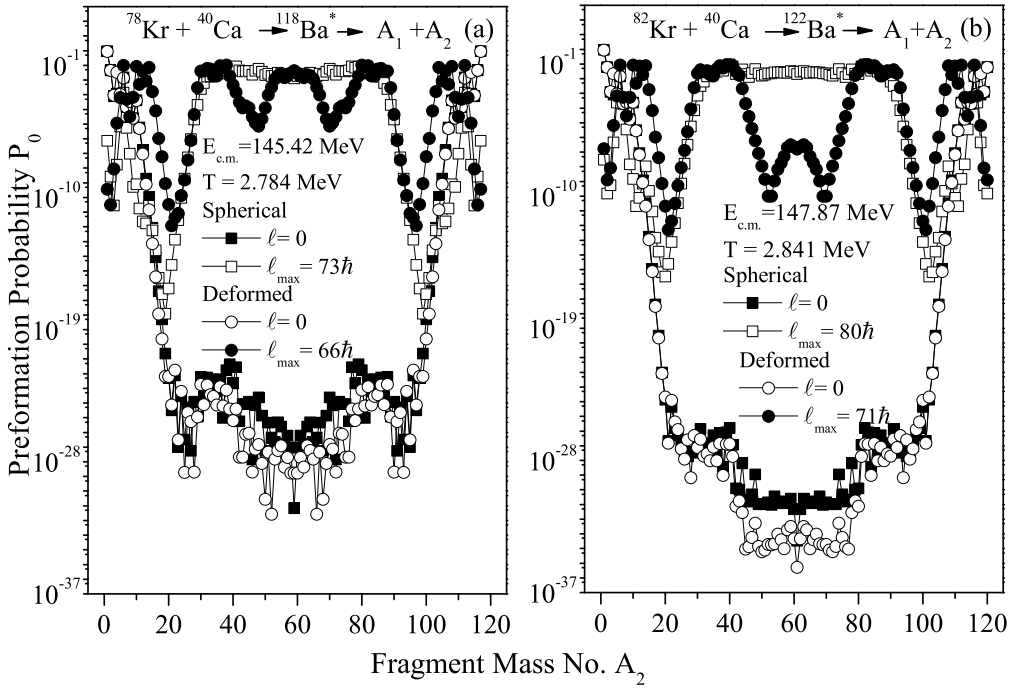

Figure 6.1 (a) and (b) shows the preformation probability P_0 as a function of fragment mass number A_2 for the compound system ^{118,122}Ba* respectively at $E_{c.m.}$=145.42 and 147.87 MeV (equivalently T=2.784 and 2.841 MeV) for spherical as well as deformed case.

ER part, for both the compound systems ^{118,122}Ba*. Fig. 6.1 shows the preformation probability P_0 as a function of fragment mass A_2 at extreme ℓ values for spherical and deformed choices of fragmentation for ^{118,122}Ba*. It is clear from the Fig. 6.1 that at lower ℓ value (i.e ℓ=0) the behavior is similar for the spherical as well as the deformed case however at $\ell=\ell_{max}$, there seems a humped structure for the deformed choice and symmetric distribution for the spherical i.e a single window is formed for the spherical case whereas multiple windows are to be considered for the deformed case. Interestingly, the symmetric fragments seem to be operating for ^{118}Ba* whereas the same are completely out of picture within β_2-deformed fragmentation approach. In other words N/Z seem to be operating within β_2-deformed approach but at the same time fission data couldn't

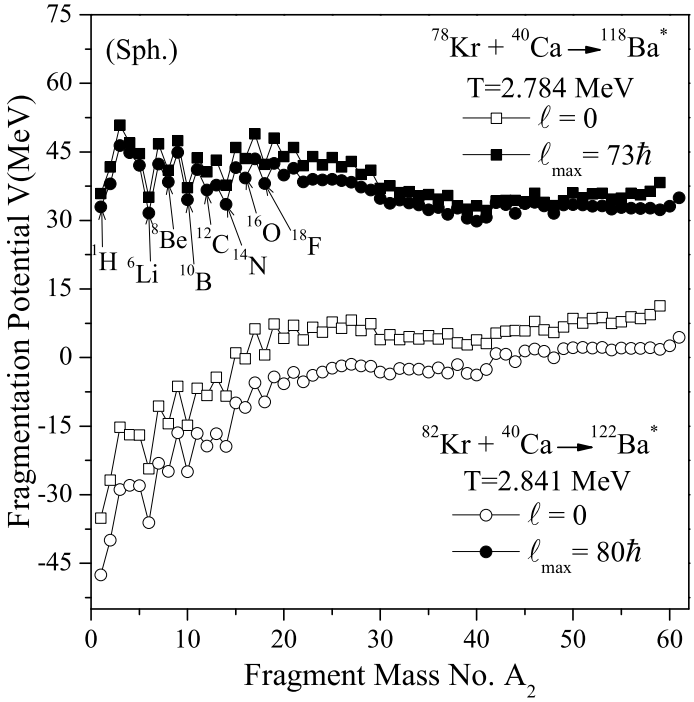

Figure 6.2 Fragmentation Potential as a function of fragment mass number A_2 for the compound system ^{118,122}Ba* at E$_{c.m.}$=145.42 and 147.87 MeV (equivalently T=2.784 and 2.841 MeV) respectively at extreme ℓ values.

be fitted so nothing concrete can be said at this point regarding the N/Z dependence of decaying fragments. However N/Z dependence of Ba isotopes is independently worked out later in section 6.2.3. Fig. 6.2 shows the mass fragmentation potentials $V(A_i)$ calculated at extreme ℓ-values (i.e ℓ=0 and ℓ=ℓ_{max}) for ^{118,122}Ba* respectively at fixed $E_{c.m.}$= 145.42 and 147.87 MeV (equivalently at T=2.784 and 2.841 MeV). One may notice an interesting α-nucleus structure for different mass regions i.e different mass regions behave differently. At ℓ=0, the light fragments production is dominant whereas the trend gets reversed with the inclusion of angular momentum effects and IMFs and fission starts competing with light fragments. Interestingly, the α-nucleus structure in HMF region start vanishing for neutron rich ^{122}Ba*. This aspect is further exploited in Fig. 6.10 to establish the N/Z dependence of Ba isotopes formed in Kr induced reactions.

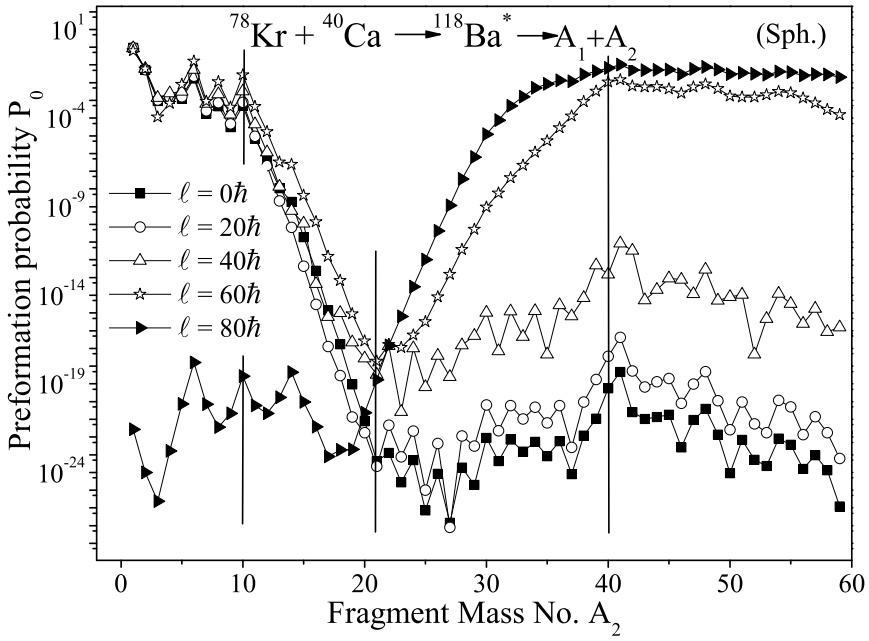

Figure 6.3 Preformation probability (P_0) as a function of fragment mass number A_2 for different ℓ values, calculated for the compound system $^{118}Ba^*$ at $E_{c.m.}$=145.42 MeV (equivalently T=2.784 MeV) for the spherical case.

6.2.2 Individual fragment cross-sections for the charge region 3<Z<28

The calculations are initiated by taking same neck-length parameter ($\triangle$R) values as used initially to calculate the ER and fission cross-sections, but it is observed in Fig. 6.3 that different mass regions are behaving differently, so different $\triangle$R values for different mass regions are used in order to fit the fragment cross-section data. It can be seen from the Fig. 6.3, which shows the preformation probability at various ℓ-values for the compound system $^{118}Ba^*$, that the LPs, the intermediate mass fragments (denoted as IMFs), the heavy mass fragments (HMFs), near symmetric fission (nSF) and symmetric fission (SF) fragments show different characteristic behavior. The use of different $\triangle$R values simply means that they are occurring at different time scales. This prediction of different $\triangle$R values for fragment mass region is also made in the earlier calculation for $^{56}Ni^*$ compound system [26] and the preliminary work for $^{118,122}Ba^*$ [24]. The parameter $\triangle$R, taken to

be the same for all ℓ values, is fixed for penetrability, P→1 in present calculations at $\ell=\ell_{max}$. Using the △R (ℓ_{max}) values as 1.32(106), 1.39(90), 1.29(100), 1.0(123) for mass regions, namely 1-10, 11-22, 23-39, 40-59 for ^{118}Ba* and 1.25(111), 1.35(98), 1.29(105), 1.19(116) for mass regions 1-14, 15-22, 23-36, 37-61 for ^{122}Ba*, the mass fragmentation potentials are calculated. Fig. 6.4 shows the cross-sections calculated for both the

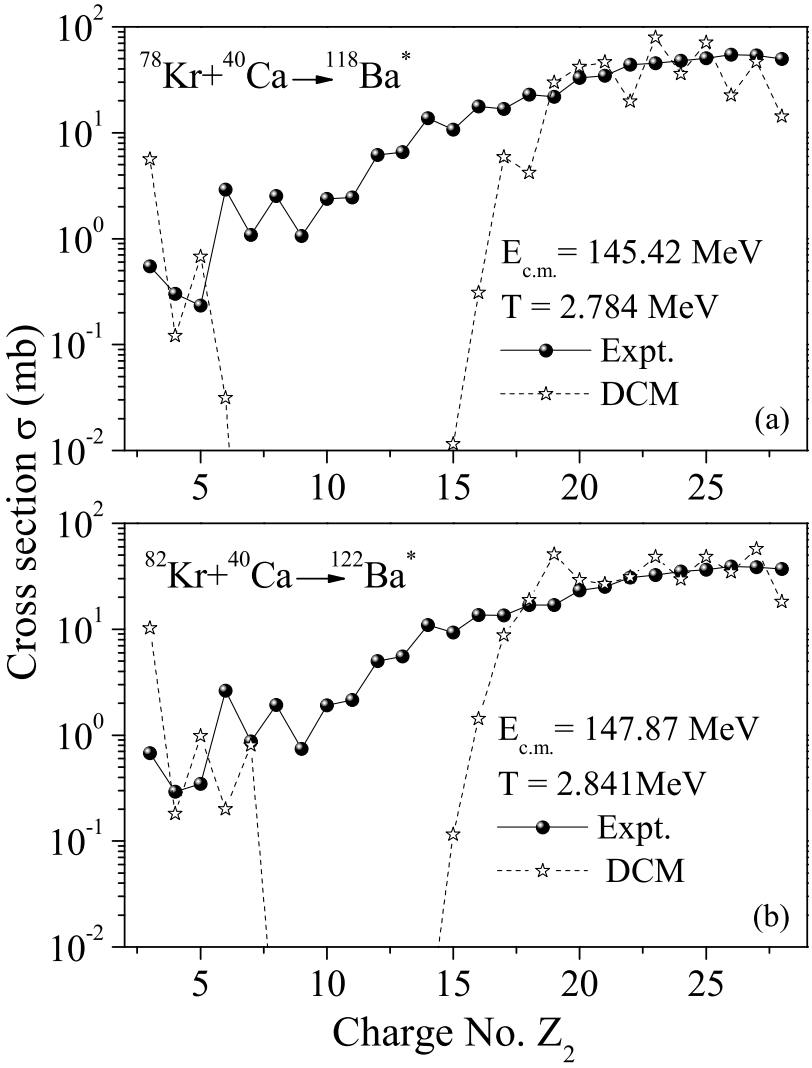

Figure 6.4 (a) and (b) shows the comparison of DCM based fragment cross-sections with the experimentally available data as a function of the charge Z_2 of the light fragment for the ^{118,122}Ba* compound systems.

compound systems ^{118,122}Ba* and are also compared with the experimental data [1]. As only the charges of fragments are measured in experiments, the calculated yields for each charge are summed over the energetically favored masses of the fragments. The cross-

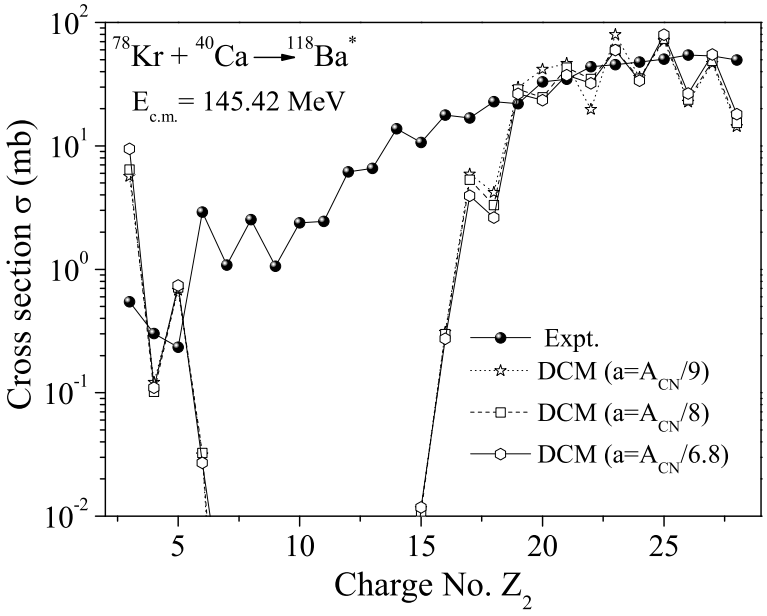

Figure 6.5 The variation of the individual fragment cross-section for different values of level density parameter compared with the experimental data as a function of the charge Z_2 of the light fragment for the $^{118}Ba^*$ decay at incident laboratory energy 5.5 MeV/nucleon.

sections are peaked at Z_2(contributing masses)= 23(46, 47, 48) and 25(51, 52, 53, 54) for $^{118}Ba^*$ and at Z_2(contributing masses)= 19(39, 40), 23(48, 49, 50), 27(58, 59, 60) for $^{122}Ba^*$. The most probable Z_2 for the light fragments in DCM calculations is ^1H. The level density parameter 'a' used here is A/9. The level density parameter is related to the $E_{C.N.}$ (see Eq. 2.16). Fig. 6.4 shows that the DCM results are reasonable for the lower end of light IMFs and upper end of heavy mass fragments, nSF and SF data but DCM underestimates the data for the fragment mass region ($6 \leq Z \leq 18$). It is relevant to mention here that the BUSCO code fits only the light IMFs data and GEMINI code fits the HMFs, nSF and SF data [1] with the value of level density parameter 'a' taken as A/8.5 and A/8 respectively whereas DNS model, with a=A/6.8, gives reasonably better description with some underestimation of the magnitude by a factor of 2-3. As BUSCO, GEMINI and DNS codes have used different values of the level density parameter so the effect of the level density parameter 'a' is also studied within DCM. Fig. 6.5. shows the

variation of the fragment cross-section with charge number Z_2 for different values of level density parameter. As 'a' increases, temperature decreases but it still remains above 2 MeV for all 'a' values considered here, therefore shell effects are not coming into picture and hence no significant change occurs within DCM. As temperature is greater than 2 MeV for both the systems ^{118,122}Ba*, the pairing strength δ=0 (in the liquid drop model) is used here in the DCM calculations. The effect of non zero pairing δ>0 is also seen for the ^{118}Ba*, taking δ (T) in V_{LDM} as a fitting parameter, say to Li data. Fig. 6.6 shows the behavior of zero pairing strength (δ=0) and the role of non zero pairing strength (δ>0), using δ=17.5 MeV, fitted to Li data. For δ=17.5 MeV, the stronger preference for even Z over the odd-Z fragments is noticed.

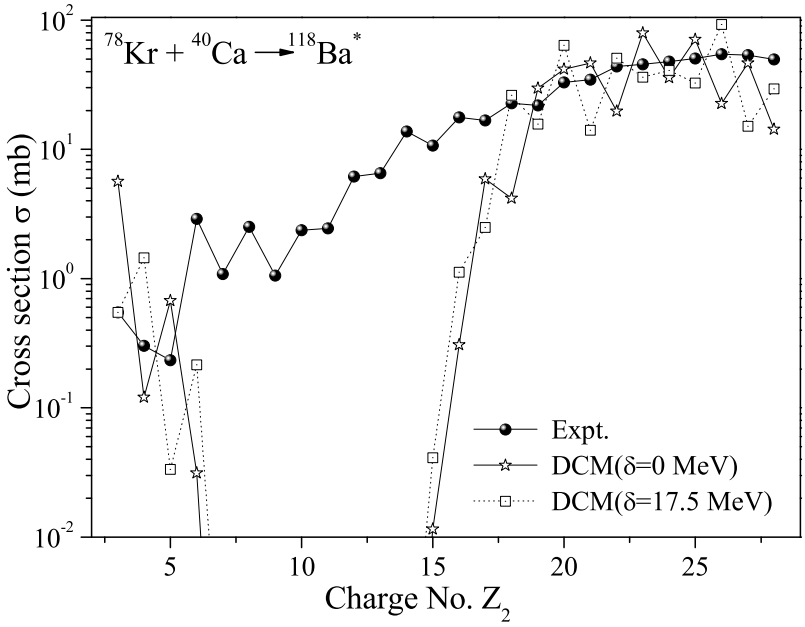

Figure 6.6 The role of non zero pairing strength δ>0 illustrated for ^{118}Ba* using δ=17.5 MeV, fitted to say, Li data. Note that at T values of experiments (T>2 MeV) the pairing strength, δ is zero in the liquid drop potential used here in DCM calculations

As the level density parameter 'a' and pairing strength 'δ' do not improve the fitting in HMF region so in order to fit the heavier mass fragments, different versions of proximity potentials [2–6] are used. These proximity potentials are denoted as, prox77 [2,3], prox88

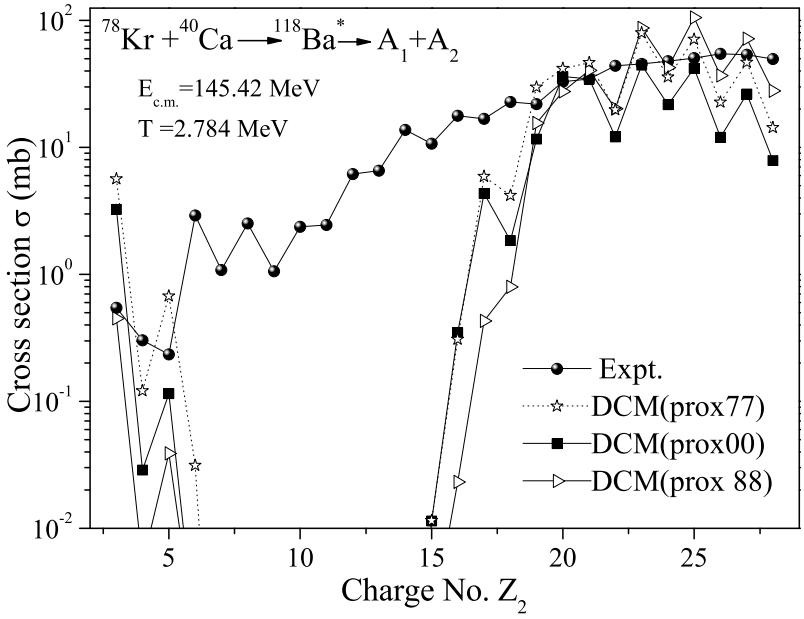

Figure 6.7 The variation of the fragment cross-section for different proximity potentials compared with the experimentally available data as a function of the charge Z_2 of the light fragment for the $^{118}Ba^{*}$ decay at incident laboratory energy 5.5 MeV/nucleon.

[4, 5], prox00 [6]. Fig. 6.7 shows the comparison of fragment cross-section calculated by using different proximity potentials with the available experimental cross-sections. It is clear from Fig. 6.7 that even by using different versions of nuclear proximity potential, the HMF region is not fitted. It is so because the structure of preformation probability remains same even by using different proximity potentials, however there is variation in its magnitude which leads to different ℓ_{max} values. For example by using prox00 in the fragmentation potential, the magnitude of preformation probability increases though the structure remains same but at the same time the ℓ_{max} values decrease so the comparison in HMF region does not improve. Within DCM, as a possible solution to this problem, the non-compound nucleus (nCN) contribution have been calculated for this region ($6 \leq Z \leq 18$) alone, by taking preformation probability, P_0=1 and defining $\sigma_{nCN}=\sigma_{CN}^{Expt}-\sigma_{CN}^{Cal}$ for each fragment. Fig. 6.8 shows the comparison of the DCM calculated compound nucleus plus non-compound nucleus contribution with the experimental cross-sections for $^{118,122}Ba^{*}$

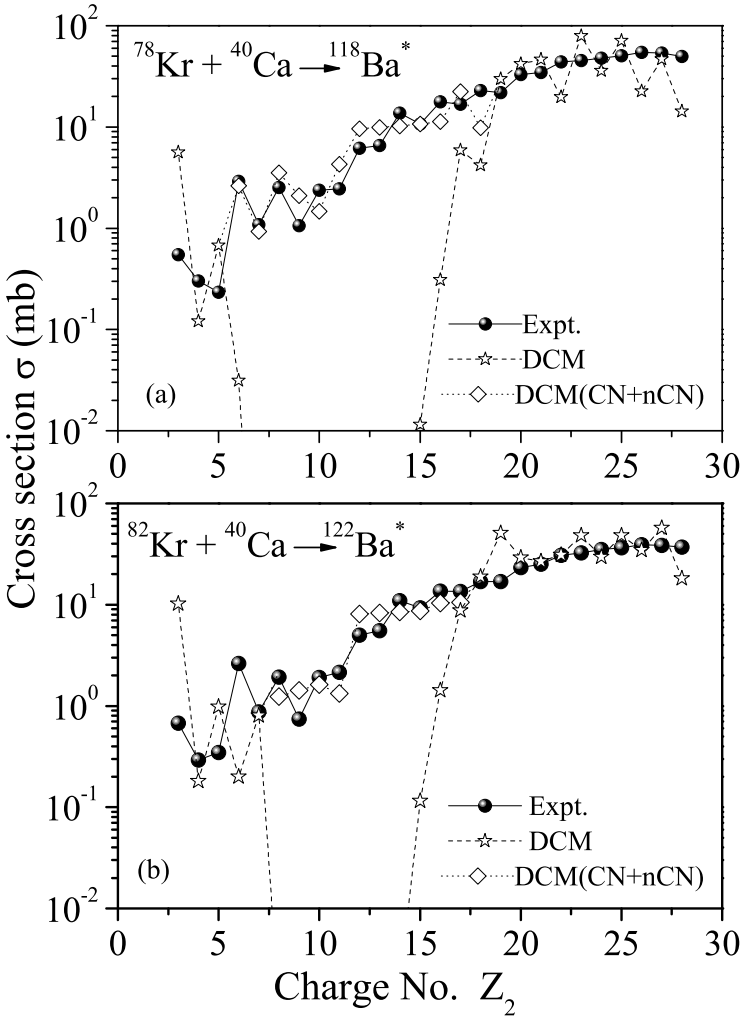

Figure 6.8 (a) and (b) shows the non-compound nucleus contribution calculated within DCM by making preformation probability, P_0=1 only for Z_2=6-18 fragments for ^{118}Ba* and Z_2=8-17 fragments for ^{122}Ba*.

formed in ^{78,82}Kr + ^{40}Ca reactions respectively. For the best fitted ℓ-value at same ΔR values, the valley gets filled and DCM calculated σ_{CN}+σ_{nCN} is in better agreement with the experimental data. The ℓ-values (mass region) taken for the nCN calculations are 34 $\hbar$ (6≤Z≤11) and 56 $\hbar$ (12≤Z≤18) for ^{118}Ba* and 39 $\hbar$ (8≤Z≤11) and 58 $\hbar$ (12≤Z≤17) for ^{122}Ba*. It is relevant to mention here that this nCN contribution supports the prediction of qf in ^{78,82}Kr + ^{40}Ca reactions at 5.5 MeV/nucleon. It may be noted that the experiment [1] as well as the DNS based results also support this additional qf or nCN component in the HMF/fission region.

Table 6.2 Evaporation residue cross-section (σ_{ER}) and fission cross-section ($\sigma_{fission}$) calculated using DCM for isotopes of Ba at the respective ΔR values.

CN	ΔR^{ER} (fm)	$\Delta R^{fission}$ (fm)	σ_{ER} (mb)	$\sigma_{fission}$ (mb)
$^{114}Ba^*$	1.632	1.619	629	322
$^{118}Ba^*$	1.587	1.6	538	318
$^{122}Ba^*$	1.539	1.58	491	296
$^{126}Ba^*$	1.489	1.559	30.6	288

6.2.3 N/Z dependence of decay fragments in Ba isotopes

To study the N/Z dependence, the decay of various isotopes of Ba say ^{114,118,122,126}Ba* is studied at same energy E=5.5 MeV/nucleon. The experimental data for ^{118}Ba* and ^{122}Ba* is available, which is fitted via DCM by adjusting the neck-length parameter (ΔR) simultaneously for ER and fission. In order to predict the ER and fission cross-sections for ^{114}Ba* and ^{126}Ba* (see Table 6.2), the ΔR values of ^{118}Ba* and ^{122}Ba* are extrapolated

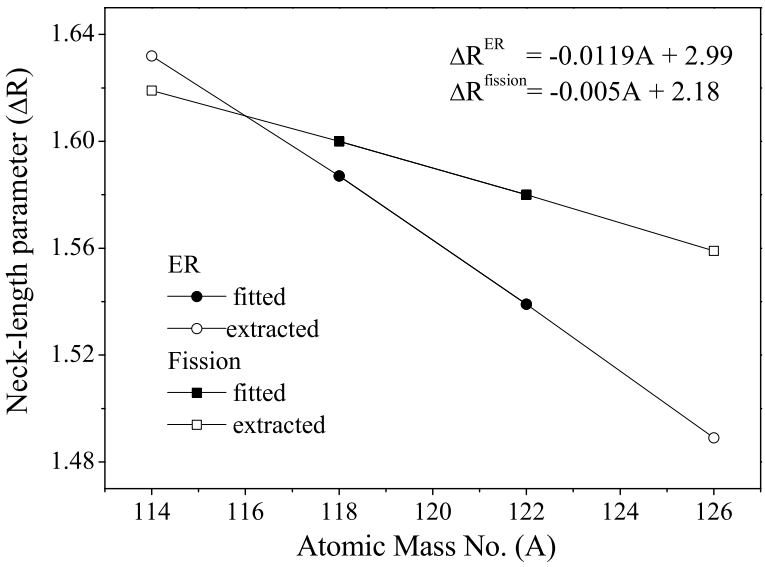

Figure 6.9 Extrapolated neck-length parameter (ΔR) as a function of atomic mass number (A).

using polynomial fitting. Fig. 6.9 shows the extrapolated ΔR values for ER and fission as a function of atomic mass number (A), where the filled symbols represent ΔR for

DCM fitted ^{118,122}Ba* cross-sections and hollow symbols represent extracted ΔR values for ^{114,126}Ba* by using the polynomials,

$$\Delta R^{ER} = -0.0119A + 2.99, \Delta R^{fission} = -0.005A + 2.18$$

fitted for the ΔR values of ^{118,122}Ba*. One can observe from Table 6.2 that the ER as well as the fission cross-sections are enhanced for the neutron deficient nuclei i.e the cross-sections show decreasing trend with increasing N/Z ratio.

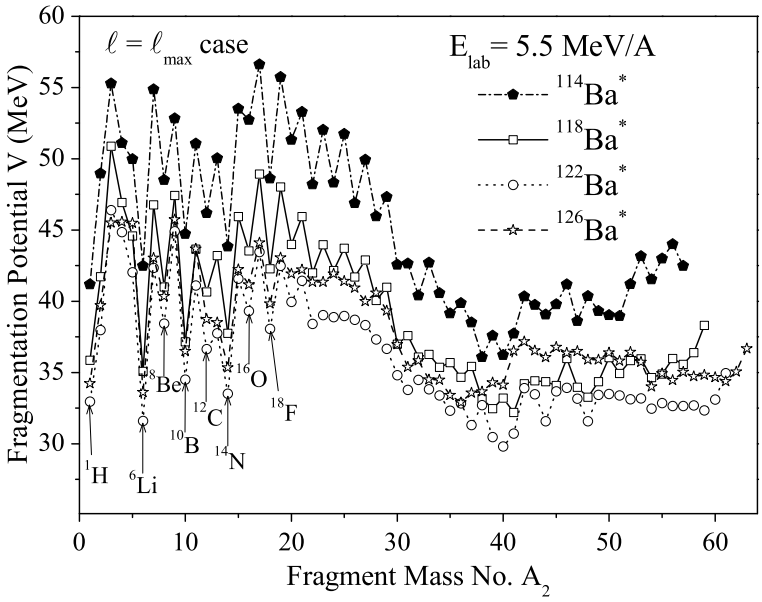

Figure 6.10 Fragmentation Potential as a function of fragment mass number A_2 for the compound systems ^{114,118,122,126}Ba* at E=5.5 MeV/nucleon with respective ℓ_{max} values as 66, 73, 80, 88 $\hbar$.

This behavior of fission cross-sections may be because of strong structure effects as shown in Fig. 6.10 depicting the fragmentation potential as a function of fragment mass number A_2 for various isotopes of Ba. One may see in Fig. 6.10 that α-nucleus structure is prominent for ^{114}Ba and it starts vanishing with addition of every four neutrons. In other words the α-nucleus structure is prominent for ^{114,118}Ba and is almost absent in HMF region for ^{122,126}Ba. It may be noted that this difference in the structure with addition

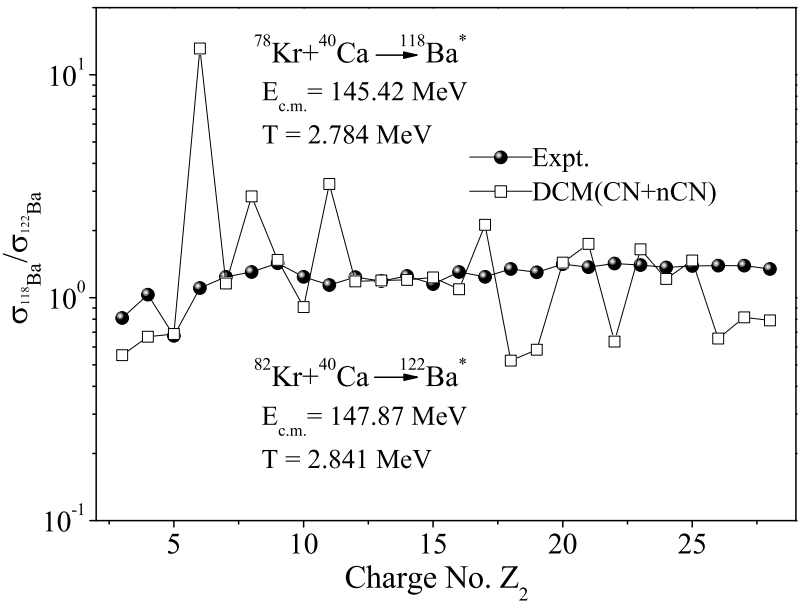

Figure 6.11 The ratio $\sigma_{^{118}Ba}/\sigma_{^{122}Ba}$ as a function of charge number Z_2 for experiment compared with DCM calculated CN+nCN cross-sections.

of neutrons come mainly by shell corrections. It may also be noted that cross-sections of ^{114,126}Ba reported in Table 6.2 are extracted from polynomial fit on the systematics of ΔR used. Hence the fragmentation path for ^{114,126}Ba reported in Fig. 6.10 is plotted only to see the α-nucleus structure of fragments evolved. Fig. 6.11 shows the comparison of ratio $\sigma_{^{118}Ba}/\sigma_{^{122}Ba}$ as a function of charge number Z_2 for the experimental data with the calculated ratio from DCM, which includes contribution due to non-compound nucleus (nCN) in addition to compound nucleus (CN) contribution. The DCM based calculations show enhanced cross-sections for majority of decaying fragments of neutron deficient ^{118}Ba, in agreement with the experimental observation.

6.3 Summary

Summarizing, in this chapter, the decay of ^{118,122}Ba* formed in ^{78,82}Kr+^{40}Ca reactions at a relatively low laboratory energy of 5.5 MeV/nucleon is studied using DCM for the latest available data [1] which is 3 to 4 times greater than the preliminary data [23]. The ER

as well as total fission cross-sections (by incorporating the qf component) is accounted reasonably well within DCM, for the spherical choice of fragmentation. The complete Z-distribution is observed in experiment [1] and the DCM based calculations under-estimate the yields in a narrow window of $6 \leq Z \leq 18$, whereas for the similar mass region the GEMINI code over-estimates the data and the BUSCO code under-predicts strongly beyond IMF region. The DNS model gives relatively better picture with some underestimation of the magnitude by a factor of 2 to 3. In other words, an overall comparison of the data with DCM is better than for both the BUSCO and GEMINI codes, and could perhaps be improved with the inclusion of the secondary emission of light particles from the primary fragments. Since for both reactions the temperature remains above 2 MeV so no significant change is observed in the pattern of potential energy surfaces with different values of level density parameter and pairing strength. As expected, the even Z fragments become relatively favorable with the inclusion of pairing strength. Different versions of proximity potentials are also not able to account for the unfitted valley. Subsequently, the inclusion of non-compound nucleus contribution (nCN) predicted for this unfitted region ($6 \leq Z \leq 18$) bring the DCM results closer to experimental data. The N/Z dependence of decay fragments in the isotopes of Ba is explored, the neutron deficient Ba nuclei are shown to give enhanced ER and fission cross-sections and because of the shell corrections, the α-nucleus structure starts vanishing with increase in N/Z ratio. The prediction of qf and/or nCN contribution reported in this work calls for further verifications.

Bibliography

[1] G. Ademard, J. P. Wieleczko, J. Gomez del Campo, M. La Commara, E. Bonnet, M. Vigilante, A. Chbihi, J. D. Frankland, E. Rosato, G. Spadaccini, Sh. A. Kalandarov, C. Beck, S. Barlini, B. Borderie, R. Bougault, R. Dayras, G. De Angelis, J. De Sanctis, V. L. Kravchuk, P. Lautesse, N. Le Neindre, J. Moisan, A. D'Onofrio, M. Parlog, D. Pierroutsakou, M. F. Rivet, M. Romoli, R. Roy, G. G. Adamian, and N. V. Antonenko, Phys. Rev. C **83**, 054619 (2011).

[2] J. Blocki, J. Randrup, W.J. Swiatecki, and C.F. Tsang, Ann. Phys. (N.Y.) **105**, 427 (1977).

[3] R. K. Gupta, N. Singh and M. Manhas, Phys. Rev. C **70**, 034608 (2004).

[4] P. Moller and J. R. Nix, Nucl. Phys. A **361**, 117(1981).

[5] W. Reisdorf, J. Phys. G: Nucl. Part. Phys. **20**, 1297 (1994).

[6] W. D. Myers and W. J. Swiatecki, Phys. Rev. C **62**, 044610 (2000).

[7] M. Kaur, R. Kumar and M. K. Sharma, Phys. Rev. C **85**, 014609 (2012).

[8] J. Gomez del Campo, C. Baktash, H.-Q. Jin, D. Rudolph, A. D'Onofrio, F. Terrasi, G. de Angelis, M. De Poli, C. Fahlander, A. Gadea, D. R. Napoli, Q. Pan, P. Spolaore, L. De Acuna, D. Bazzacco, S. Lunardi, P.Pavan, C. Rossi-Alvarez, A. Buscemi,

R. Zanon, A. De Rosa, L. Campajola, M. La Commara, G. Inglima, V. Roca, M. Romano, M. Sandoli, M. Romoli, A. Ordine, and D. Pierroutsakou, Phys. Rev. C **57**, R457 (1998).

[9] M. La Commara, J. Gomez del Campo, A. D'Onofrio, A. Gadea, M. Glogowski, P. Jarillo-Herrero, N. Belcari, R. Borcea, G. de Angelis, C. Fahlander, M. Gorska, H. Grawe, M. Hellström, R. Kirchner, M. Rejmund, V. Roca, E. Roeckl, M. Romano, K. Rykaczewski, K. Schmidt, and F. Terrasi, Nucl. Phys. A **669**, 43 (2000).

[10] J. Gomez del Campo, J. L. Charvet, A. D'Onofrio, R. L. Auble, J. R. Beene, M. L. Halbert, and H. J. Kim, Phys. Rev. Lett. **61**, 290 (1988).

[11] J. Gomez del Campo, R. L. Auble, J. R. Beene, M. L. Halbert, H. J. Kim, A. D'Onofrio, and J. L. Charvet, Phys. Rev. C **43**, 2689 (1991).

[12] R. K. Gupta, M. Balasubramaniam, R. Kumar, D. Singh, S. K. Arun and W. Greiner, J. Phys. G: Nucl. Part. Phys. **32**, 345 (2006).

[13] S. S. Malik and R. K. Gupta, Phys. Rev. C **39**, 1992 (1989).

[14] Niyti, R. K. Gupta and W. Greiner, J. Phys. G: Nucl. Part. Phys. **37**, 115103 (2010); R. K. Gupta, Niyti, M. Manhas and W. Greiner, J. Phys. G: Nucl. Part. Phys. **36**, 115105 (2009) .

[15] S. Kanwar, M. K. Sharma, B. B. Singh, R. K. Gupta and W. Greiner, Int. J. Mod. Phys E **18**, 1453 (2009).

[16] B. B. Singh, M. K. Sharma , R. K. Gupta and W. Greiner, Int. J. Mod. Phys E **15**, 699 (2006).

[17] M. K. Sharma, S. Kanwar, G. Sawhney, R. K. Gupta and W. Greiner, J. Phys. G: Nucl. Part. Phys. **38**, 055104 (2011).

[18] M. K. Sharma, G. Sawhney, R. K. Gupta and W. Greiner, J. Phys. G: Nucl. Part. Phys. **38**, 105101, (2011).

[19] K. Sandhu, M. K. Sharma and R. K. Gupta, Phys. Rev. C **85**, 024604 (2012).

[20] M. Kaur and M. K. Sharma, Phys. Rev. C **85**, 054605 (2012).

[21] M. Kaur, M. K. Sharma and Raj K. Gupta, Phys. Rev. C **86**, 064610 (2012).

[22] Raj Kumar, K. Sandhu, M. K. Sharma and R. K. Gupta, Phys. Rev. C **87**, 054610 (2013).

[23] E. Bonnet, J. P. Wieleczko, J. Gomez del Campo, M. La Commara, S. Barlini, C. Beck, B. Borderie, R. Bougault, A. Chbihi, R. Dayras, G. De Angelis, J. D. Frankland, A. Galindo-Uribarri, T. Glodariou, V. Kravchuk, Ph. Lautesse, J. Moisan, N. Le Neindre, B. Martin, L. Nalpas, A. D. Onofrio, M. Parlog, D. Pierroutsakou, F. Rejmund, M. F. Rivet, M. Romoli, E. Rosato, R. Roy, D. Shapira, G. Spadaccini, B. Tamain, and M. M. Vigilante, Int. J. Mod. Phys. E **17**, 2359 (2008).

[24] R. Kumar and R. K. Gupta, Phys. Rev. C **79**, 034602 (2009).

[25] R. J. Charity, D. R. Bowman, Z. H. Liu, R. J. McDonald, M. A. McMahan, G. L. Wozniak, L. G. Moretto, S. Bradley, W. L. Kehoe, A. C. Mignerey, Nucl. Phys. A **476**, 516 (1988).

[26] R. K. Gupta, M. Balasubramaniam, R. Kumar, D. Singh, C. Beck and W. Greiner, Phys. Rev. C **71**, 014601 (2005).

Chapter 7

Dynamics of ^{58}Ni+^{54}Fe$\rightarrow^{112}$Xe* reaction across the Coulomb barrier

The work in previous chapters deal with the energies either near or above the barrier. But here in this chapter, the dynamics of ^{58}Ni+^{54}Fe$\rightarrow^{112}$Xe* massive heavy ion reaction is investigated at energies across the Coulomb barrier. Here the issue of fusion hindrance at sub barrier energies is addressed in terms of barrier lowering property of DCM. The role of deformations and corresponding orientations, diffuseness, structure effects etc. are analyzed in context of the chosen massive heavy ion reaction.

7.1 Introduction

The process of fusion of massive heavy ions is of great interest at low incident energies. It provides opportunity to investigate the dynamics of compound systems formed in heavy ion reactions, besides revealing many interesting aspects related to nuclear structure properties. However there are challenges in the theoretical description of such reactions particularly at sub-barrier energies. The fusion mechanism across the barrier is immensely

influenced by the structure and N/Z ratio of the interacting nuclei [1]. It is worth noting that neutron to proton ratio (N/Z) play an important role in the shape and structure of the nuclei. In low energy heavy ion reactions, the incident beam of projectile should have enough energy to overcome the mutual Coulomb repulsion and lead to the formation of compound nucleus. It is quite an interesting topic to look for the formation and decay aspects of compound nucleus which inturn helps to extract information about the associated nuclear properties and related behavior. The nuclear reactions are the most important probes to extract the information about nuclear dynamics and nuclear structure by observing the decay products and estimating the cross sections in the vicinity of the barrier. Theoretically, many sophisticated approaches have been developed and used to understand the decay modes of various nuclear systems formed in heavy ion reactions. These approaches are based on various hypothesis such as level density, diffuseness, potentials, barrier height, barrier position, deformation, angular momentum etc.

Generally, the analysis of the decaying products impart a comprehensive understanding of the reaction dynamics. The cross sections calculated for the decaying components of compound nucleus exhibit the probable likelihood of occurance of a particular decay mode. In some cases, it has been observed that experimentally measured cross sections at sub barrier energies show sharp decrease and the coupled channel (CC) calculated cross sections are generally overestimated at such energies. This process is termed as fusion hindrance and it is a well established phenomenon in medium mass nuclear systems [2]. The proper explanation of this unexpected steep fall off or hindrance phenomena, is a challenge for the low energy heavy ion community. The hinderance phenomenon is investigated by analyzing the logarithmic derivative and considering the coupling of the relative motion of the colliding nuclei to various states or degrees of freedom in various experimental and theoretical calculations [3–5]. Recently, an experiment [6, 7] was

performed using the massive projectile ^{58}Ni beam from XTU Tandem accelerator of the Laboratori Nazionali di Legnare of INFN, and fusion cross sections were measured over a wide range of energies across the Coulomb barrier down to $\approx 1\mu$b at deep sub barrier energy. This is a pure compound nucleus reaction since quasi fission or non compound nucleus component is not measured for the reaction under study at the given energy range. For the ^{58}Ni+^{54}Fe$\rightarrow^{112}$Xe* reaction, the measured fusion cross section consist of fusion-evaporation process. The CC cross sections are also presented in the work [6, 7] which give good account for higher values of energy however at lower energies, the experimental cross sections fall faster than the CC calculations. Different values of diffuseness parameter were employed to address the data, but the CC calculations were overestimating the cross sections at sub-barrier energies.

In the present work, the decay of ^{112}Xe* formed in ^{58}Ni+^{54}Fe reaction channel is studied using the DCM [8]- [17]. The fusion-evaporation (ER) cross sections are calculated for a range of energies in reference to the experiment [6, 7]. The cross sections are calculated by considering the spherical fragmentation path as well as by including the quadrupole (β_2) deformation with optimum orientation of the decaying fragments. Besides this the effect of adding higher multipole deformations β_2-β_4 with compact orientations has also been worked out at the extreme energies across the barrier. The possible occurance of fusion hinderance at below barrier energies is addressed in terms of barrier lowering index "ΔV_B". ΔV_B arises in a straight forward way via the inclusion of the neck length parameter (ΔR) in DCM based calculations. Here the fusion hindrance aspect is addressed in terms of the barrier modification and have investigated the role of excitation energy, deformations, orientations and angular momentum in the decay of ^{112}Xe* formed in ^{58}Ni+^{54}Fe reaction. The role of diffuseness coefficient is also investigated in context of the reaction under study. The projectile beam ^{58}Ni is a nearly closed shell projectile

which could impart important information in reference to the dynamics of compound nucleus involved. The fragmentation paths are analyzed by striking ^{58}Ni projectile (beam) on different targets ^{54}Fe, ^{58}Ni, ^{64}Ni and ^{74}Ge, where all the reaction channels are having negative Q-value but different N/Z ratio.

The chapter is organized as follows: The calculations and results obtained are discussed in Sec. 7.2 and finally, the results are summarized in Sec. 7.3.

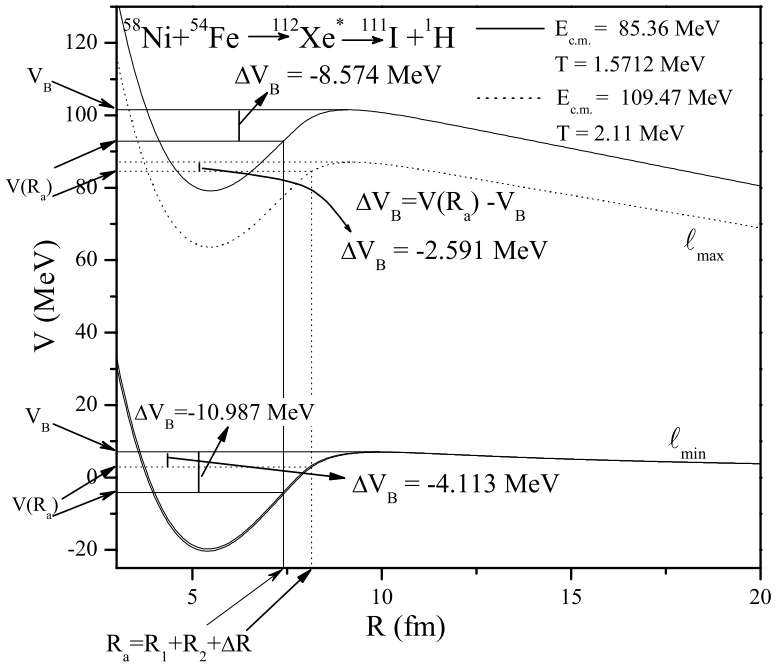

Figure 7.1 shows the scattering potential $V(R, \ell)$ as a function of R for ^{112}Xe* $\rightarrow^{111}$I+^{1}H at temperature T=1.571 MeV and 2.11 MeV (equivalently, $E_{c.m.}$=85.36 MeV and 109.47 MeV) at the two ℓ values of angular momentum. The barrier lowering parameter $\triangle V_B$ is also shown for lowest and highest energy at ℓ_{min} and ℓ_{max} values.

7.2 Calculations

The scattering potential in Fig. 7.1 for ^{112}Xe*$\rightarrow^{111}$I+^{1}H shows the barrier lowering index ΔV$_B$ at extreme energies for the two ℓ values. It is clear from Fig.7.1 that the magnitude of ΔV$_B$ is highest for lower incident energy and/or at lower value of angular momentum.

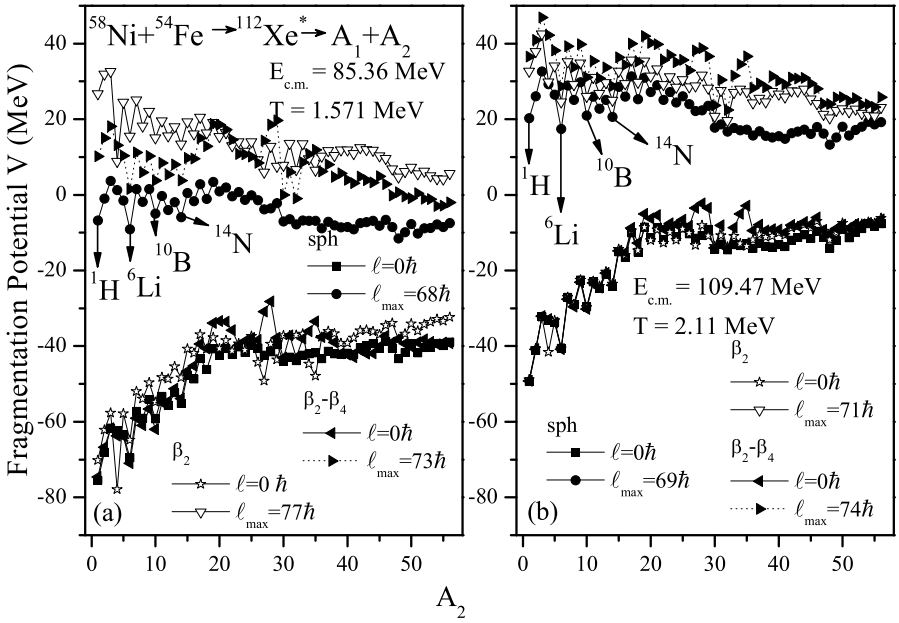

Figure 7.2 (a) and (b) shows the fragmentation potentials $V(R, \ell)$ as a function of A_2 for the decay of $^{112}Xe^{*}$ formed in $^{58}Ni+^{54}Fe$ reaction channel at temperature T=1.571 and 2.11 MeV (equivalently, $E_{c.m.}$=85.36 and 109.47 MeV) respectively, at extreme values of angular momentum ℓ for spherical as well as deformed choices.

This lowering of barrier at sub barrier energies enable us to account for the data at lower incident energies below the barrier.

First of all, the fragmentation behavior is studied for the decay of $^{112}Xe^{*}$ formed in $^{58}Ni+^{54}Fe$ reaction and investigate the comparative contribution of energetically favored fragments along with angular momentum effects. Fig. 7.2 shows the fragmentation potential which is plotted as a function of fragment mass (A_2) at the extreme values of angular momentum at the lowest and highest values of energy lying on the either side of the Coulomb barrier. The fragmentation path is plotted for the spherical as well as deformed choices i.e quadrupole (β_2)-deformed with optimum orientation of decaying fragments and with higher multipole deformation β_2-β_4 with compact orientation approach. The optimum orientations θ_i^{opt} are uniquely fixed on the basis of the quadrupole deformation alone of nuclei [8] and compact orientations θ_i^{c} of hot configurations for higher-multipole

Table 7.1 DCM calculated evaporation residue cross-section (σ_{ER}) considering spherical as well as deformed fragmentation path compared with experiment and DCM predicted σ_{IMF} and σ_{FF} for β_2-deformed fragmentation path.

		ℓ_{max}		ΔR_{ER}		σ_{ER}			at $\Delta R=\Delta R_{ER}$-0.5	
$E_{c.m.}$	T	Sph.	β_2	Sph.	β_2	DCM(Sph.)	DCM(β_2)	Expt.	σ_{IMF}	σ_{FF}
(MeV)	(MeV)	($\hbar$)	($\hbar$)	(fm)	(fm)	(mb)	(mb)	(mb)	(mb)	(mb)
85.36	1.5712	68	77	0.305	0.796	0.0011	0.0011	0.0011±0.00079	1.57×10^{-11}	4.70×10^{-3}
85.84	1.584	68	76	0.360	0.835	0.0023	0.0022	0.0022±0.0010	5.87×10^{-7}	4.78×10^{-3}
86.32	1.593	69	75	0.500	0.926	0.0139	0.0136	0.0139±0.0035	1.00×10^{-4}	2.54×10^{-2}
86.81	1.609	69	75	0.57	0.97	0.0341	0.0348	0.0358±0.0049	1.48×10^{-4}	4.98×10^{-2}
87.29	1.621	69	74	0.70	1.043	0.181	0.1779	0.178±0.019	2.68×10^{-4}	6.74×10^{-2}
88.25	1.6453	69	73	0.815	1.11	0.775	0.78	0.795±0.070	4.76×10^{-4}	1.21×10^{-1}
89.22	1.67	69	72	0.94	1.184	3.54	3.87	3.91±0.12	9.58×10^{-4}	2.42×10^{-1}
90.18	1.693	69	72	1.019	1.2245	8.67	8.61	8.61±0.21	1.48×10^{-3}	2.88×10^{-1}
91.14	1.716	69	72	1.07	1.2575	15.2	15.91	15.93±0.34	2.15×10^{-3}	5.48×10^{-1}
92.11	1.7392	69	72	1.125	1.286	27.1	27.1	27.46±0.61	3.05×10^{-3}	5.2×10^{-1}
93.07	1.7617	69	71	1.178	1.318	46.7	46.1	46.73±0.86	4.92×10^{-3}	5.15×10^{-1}
94.04	1.7842	69	71	1.21	1.34	63.8	64.4	64.48±1.44	6.92×10^{-3}	6.46×10^{-1}
95.00	1.8062	69	71	1.239	1.361	85.1	85.0	85.61±1.91	9.56×10^{-3}	8.26×10^{-1}
95.97	1.8281	69	71	1.237	1.384	116.8	116	116.8±1.8	1.43×10^{-2}	7.94×10^{-1}
96.93	1.8496	69	71	1.288	1.396	132.9	132.3	132.9±3.0	1.76×10^{-2}	8.88×10^{-1}
97.90	1.871	69	71	1.312	1.4135	166	167	167.1±3.7	2.36×10^{-2}	1.078
98.86	1.8921	69	71	1.335	1.433	199.2	198	198.1±4.3	73.33×10^{-2}	1.312
99.82	1.9127	69	71	1.348	1.444	219	219	219.5±3.7	74.07×10^{-2}	1.472
100.79	1.9334	69	71	1.365	1.458	249.1	250.9	250.5±3.5	5.13×10^{-2}	1.744
101.75	1.9536	69	71	1.381	1.468	277	276	276.1±4.7	6.35×10^{-2}	1.464
103.68	1.9938	69	71	1.408	1.485	332	315	332.5±8.7	9.50×10^{-2}	1.956
104.65	2.013	69	71	1.42	1.5	358	357	357.4±8.4	1.11×10^{-1}	2.180
106.57	2.052	69	71	1.437	1.513	390.9	389	390.7±6.2	1.42×10^{-1}	2.440
107.54	2.0716	69	71	1.448	1.523	417	418	418.2±7.1	1.69×10^{-1}	2.760
109.47	2.11	69	71	1.467	1.529	434	435	435.1±5.0	3.06×10^{-1}	1.476

deformations (β_2 - β_4) are taken as prescribed in [18]. It is evident from the Fig. 7.2 that the relative magnitude is comparable at lower ℓ-value for all the choices of fragmentation, which increases with increase in incident energy. Interestingly at ℓ=0, α-nucleus structure is clearly visible for ER and IMF region whereas in heavy mass fragments (HMF) and fissioning region the deformed fragmentation gives enhanced structural effects as compared to that for spherical fragmentation. The deformation effects are distinctly visible at higher angular momentum $\ell=\ell_{max}$. Here again the α-nucleus structure is evident in ER and IMF

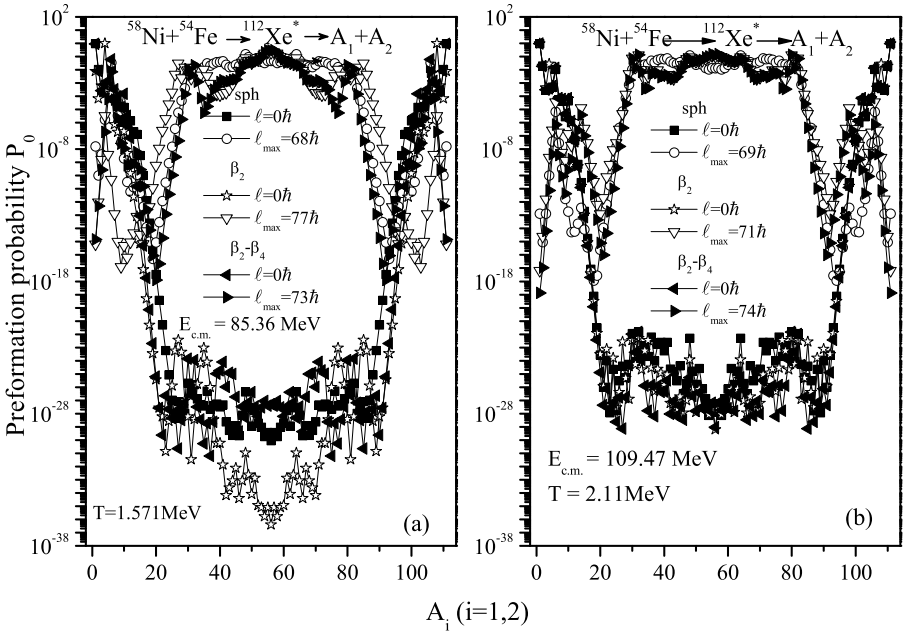

Figure 7.3 (a) and (b) shows the preformation probability P_0 as a function of fragment mass number for the decay of compound system $^{112}Xe^{*}$ formed in $^{58}Ni+^{54}Fe$ reaction channel respectively at $E_{c.m.}$=85.36 and 109.47 MeV (equivalently T=1.571 and 2.11 MeV) for spherical as well as deformed fragmentation paths.

region, whereas the same starts disappearing in HMF and fission region independent of choice of fragmentation. The magnitude of fragmentation potential for spherical choice is lower than that for deformed fragmentation process, possibly due to smaller value of angular momentum for spherical fragmentation process. The energetically favored fragments are depicted in Fig. 7.2 for spherical fragmentation process. One may also notice in Fig. 7.2 that the light particles contribution is prominent at lower ℓ-value for both the energies whereas HMF and fission fragments start competing the light particles at ℓ_{max}-value. This fact can be further exploited from Fig.7.3 which shows the preformation probability as a function of fragment mass at extreme ℓ-values for spherical as well as deformed fragmentation paths.

Fig. 7.3, reemphasizes the fact that light particles are preformed strongly at lower ℓ-value where as fission starts approaching at higher ℓ-values. It is relevant to mention

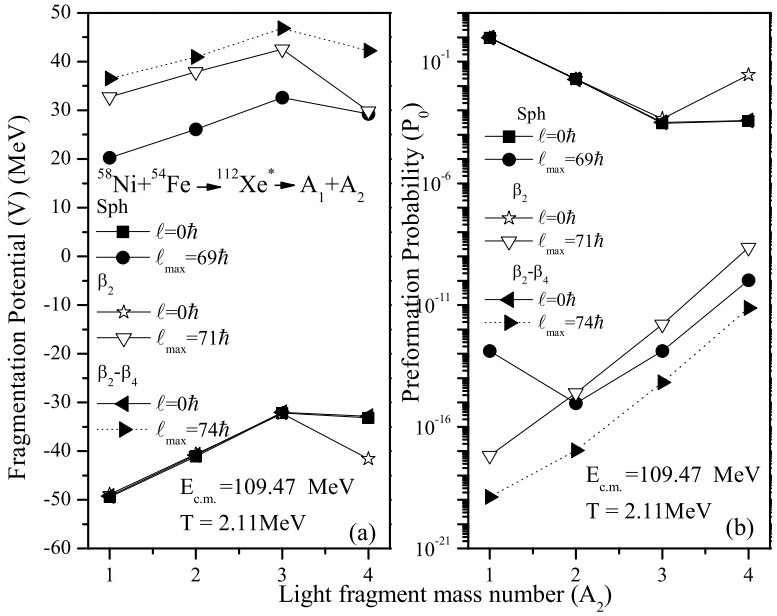

Figure 7.4 Fragmentation Potential and Preformation probability (P_0) as a function of fragment mass number A_2 for A_2=1-4, calculated for the compound system ^{112}Xe* at extreme values of energy, ($E_{c.m.}$) for spherical as well as deformed paths.

here that ℓ_{max} is much higher than ℓ_{crit} (critical angular momentum) due to the use of sticking moment of inertia in the calculation of angular momentum dependent potential, in view of nuclear proximity effect. The main difference between the use of ℓ_{max} or ℓ_{crit} angular momentum is that the neck length parameter ΔR is relatively higher in case of later choice. Fig. 7.3 clearly depict that light particle production does not depend much on the spherical or deformed choice of fragmentation, an extensive analysis of this aspect is worked out in Fig.7.4. However one may observe a noticeable difference in the fission and HMF region. For spherical case, the fission fragments are almost equally preborned in the vicinity of A/2$\pm$24, whereas asymmetric peaks start appearing for the use of deformed fragmentation, along with usual symmetric distribution of fission fragments. Interestingly the appearance of asymmetric peak for deformed fragmentation at A_2=32 and nearby fragments corresponds to proton magic shell closure Z_2=16. On the other hand the complementary peak at A_1=80 and nearby fragments is associated with deformed shell

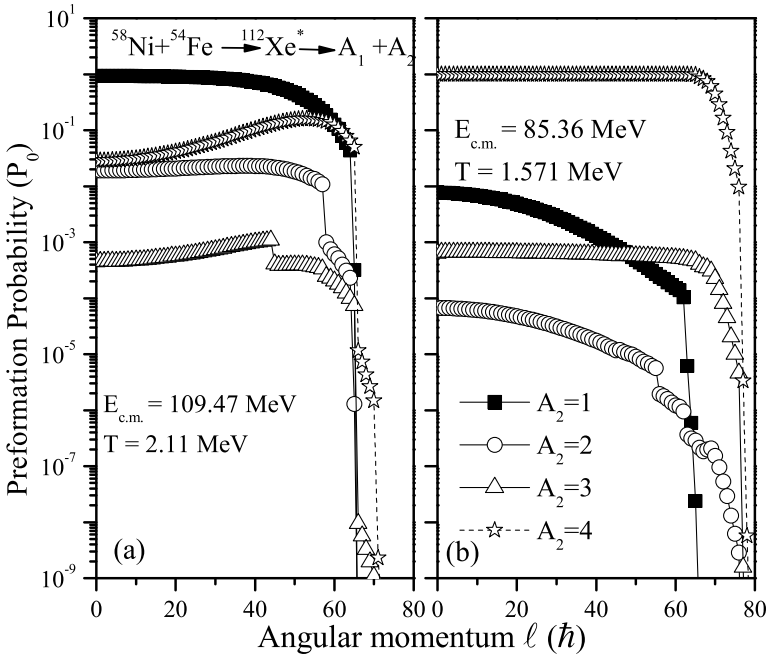

Figure 7.5 Preformation probability and penetrability as a function of angular momentum for the light particle emission A_2=1-4.

closure Z_1=38. Therefore, the inclusion of deformation effects, in a way brings in the shell closure effects of decaying fragments at two extreme energies spread across the Coulomb barrier.

Fig. 7.4 gives the fragmentation as well as preformation probability explicitly for the light particles for spherical as well as deformed choices at highest incident energy. It can be seen from Fig. 7.4(a) that out of LP's, ^{1}H is more favored independent of the deformations at extreme ℓ values, except for the fact that ^{4}Li starts appearing in the β_2 deformed choice at $\ell = \ell_{max}$ value. This emergence of ^{4}Li may not contribute much as light particle production is minimal at higher ℓ-values, as is evident from Fig. 7.4(b). Fig. 7.4(b) clearly shows that preformation probability of light fragments is extremely small at higher ℓ values and ^{1}H is the favored fragment at ℓ=0 case, independent of deformation effects.

Further analysis of ℓ-dependence is worked out in Fig. 7.5(a&b) which shows preformation probability P_0 as a function of angular momentum at highest and lowest incident

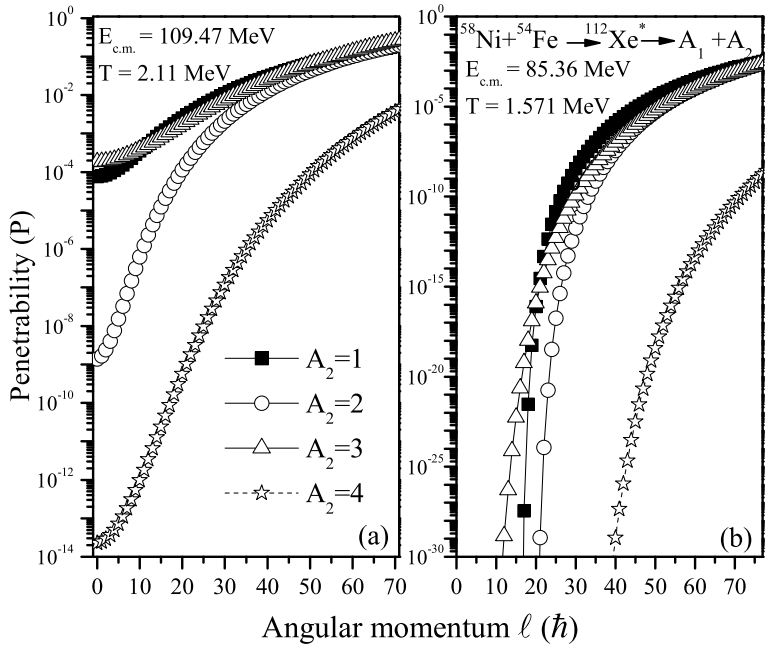

Figure 7.6 The DCM calculated cross-section compared with the experimentally available data as a function of $E_{c.m.}$.

energies respectively. One can see from Fig. 7.5(a) that P_0 is having dominant contribution towards A_2=1 (^{1}H) fragment at all ℓ-values. However the same is not true for lower incident energy where fragment with A_2=4 is more favored over a range of angular momentum value. Therefore one may conclude that relative preformation probability of decaying fragments depends on the incident energy of projectile. Fig. 7.6(a) and (b) show the behavior of penetrability P as a function of angular momentum at two extreme incident energies. Fig. 7.6 shows that in general, the penetrability of ^{1}H fragment leads other fragments in the sequence of A_2=3, 2 and 4 independent of center of mass energy involved. These calculated values of preformation probability and penetrability contribute towards cross section calculations. Table 7.1 shows that the DCM calculated cross sections are in nice agreement with the experiment [6,7] at all reported energies. It can also be seen from Table 7.1 that the ℓ_{max}-value decreases with increase in energy which becomes constant for all the above barrier energies for the β_2 deformed choice however its value remains constant throughout for the spherical choice. The cross sections are calculated by sum-

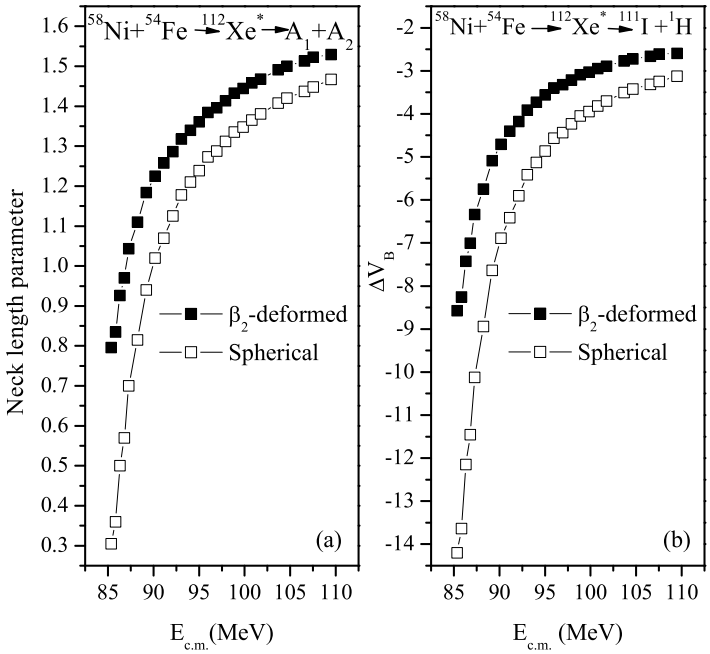

Figure 7.7 (a) and (b) shows the variation of the neck length parameter (ΔR) and barrier lowering ΔV_B as a function of center of mass energy $E_{c.m.}$.

ming the light particle cross sections from ℓ=0 to ℓ_{max}-value by fitting the neck length parameter (ΔR), which decides the first turning point R_a for the fragment to penetrate the barrier. An effort is made to predict the IMF and fission cross sections in reference to ^{58}Ni + ^{54}Fe reaction by considering ΔR_{IMF}= $\Delta R_{fission}$=ΔR_{ER}-0.5 fm for β_2-deformed fragmentation path. It is so, because ΔR for ER is generally more than that for IMF or fission process [12, 15]. The predicted IMF and fission cross sections are shown in Table 7.1, whose magnitude is negligibly small in comparison to the ER cross sections.

Fig. 7.7(a) shows the variation of the neck length parameter (ΔR) with center of mass energy for spherical as well as (β_2) deformed choice of fragmentation. Fig. 7.7(a) clearly depicts that ΔR increases with the center of mass energy and its magnitude is higher for the β_2 deformed choice of fragmentation. The value of ΔR indicates the time scale of the decaying process and it assimilates the neck formation effects.

By fitting the ΔR, the experimental data [6, 7] is fitted nicely at all energies above as well as below the barrier in contrast to the CC calculations where the measured cross

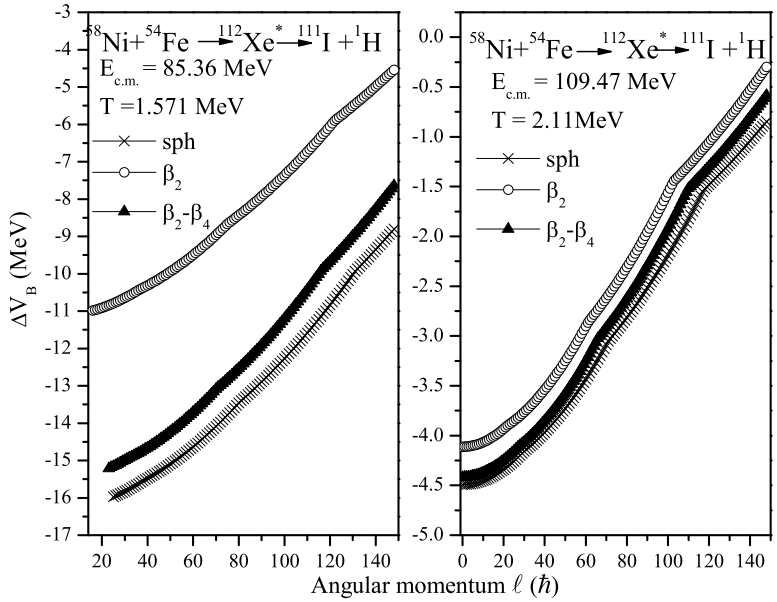

Figure 7.8 The index of barrier lowering, ΔV_B as a function of angular momentum for the decay ^{112}Xe* formed in ^{58}Ni+^{54}Fe reaction channel at extreme values of energy for spherical as well as deformed choice of fragmentation.

sections show deviations at near and below barrier region. The agreement of DCM based calculations with experimental data at below barrier energies is associated with the "Barrier modification" or " barrier lowering" effect which appears in the calculations through neck length "ΔR" fitting. Fig. 7.7(b) shows the DCM calculated index of "barrier lowering" ΔV_B as a function of $E_{c.m.}$ for the reaction ^{58}Ni+^{54}Fe→^{112}Xe*→^{111}I+^{1}H using spherical as well as deformed fragmentation paths. It can be seen from Fig. 7.7(b) that ΔV_B varies exactly the same way as ΔR, justifying the fact that ΔV_B comes in naturally in DCM calculation via the use of neck length parameter. One may observe that ΔV_B is minimum for the highest energy and increases with decrease in center of mass energy. The barrier modification is having the maximum value of ≈8.5 MeV at the lowest energy for the β_2 deformed choice and ≈14 MeV for the spherical case at ℓ_{max} value. The variation of ΔV_B with angular momentum (ℓ) is plotted in Fig. 7.8 for spherical as well as deformed fragmentation paths at lowest and highest energies. One can observe from Fig. 7.8 that ΔV_B increases with decrease in angular momentum (ℓ) independent of the deformation

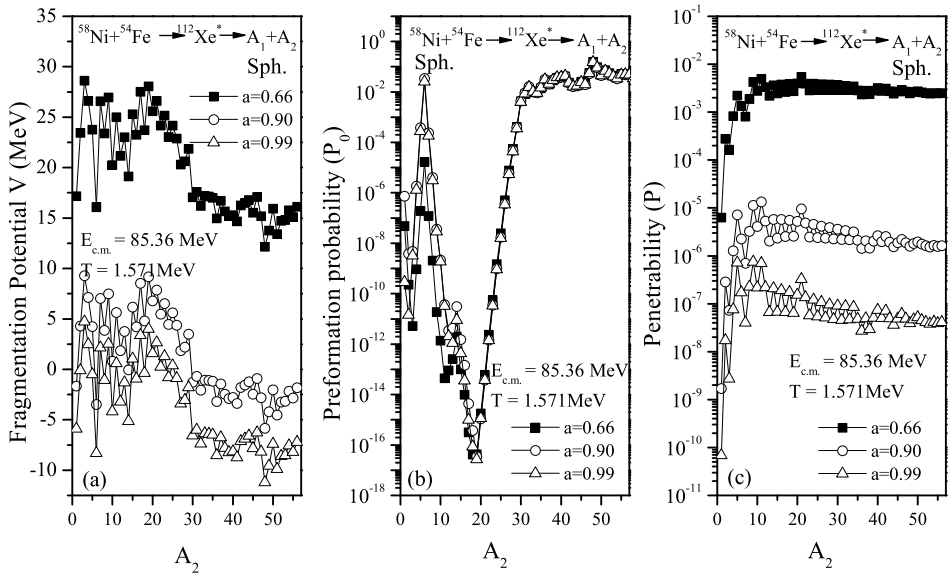

Figure 7.9 (a), (b) and (c) shows the fragmentation potential, preformation probability and penetrability as a function of fragment mass for the decay of ^{112}Xe considering different values for the diffuseness parameter.

effects however it is having highest value for the spherical case followed by hexadecapole (β_2-β_4) and β_2-deformed choices of fragmentation at each ℓ. Fig. 7.8 reconfirms the fact that ΔV_B is larger for below barrier energies and hence helps to address the data at near and sub barrier region.

In the experimental work [6, 7], the measured cross sections are compared with CC calculations for different values of diffuseness coefficient 'a' i.e a=0.66 and a=0.90. In view of this, the role of diffuseness is also investigated in context of DCM calculations. The temperature dependent diffuseness is given as, b=a(1+0.009T^2), where a=0.60, 0.90 and 0.99, the later is more frequently used in DCM calculations (more details are discussed in chapter 2). Fig. 7.9 shows the fragmentation potential, preformation probability and barrier penetrability as a function of fragment mass for the decay of ^{112}Xe* formed in ^{58}Ni+^{54}Fe reaction for the various values of diffuseness coefficient with in spherical choice of fragmentation. It can be seen from Fig. 7.9(a) that the structure remains almost same though the magnitude of the fragmentation potential decreases with the increase in

the diffuseness value. However Preformation probability (depicted in Fig. 7.9(b)) remains almost similar in structure as well as in magnitude. This observation seems to suggest that the probability of formation of the fragments at compound nucleus state does not depend on the choice of diffuseness coefficient. On the other hand the penetrability plotted in Fig. 7.9(c) is having larger magnitude for the lower value of diffuseness parameter without much change in the structure of penetrability. It has been observed that for chosen ΔR value and lower limit of diffuseness say a=0.66, the cross sections come out to be very large however with increase in diffuseness, the cross sections start approaching the experimental values. As the penetrability contributes towards the cross sections, so the larger values of cross section for lower diffuseness can be understood in terms of increased penetrability. It is worth reminding that preformation probability P_0 does not depend much on the choice of diffuseness parameter 'a'. So the change in cross sections is mainly governed via penetrability process. In DCM, usually a=0.99 is used, and the results shown in Table 7.1 correspond to this choice of diffuseness coefficient.

Next in order to investigate the role of orientation degrees of freedom, the barrier height (V_B)and radius (R_B) corresponding to the barrier height is plotted for the decay of ^{112}Xe* formed in ^{58}Ni+^{54}Fe reaction channel as a function of θ_1 at various fixed values of θ_2 in Fig. 7.10, where θs are the orientation angles as shown in [8]. It can be seen from Fig. 7.10(a) that for the symmetric division, the value of R_B is minimum for θ_2=90° and maximum θ_2=180° for all values of θ_1. One may observe in Fig. 7.10(b) that V_B also varies significantly with collision angles, being lowest for θ_2=180° and maximum for θ_2=90° at all values of the θ_1 for the symmetric division. In other words, Fig. 7.10(a) and (b) clearly show that θ_1=90°, θ_2=90° exhibit the most compact hot configuration with minimum radius and maximum barrier height for the symmetric division whereas this is not case for asymmetric division of fragments where θ_2=150° corresponds to the minimum

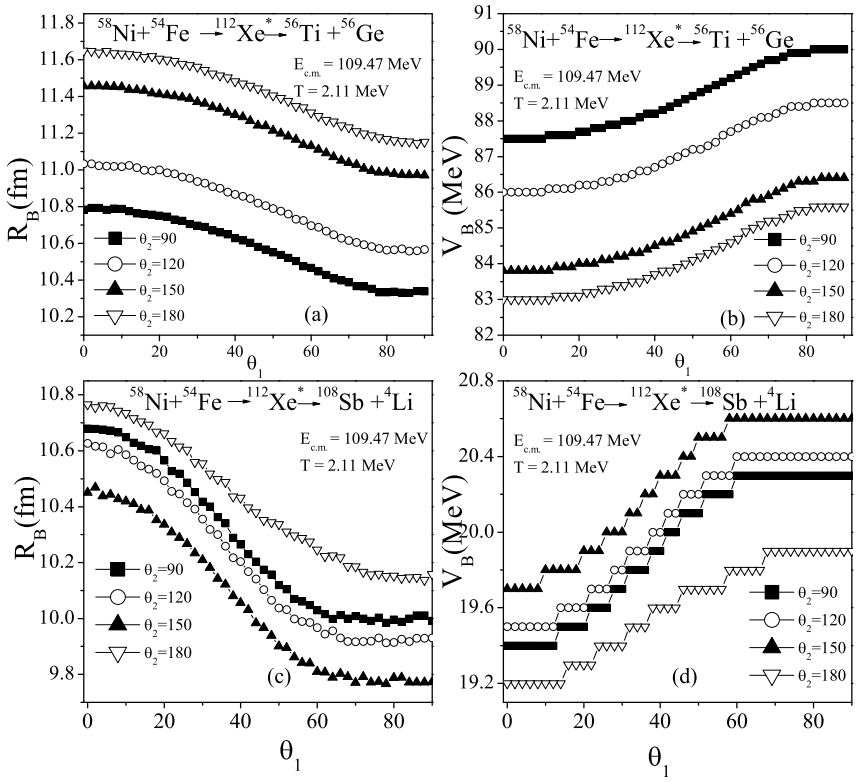

Figure 7.10 The barrier height as well as radius corresponding to the barrier height as a function of orientation angle (θ_1) for the symmetric as well as asymmetric decay.

value of R_B and maximum value of barrier V_B at all θ_1 depicted in Fig. 7.10(c) and (d). It may be noted here that the above observation is valid independent of the energy of projectile. The main conclusion of Fig. 7.10 is that orientation degree of freedom responds differently for symmetric and asymmetric division of compound nuclear system.

Finally, to look for the N/Z dependence, the reactions ^{58}Ni+^{54}Fe$\rightarrow^{112}$Xe*, ^{58}Ni+^{58}Ni$\rightarrow^{116}$Ba*, ^{58}Ni+^{64}Ni$\rightarrow^{122}$Ba* and ^{58}Ni+^{74}Ge$\rightarrow^{132}$Nd* are considered, all having negative Q-value and nearly closed shell projectile beam ^{58}Ni, incident on increasing mass targets. The fragmentation profile of these four reactions is investigated at a comparable energy ($E_{c.m.}\approx$ 99 MeV), to look for the possible structure effects. The cross sections at a comparable center of mass energy are fitted for all the channels by adjusting the neck length parameter. The experimental data at comparable energy is taken from [3] for ^{58}Ni+^{58}Ni and from [19] for ^{58}Ni+^{64}Ni and ^{58}Ni+^{74}Ge reaction channels. Fig. 7.11

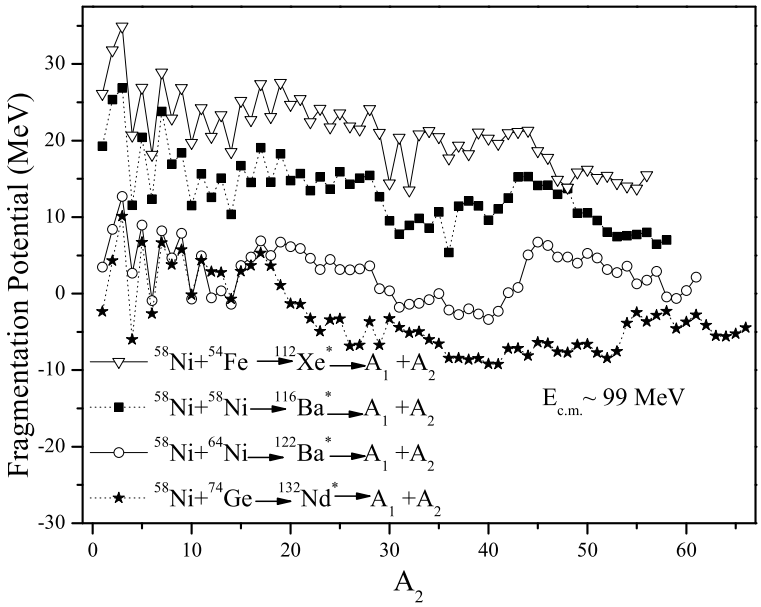

Figure 7.11 Fragmentation Potential as a function of fragment mass for the decay of various nuclear systems formed in ^{58}Ni induced reactions.

shows the fragmentation potential as a function of fragment mass (A_2) for the above mentioned reaction channels at a comparable energy. One may notice that there appears some structure variation with increase in mass of the target nucleus. Fig. 7.11 clearly depicts that α-structure is most prominent for the systems with lower N/Z value i.e ^{112}Xe, ^{116}Ba whereas with increase in N/Z value the α-structure starts vanishing. This observation is consistent with the earlier work [14] discussed in chapter 6, where fragmentation profile of various isotopes of Ba nucleus was analyzed.

7.3 Summary

The decay of ^{112}Xe* formed in ^{58}Ni+^{54}Fe reaction is studied using the dynamical cluster decay model with effects of deformation and orientation degrees of freedom included. The fusion evaporation cross sections calculated at above as well as below barrier energies find nice agreement with the experimental data. The fitted ER cross sections clearly show the signatures of barrier lowering effect at sub barrier energies. The neck length

parameter brings into picture the barrier modification ΔV_B, whose magnitude increases with decrease in energy, independent of deformation effects. This significant barrier modification at low incident energies help to address the data at sub barrier region. The diffuseness parameter does not vary the structure of the fragmentation path however it leads to higher cross section at lower values of diffuseness. It is so because penetrability is greatly enhanced with reduction in diffuseness coefficient. The preformation probability on the other hand plays a silent role with change in diffuseness. Different orientation configurations are suggested for symmetric and asymmetric division of compound nucleus involved. The IMF and fission contribution is predicted to be negligibly small in comparison to ER channel. Interestingly in ER, the relative contribution of light fragments varies with incident energy of projectile.

Bibliography

[1] L. Corradi, *Proceedings of the Conference on New Aspects of Heavy Ion Collisions Near the Coulomb Barrier, Chicago, 2008*, AIP Conf. Proc. **1098**, 334 (2009).

[2] C. L. Jiang, H. Esbensen, K. E. Rehm, B. B. Back, R. V. F. Janssens, J. A. Caggiano, P. Collon, J. Greene, A. M. Heinz, D. J. Henderson, I. Nishinaka, T. O. Pennington, and D. Seweryniak, Phys. Rev. Lett. **89**, 052701 (2002).

[3] M. Beckerman, J. Ball, H. Enge, M. Salomaa, A. Sperduto, S. Gazes, A. DiRienzo, and J. D. Molitoris, Phys. Rev. C **23**, 1581 (1981).

[4] C. L. Jiang et al , Phys. Rev. Lett. **93**, 012701 (2004).

[5] M. Dasgupta, D. J. Hinde, N. Rowley, and A. M. Stefanini, Annu. Rev. Nucl. Part. Sci. **48**, 401 (1998).

[6] A. M. Stefanini, G. Montagnoli, L. Corradi, S. Courtin, E. Fioretto, A. Goasduff, F. Haas, P. Mason, R. Silvestri, Pushpendra P. Singh, F. Scarlassara and S. Szilner, Phys. Rev. C **81**, 037601 (2010).

[7] A. M. Stefanini, G. Montagnoli, L. Corradi, S. Courtin, E. Fioretto, A. Goasduff, F. Haas, P. Mason, R. Silvestri, Pushpendra P. Singh, F. Scarlassara and S. Szilner, Phys. Rev. C **82**, 014614 (2010).

[8] R. K. Gupta, M. Balasubramaniam, R. Kumar, N. Singh, M. Manhas and W. Greiner, J. Phys.G : Nucl. Part. Phys. **31**, 631 (2005).

[9] B. B. Singh, M. K. Sharma and R. K. Gupta, Phys. Rev. C **77**, 054613 (2008). B. B. Singh, M. K. Sharma , R. K. Gupta and W. Greiner, Int. J. Mod. Phys E **15**, 699 (2006).

[10] Niyti, R. K. Gupta and W. Greiner, J. Phys. G: Nucl. Part. Phys. **37**, 115103 (2010); R. K. Gupta, Niyti, M. Manhas and W. Greiner, J. Phys. G: Nucl. Part. Phys. **36**, 115105 (2009) .

[11] S. Kanwar, M. K. Sharma, B. B. Singh, R. K. Gupta and W. Greiner, Int. J. Mod. Phys E **18**, 1453 (2009).

[12] M. K. Sharma, S. Kanwar, G. Sawhney, R. K. Gupta and W. Greiner, J. Phys. G: Nucl. Part. Phys. **38**, 055104 (2011).

[13] M. K. Sharma, G. Sawhney, R. K. Gupta and W. Greiner, J. Phys. G: Nucl. Part. Phys. **38**, 105101, (2011).

[14] M. Kaur, R. Kumar and M. K. Sharma, Phys. Rev. C **85**, 014609 (2012). M. Kaur, M. K. Sharma and R. K. Gupta, Phys. Rev. C **86**, 064610 (2012).

[15] M. Kaur and M. K. Sharma, Phys. Rev. C **85**, 054605 (2012).

[16] K. Sandhu, M. K. Sharma and R. K. Gupta, Phys. Rev. C **85**, 024604 (2012). K. Sandhu, M. K. Sharma and R. K. Gupta, Phys. Rev. C **86**, 064611 (2012).

[17] G. Sawhney and M. K. Sharma, Eur. Phys. J. A **48**, 57 (2012). G. Kaur and M. K. Sharma, Nucl. Phys. A **884**, 36 (2012). G. Kaur and M. K. Sharma, Phys. Rev. C **87**, 044601 (2013).

[18] R. K. Gupta, M. Manhas, W.Greiner, Phys. Rev. C **73**, 054307 (2006).

[19] M. Beckerman, M. Salomaa, A. Sperduto, J. D. Molitoris and A. DiRienzo, Phys. Rev. C **25**, 837 (1982).

Chapter 8

Summary and outlook

In this thesis, the dynamical cluster decay model (DCM) has been applied to study the decay of hot and rotating nuclear systems formed in heavy ion reactions over a wide mass range from A=100-255. Based on the quantum mechanical fragmentation theory, DCM has been formulated to study the decay of excited (hot) compound systems formed in heavy ion reactions. It treats the emission of light particles LP/ER, IMF and FF on equal footings using the collective clusterization method.

An overview of present status of research and general introduction related to this work have been discussed in Chapter 1. The details of the methodology used i.e the dynamical cluster decay model is discussed in Chapter 2. The model has been employed to address various nuclear phenomena associated with decay paths of compound nuclear systems formed in heavy ion reactions at low energy region.

As a first application, DCM is applied to study the decay of ^{254}Fm* compound system over a wide energy range in Chapter 3. The actinide nuclear system ^{254}Fm* is formed in boron (^{11}B) induced, ^{11}B+^{243}Am reaction. The entrance channel mass asymmetry α when compared with α_{BG}, suggests no non compound nucleus (nCN) contribution however anomalous values of fission fragment anisotropies anticipate nCN contribution which was

related to target deformation. In order to investigate this aspect, the decay of ^{254}Fm* is studied using DCM by considering spherical as well as by including higher multipole deformations with corresponding orientations. The nice comparison of DCM calculations with the experimental data at all energies suggests that the contribution of competing non-compound nucleus quasi-fission (qf) component is quite small. With the static as well as dynamic deformation, the structure remains almost similar with no significant change. The mass distribution changes from symmetric in heavy ion induced decay to asymmetric in spontaneous decay of ^{254}Fm. Independent of the number of neutrons, the mass distribution remains symmetric for various isotopes of fermium. The fission fragment anisotropies calculated using DCM based parameters at $\Delta R_{fission}$ are in agreement with the statistical model calculations, but for ΔR increased to bring it close to I_{NS} value, the anisotropies start approaching the experimental data. The neck-length parameter ΔR is relatively larger for β_2-deformed case, and comparable for spherical and β_2-β_4 deformations. The fragmentation behavior is influenced by the inclusion of deformations and orientations but remains symmetric in the fissioning region.

In addition to compound nucleus decay, DCM has been applied to study the incomplete fusion (ICF) systematics in reference to carbon induced reaction channels in Chapter 4. The cross sections calculated within DCM for the decay of ^{220}Ra* compound nucleus formed in ^{12}C+^{208}Pb and ^{13}C+^{207}Pb reaction channels find nice comparison with the experimental data. Different decay paths of ^{220}Ra* involving n-decay, ER, fission, charged particle decay (αxn) and competing ICF process are investigated where the fitted neck length parameter is higher for ER and n-decay. It implies that ER or n-decay occur almost simultaneously at an early stage, followed by ICF, αxn and fission decay in sequence. The entrance channel independence is observed by analyzing the fragmentation path, preformation profile, angular momentum, barrier characteristics and neck length parameter.

Besides this, the fragmentation behavior of different nuclear systems formed by striking ^{13}C projectile on increasing mass targets is explored using CF and ICF process, which shows that the mass distribution changes from near symmetric to asymmetric when the target changes from medium mass to heavy mass region. The ICF% systematics is worked out as a function compound nucleus mass and target mass and is found to be larger for asymmetric channel which is in line with the Morgestern systematics.

In Chapter 5, the decay of preactinide nuclear system ^{204}Po* formed via ^{16}O + ^{188}Os and ^{28}Si +^{176}Yb reaction channel is investigated in the framework of DCM. It is important to note that here the cross sections are calculated by simultaneously fitting the neck length parameter for the ER and fission process. With the spherical choice of fragmentation the ER data couldn't fit therefore the β_2-deformation effects are included in calculations. With the deformed choice of fragmentation the calculated evaporation residue cross-sections and fission cross-sections find excellent agreement with the available data at all incident center of mass energies, except at one highest energy for the channel ^{28}Si +^{176}Yb in case of fission process. This indicates the presence of some amount of nCN contribution at this energy which is also expected as the entrance channel mass asymmetry for ^{28}Si +^{176}Yb channel is less than α_{BG} and also the Z_pZ_t product of this channel is near 1000 which is considered for the onset of nCN. The fission fragment anisotropies calculated within SSPM approach using DCM based ℓ_{max} values for the non sticking moment of inertia, show reasonable comparison with the experimental data, so the contribution of nCN component is not confirmed in agreement with the experimental predictions. The modification in the preformation probability with addition of two neutrons (i.e for the decay of Po isotopes) imparts important information regarding sub structure of fission fragments in decay of Po isotopes. In addition to ℓ-independence, the decay barrier heights show entrance channel independence for the heavy nuclear system ^{204}Po* formed

in ^{16}O and ^{28}Si induced reactions.

Besides the ER and fission cross sections, independent fragment cross sections are also worked out in Chapter 6. Here the decay of ^{118,122}Ba* formed in ^{78,82}Kr+^{40}Ca reactions is studied at a relatively low laboratory energy of 5.5 MeV/nucleon using DCM for the available data. Within DCM, the data is accounted reasonably well for the ER as well as total fission cross-sections (by incorporating the qf component) with the spherical choice of fragmentation. In addition to total cross sections, independent fragment cross sections are also worked out within DCM. The DCM based calculations under-estimate the yields in a narrow window of $6 \leq Z \leq 18$. The overall comparison of the DCM based calculations with experimental data is better than for both the BUSCO and GEMINI codes, and could perhaps be improved with the inclusion of the secondary emission of light particles from the primary fragments. For the unfitted region, different values of level density parameter and pairing strength are employed where even Z fragments become relatively favorable with the inclusion of pairing strength. The level density parameter, non zero pairing strength as well as different versions of proximity potentials are not able to account for the unfitted valley. Therefore the non-compound nucleus contribution (nCN) is predicted for the unfitted region ($6 \leq Z \leq 18$) which bring the DCM results closer to experimental data. The α-nucleus structure starts vanishing with increase in N/Z ratio. The neutron deficient Ba nuclei are shown to give enhanced ER and fission cross-sections.

In the above discussion, DCM has been applied to study a variety of nuclear systems over a range of energies near and above the Coulomb barrier. In Chapter 7, the decay of medium mass nuclear system ^{112}Xe* is investigated across the Coulomb barrier down to deep sub barrier energies. The fusion evaporation cross sections calculated at above as well as below barrier energies find nice agreement with the experimental data because of the barrier lowering property of DCM at sub barrier energies. The neck length parameter

allows us to define the barrier modification ΔV_B, whose magnitude increases with decrease in energy, independent of deformation effects. The predicted IMF and fission contribution is negligibly small compared to ER cross sections. Within ER, the relative contribution of light particles is shown to change with energy of projectile. Beside this, the role of diffuseness parameter is investigated and the cross sections are observed to have larger value for lower diffuseness coefficient, which is associated with enhancement in magnitude of penetration probability. Interestingly, the preformation factor does not depend on the choice of diffuseness parameter. In addition to this, the behavior of orientation degree of freedom is investigated and different orientational configurations are suggested for light and heavy fragments emerging from compound nuclear state. More α-structure is evident for the compound system with lower neutron to proton ratio.

The work of this thesis has the potential of getting extended to other mass regions such as light mass region A<100 and super heavy mass region for better understanding of the reaction dynamics. The present work involves deformation effects upto hexadecapole within coplanar approach (ϕ =0) and hence it would be of further interest to include non coplanar ($\phi \neq 0$) orientations in the decay of hot and rotating nuclei produced in heavy ion reactions. Beside this, the methodology used may be refined further to address competing non compound nuclear processes.